DESIGN AND OPTIMIZATION OF MICROSTRUCTURED OPTICAL FIBER SENSORS

by

Charles Milford Jewart

BSEE, University of Pittsburgh, 2004

MSEE, University of Pittsburgh, 2006

Submitted to the Graduate Faculty of

Swanson School of Engineering in partial fulfillment

of the requirements for the degree of

Doctor of Philosophy in Electrical Engineering

University of Pittsburgh

2011

UNIVERSITY OF PITTSBURGH

SWANSON SCHOOL OF ENGINEERING

This dissertation was presented

by

Charles M. Jewart

It was defended on

June 10, 2011

and approved by

Joel Falk, PhD, Professor, Electrical and Computer Engineering

Minhee Yun, PhD, Associate Professor, Electrical and Computer Engineering

William Stanchina, PhD, Professor, Electrical and Computer Engineering

Qing-Ming Wang, PhD, Associate Professor, Mechanical Engineering and Materials Science

Ilya Avdeev, PhD, Assistant Professor, Department of Mechanical Engineering,

University of Wisconsin-Milwaukee

Dissertation Director: Kevin P. Chen, Associate Professor, Electrical and Computer Engineering

DESIGN AND OPTIMIZATION OF MICROSTRUCTURED OPTICAL FIBER SENSORS

Charles M. Jewart, PhD

University of Pittsburgh, 2011

The integration of sensor networks into large civil and mechanical structures is becoming an important engineering practice to ensure the structural health of important infrastructure and power generation facilities. The temperature, pressure, and internal stress distribution within the structures are key parameters to monitor the structural health of a system. Optical fiber sensors are one of the most common sensing elements used in the structural health monitoring due to their compact size, low cost, electrical immunity, and multiplexing ability.

In this dissertation, the design and optimization of air-hole microstructured optical fibers for use as application specific sensors is presented. Air hole matrices are used to design fiber cores with a large birefringence; while air hole arrays within the fiber cladding are studied and optimized to engineer unique geometries that can give desired sensitivity and directionality of the fiber sensors.

A pure silica core microstructured photonic crystal fiber was designed for hydrostatic pressure sensing. The impact of the surrounding air-holes to the propagation mode profiles and indices were studied and improved. To improve directionality and sensitivity of fiber sensors, air holes in the fiber cladding were implemented and optimized in the design of the fiber. Finite element analysis simulations were performed to elicit the correlation between air-hole

configuration and the fiber sensor's performance and impact of the fiber's opto-mechanic properties.

To measure pressure and stress at high temperature, an ultrafast laser was used to inscribe type II gratings in two-hole microstructured optical fibers and suspended core fibers. The fiber Bragg grating resonance wavelength shift and peak splitting were studied as a function of external pressure, bending, and lateral compression. Fiber sensors in two-hole fibers show stable and reproducible operation above 800^{o}C. Fiber grating sensor in suspended core fibers exhibits high directionality to transverse stress, and insensitivity to bending. All experimental results are in good agreement with the simulations.

This works demonstrates that ingenious design and engineering of air hole matrices in optical fiber's cladding and core can lead to multi-functional and multiplexable fiber sensors that were previously unattainable using traditional solid-core solid cladding fiber.

TABLE OF CONTENTS

LIST OF TABLES

LIST OF FIGURES

PREFACE

For Linda and AmyAnne

1.0 MICROSTRUCTURED OPTICAL FIBER SENSORS

Fiber optical sensors and devices have been of great interest over the past 40 years due to the small size, low loss and electromagnetic immunity. Much work has already been demonstrated on the applications of Fabry-Perot cavity fiber sensors, fibers that employ the use of interferometer methods such as the SAGNAC method, multi-core fibers, and fiber Bragg gratings. However, all of these methods have been primarily concerned with the use of single-mode optical fibers (SMF-28) and the development of new interrogation systems and are inherently limited by the material properties of the material and cylindrical nature of the fiber. To overcome these limitations significant work has been performed over the last 10 years in the area of microstructured optical fibers (MOFs).

Microstructured optical fibers are optical fibers that have had air holes introduced to the fiber cladding region. These air holes allow for the breaking of the symmetry of the fiber and the creation of optical fibers with unique optical traits and the ability to engineer application specific fibers for telecommunications and sensing applications. Microstructured optical fibers call into two types of operation, those that posses a doped core where confinement and propagation occurs in the same manner as traditional fibers and those that operate by a photonic bandgap, where the air holes are formed into a matrix and thus create photonic crystal fibers (PCFs).

This chapter will review the first microstructured fibers originally created at Bell Labs in the 1970s. The two hole fiber will be discussed with a few examples of sensing applications.

Photonic crystal fibers will be covered including their initial creation and their eventual use in the development of optical sensors. Highly birefringent photonic crystal fibers will be reviewed, including their design and applications to pressure sensing. Finally, suspended core optical fibers will be discussed, including different fabrication methods and current application avenues being investigated.

1.1 MICROSTRUCUTRED OPTICAL FIBERS

The first microstructured optical fiber was developed at Bell Labs by Kaiser and Astle [1] in 1974. The developed fibers were low-loss all-silica fibers that operated in single or multi-mode. The first ever developed microstructured optical fibers are presented in Figure 1. The single and multi-mode fibers possessed a thin strut (slab) support with a larger core region in the center. The demonstrated strut supports and core dimensions (h x w) are 4 μm and 6 μm x 5 μm for the single- mode fiber. The multi-mode fiber was demonstrated with cores 1-5 μm thick and cores 20-30 μm in diameter. For testing of the fiber properties, a HeNe laser (632.8 nm) was used and upon excitation it was apparent that other propagating modes were present in the fibers. Slab modes were confined within the slab and could extend further into the cladding region for small lengths of fiber (<2 cm). Additionally, the large air region contained propagating modes in the same manner as a hollow-dielectric waveguide and cladding modes. The presence of these additional propagating modes required a length of 1 meter for complete attenuation of the slab and hollow waveguide modes from the fiber. Index matching liquid is necessary to remove the cladding modes. Overall, the single-mode design experienced losses of 50 dB/km at

wavelengths from 0.5 to 1.15 μm. The multi-mode fiber possessed losses between 7.5 and 10 dB/km. The thin walled single-mode fiber and multi-core fiber were fabricated via the stacking of thin capillary tubes. The single-mode and multi-mode fibers required use of two thin-walled tubes and three thin-walled tubes, respectively.

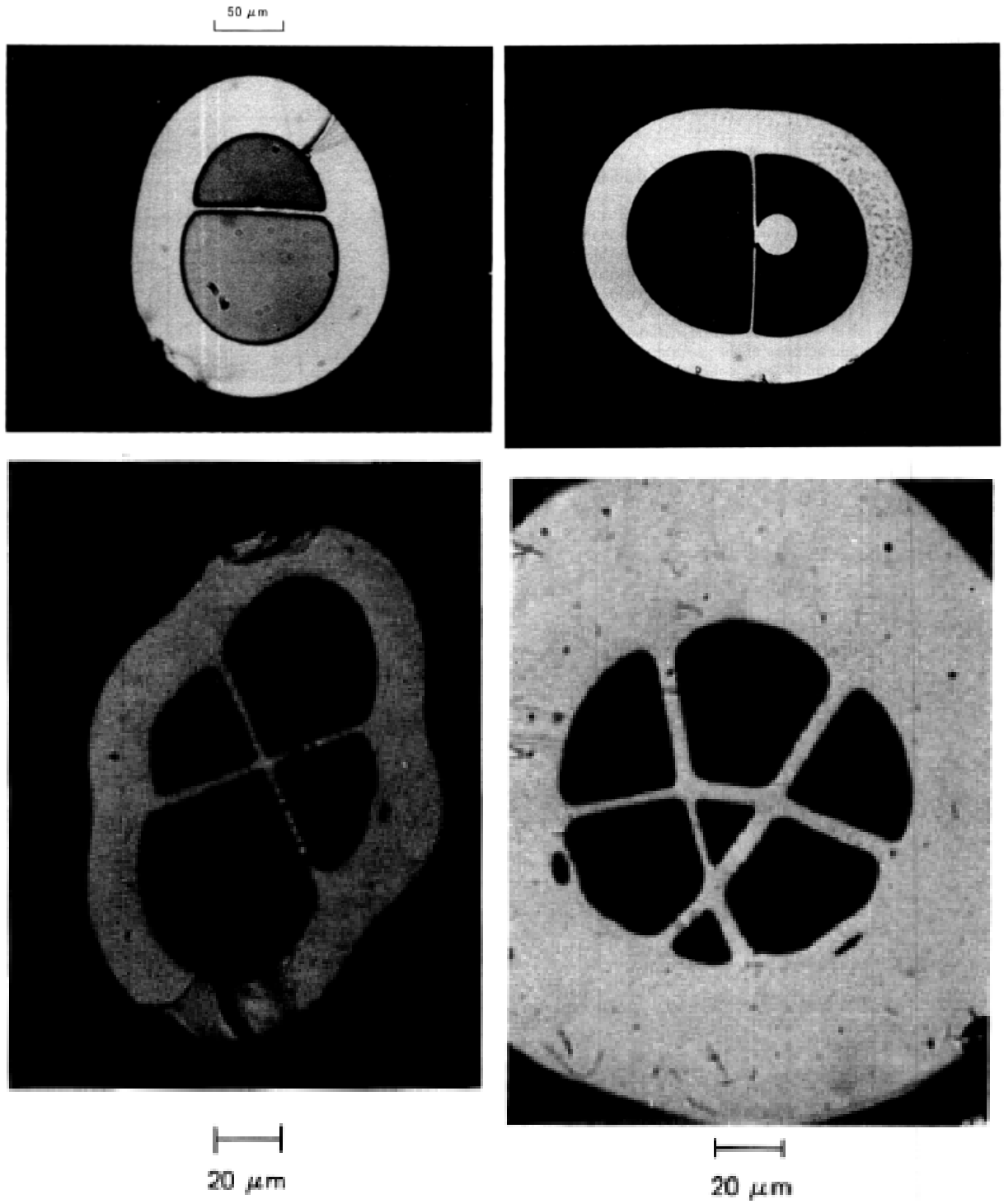

Figure 1: Cross-sectional pictures of first demonstrated microstructured optical fibers: single-mode fiber (top left), multi-mode (top right), single-mode with thin walls (bottom left) and multi-core fiber (bottom right) [1]

The next microstructured optical fiber to be demonstrated was the two hole fiber design first proposed by Xie *et al.* [2] in 1986. The concept behind this design was to allow for the creation of a fiber optic pressure sensor with the added benefit of having a built-in transducing mechanism. The fiber geometry was modeled after the PANDA fiber but with two open channels along the length of the fiber in place of the stress-inducing region with a Ge-doped core places within the geometric center. This fiber has two modes of operation, the first being that if a pressurized gas or liquid is present within the air holes, the second mode of operation is for the air holes to be held at room pressure while a pressure is applied to the fiber's outer wall. Both of these methods of operation will cause an pressure induced birefringence in the fiber. To test the fiber's versatility, a Mach-Zehnder interferometer was created. The overall increase in sensitivity to pressure for the two hole fiber over traditional fiber pressure sensors at the time was ~2.6.

In 1998, Clowes *et al*. performed the first studies on the placement and size of air holes within the fiber cladding and their effects on the ability of the fiber to be used as a fiber sensor [3]. The fibers possessed center regions and hole radii of 9.5 μm 24.46 μm, 16.49 μm and 30 μm for cross section A and B, respectively. The two fiber cross-sections under study are presented in Figure 3. From their results, they were able to demonstrate that there is a linear dependency in the induced birefringence with the angle between the fiber core and the upper edge of the air hole. Good agreement with the simulation results and experimental results were obtained for angles lower than 45^{o} between the fiber core and top of the air hole. The breakdown of the simulation was deemed not a major factor as fabrication of fibers with angles greater than 45^{o} would be extremely fragile and difficult to manufacture. This was the first time that

engineering of the air holes within an optical fiber was demonstrated to have a significant effect on the sensing properties of the fiber.

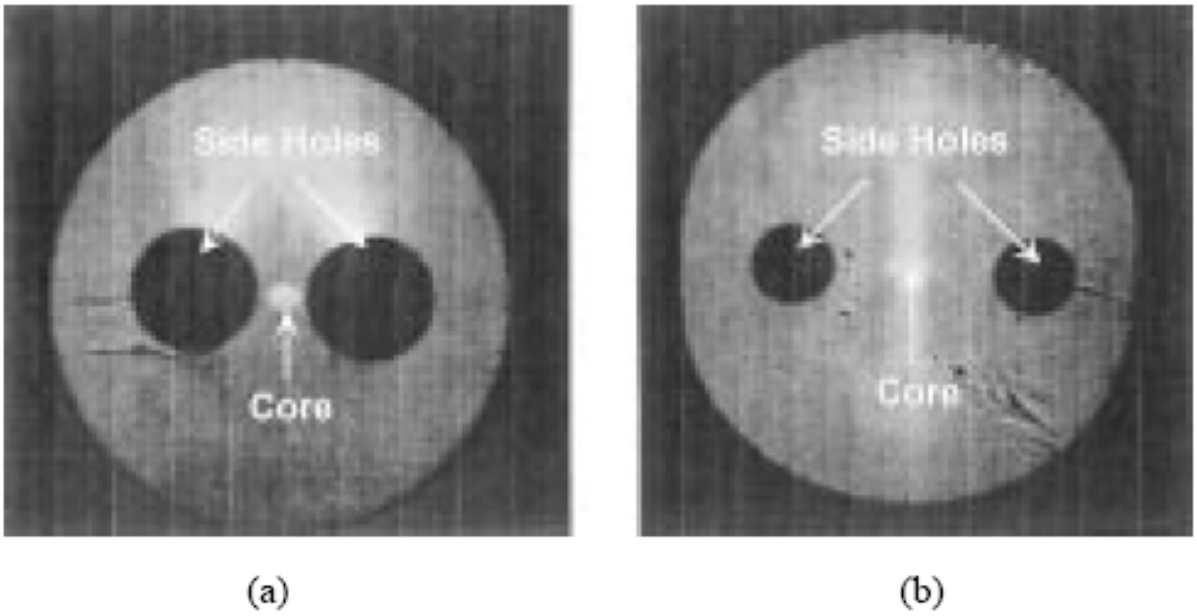

Figure 2: Side-hole fiber cross sections [3] (© [1998] IEEE)

The further development of microstructured fibers was the eventual creation of a photonic crystal fiber in 1996 by Knight *et al*. [4]. This fiber possessed a fiber structure that had a hexagonal hole pattern with a single solid, silica section in the geometric center. This solid section behaved as an optical core, while the air holes induced a photonic bandgap, effectively trapping the propagating light in the core region. The fabrication method for the creation of the fiber consisted of the creation of silica capillaries that were stacked to create the desired fiber structure. A SEM image of the photonic crystal fiber is given in Figure 4. The fiber structure suffered no variation over the length of several meters, allowing to a good, consistent fiber from the fabrication method. The fiber was coupled with four wavelengths of light (457.9 nm, 632.8 nm, 850 nm and 1550 nm) and was demonstrated to be single-mode, with the propagating modes

having better confinement at the higher wavelengths. Interestingly, the fiber was demonstrated to have two distinct polarization axes despite the hexagonal symmetry.

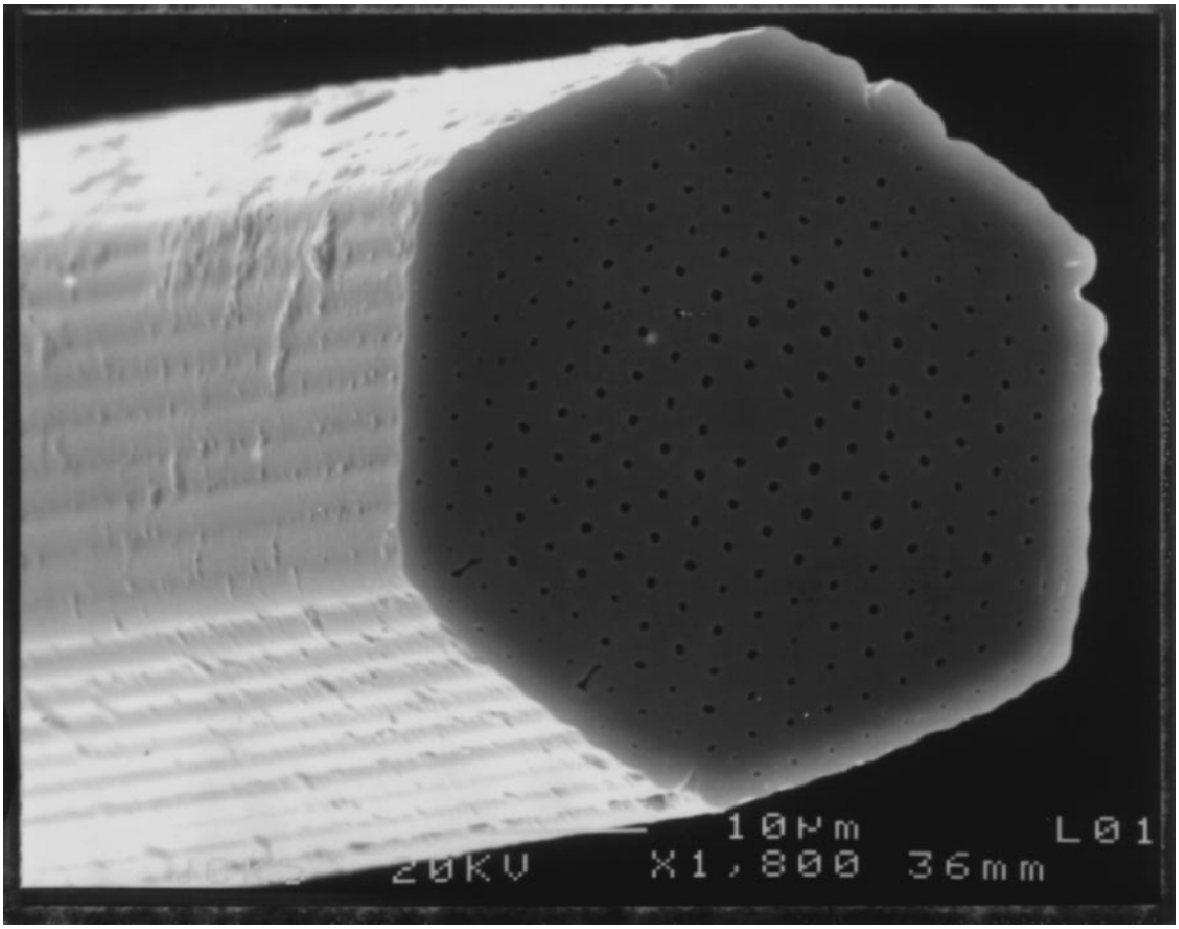

Figure 3: SEM image of photonic crystal fiber [4]

In 2005 the first major study was performed on PCFs to determine their sensitivity to applied external fields such as temperature, strain and pressure [5]. Bock *et al*. performed studies on a single-mode PCF with a hexagonal lattice structure and solid core. To determine the parameters of the fiber under test a Michelson interferometer with a broadband source were used. Results of the study were determined based upon the change in the optical path due to external

loads acting on the fiber. The overall fiber sensitivities (change in effective index) to temperature (10-100^{o}C), strain (0-1.5 mstrain) and pressure (0-18 MPa) were determined to be [1.28±0.05]x10^{-5} K^{-1}, -0.40±0.01 ε^{-1} and [-1.03±0.02]x10^{-5} MPa^{-1}, respectively. These results showed that the PCF had sensitivities close to that of standard optical fiber (SMF-28), with the discrepancy occurring in the pressure sensitivity having a negative change in the index of refraction.

Another significant breakthrough in the development of PCF sensors was demonstrated in 2005 when Martelli *et al*. demonstrated the ability of fiber Bragg gratings (FBGs) to be inscribed into PCFs [6]. This fiber was created from silica with an Er^{3+} doped core, though the erbium only affected the refractive index of the core region. Due to the nature of the PCF, a two-photon process was required to inscribe the FBG. As this particular fiber possessed two modes, one in the core and one in the cladding two distinct grating peaks were inscribed in the fiber. The temperature results of the FBGs in the PCF have sensitivities of 19.72 pm/K and 20.14 pm/K for peaks (1) and (2), respectively. These results are consistent with standard silica fibers with the erbium doping causing a slight difference. The FBGs were then tested with an applied longitudinal strain. The fundamental mode experienced a sensitivity of 1.2 pm/με with a linear trend. However, the higher order mode experiences a quadratic response to the strain. The cause of the quadratic response is that the higher order mode is confined within the PCF matrix region, which is highly sensitive to the changes in air hole diameter and spacing.

1.2 HIGHLY BIREFRINGENT PHOTONIC CRYSTAL FIBERS

Significant work was been performed on photonic crystal fibers (PCF), including theoretical calculations [7], fabrication [5] and applications [6]. By proper design of the air matrix it is possible to greatly tailor the optical properties of the PCF. One of the more recent trends has been the creation of highly birefringent fibers for use as optical sensors. By creating an asymmetric core within the fiber it is possible to create a fiber that possesses a large birefringence ($\sim 10^{-3}$) that can perform as a polarization-maintaining (PM) fiber and allow for better signal-to-noise ration and simplified measurements for sensing applications.

The first highly birefringent PCF calculations were demonstrated in 2001 by Libori *et al*. [8]. In order to create a highly birefringent fiber the standard hexagonal lattice was altered so that two larger holes were added. This method breaks the 60 degree symmetry in the PCF and in turn creates symmetry of 180 degrees. Figure 4 presents the initial design for this fiber as well as a commercially available fiber from Blaze Photonics [9]. This fiber design has been reported on extensively [10-14] in its ability to act as a hydrostatic pressure sensor. Additionally, this fiber presents significant benefits in that it possesses a temperature coefficient of birefringence ~30 times less than standard HiBi (PANDA) fibers, making this fiber inherently temperature insensitive.

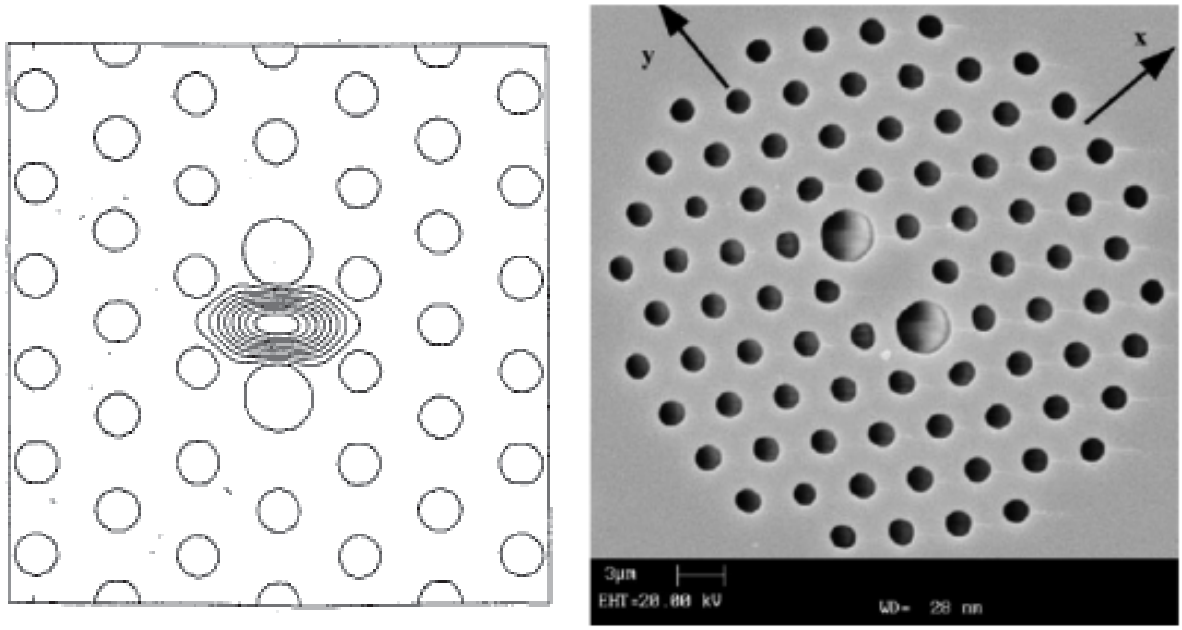

Figure 4: Highly birefringent design (left) [8] (© [2001] IEEE) and commercially available fiber [9]

Szpulak *et al*. [15] compared the effects hydrostatic pressure has upon the phase and group birefringence in PCFs. Their approach was to compare the fiber from Blaze Photonics with a new custom designed fiber structure. The design of the structure was a modified hexagonal lattice, with a center region of holes smaller than the surrounding holes. The two designs were similar to those studied by Bock *et al.* [16] and are presented in Figure 5. This design approach allowed for a fiber with an intrinsic birefringence of ~$1x10^{-3}$ and $0.4x10^{-3}$ for the structure A and B fiber designs, respectively. However, when the fibers were placed under and applied hydrostatic pressure, the fiber produced by Blaze Photonics experienced a pressure sensitivity 60% greater than that of the structure A fiber.

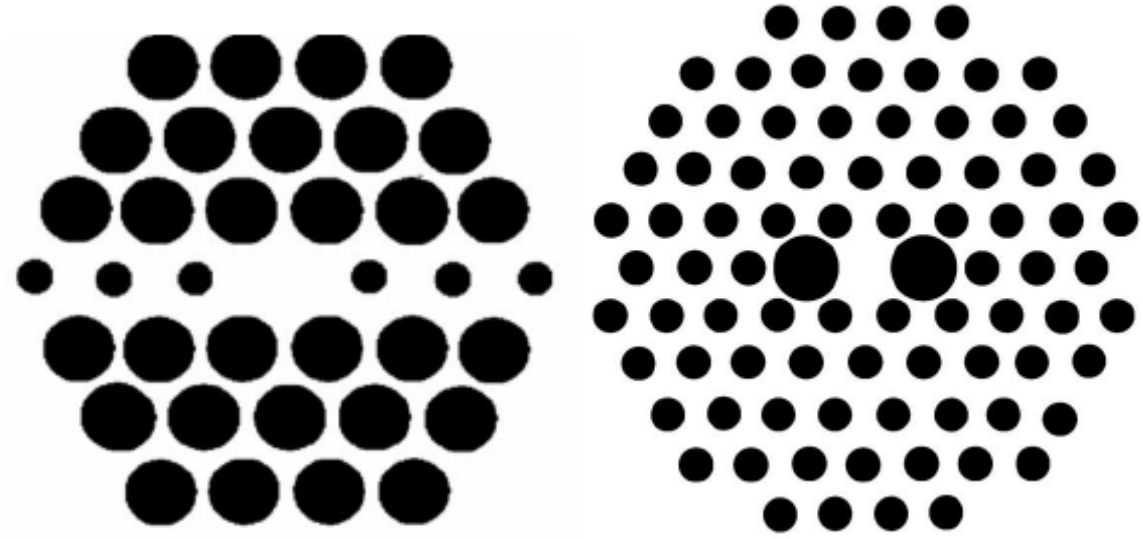

Figure 5: Cross section of new fabricated PCF (left) and cross section of commercially available fiber [16] (© [2006] IEEE)

Nasilowski *et al*. [17] presented the design of a PCF with a triple defect and studied the temperature and pressure sensitivities. The geometry of the fiber is different that previously mentioned PCFs in that the fiber lattice has had two additional air holes removed and replaced with solid silica. This geometry in turn induces a large initial birefringence in the fiber by creating a fiber core with significant asymmetry and possessed an initial birefringence of $\sim 1.6 \times 10^{-3}$ at 1300 nm. When an applied hydrostatic pressure was applied, an induced birefringence of -5×10^{-7} at 800 nm was observed and the fiber possessed roughly two orders of magnitude less sensitivity to temperature than traditional HiBi fibers.

Chen *et al*. [18] proposed a novel method for creating a PCF with a large intrinsic birefringence by modifying a square lattice photonic crystal matrix into a rectangular lattice (RLPCF). This structure was created by increasing the PCF period along the y-axis and creates a birefringence of 1.5×10^{-3}. What is interesting about this particular fiber is that the x-polarization mode extends further out into the crystal matrix at lower frequencies.

Kim *et al*. [19] proposed a modification to the RLPCF by the addition of air holes into the rectangular lattice. This structure allowed for the birefringence of ~10^{-2} with significantly improved confinement of the optical mode, with leakage loss a few thousand times smaller than the RLPCF.

1.3 SUSPENDED CORE OPTICAL FIBERS

Suspended core optical fibers (SCFs) have continued the trend in fiber optics of applying unique holey structures to adjust the optical properties of the fiber. By adding large air holes in a concentric ring structure, it is possible to create fibers that contain the optical signal due to the high index contrast between the core material and the air holes. SCFs have been fabricated from tellurite, lead silicate and silica glasses with varying air hole structures and core diameters which has lead to fibers with high numerical apertures (NA~1.0), small mode-field diameter, low splice-transmission loss and large dispersion characteristics. Additionally, due to the nature of optical confinement, a large portion of the transmitted optical power (~20-30%) is present in the air holes. These unique traits have lead to the development of evanescent wave chemical sensors for gases and liquids, super-continuum generation, polarization maintaining (PM) highly nonlinear fibers, and fiber sensors with lower sensitivities to temperature and strain.

The first modern suspended core optical fiber was first reported in 2002 by Kiang *et al*. [20]. This fiber was created from Schott SF57, a glass with high lead concentration and a nonlinear refractive index component an order of magnitude greater than that of silica glass. The fiber was fabricated at lower temperatures due to the low softening temperature of the glass by

an extrusion method and then caned in a drawing tower. The method of fabrication presented allows for the elimination of stacking glass rods to make the fiber and allows for the creation of lower loss fibers. The resulting fiber can be seen in Figure 6.

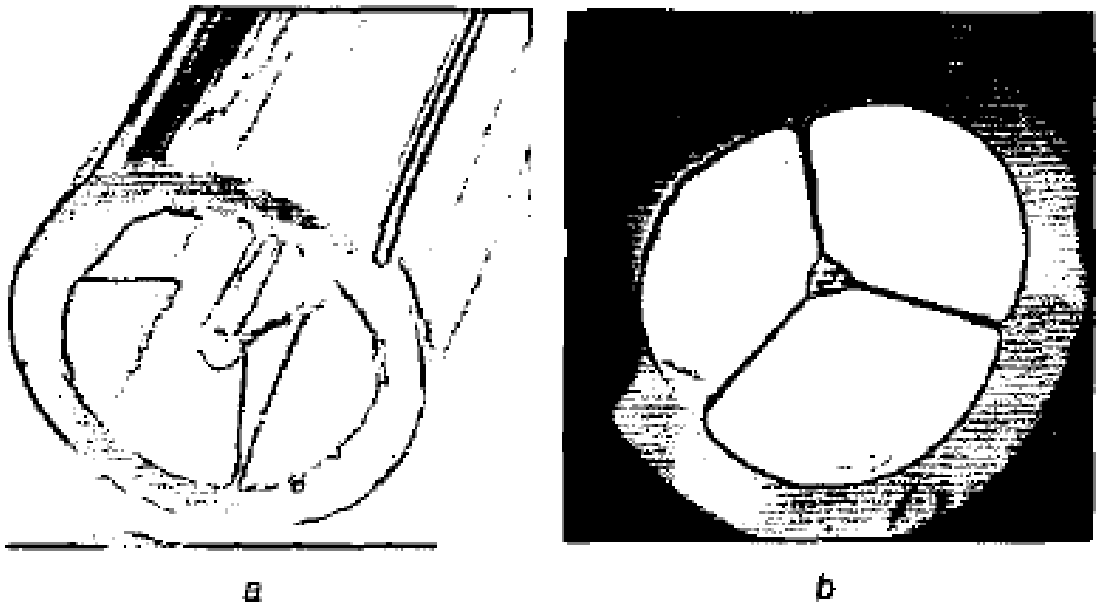

Figure 6: Photographs of preform and cane [20] (© [2002] IEEE)

Liao *et al*. created a suspended core fiber from tellurite for use in supercontinuum generation applications [20] via a fabrication process that employed the use of pump pressure to allow for a stable fiber drawing process. The fiber fabrication process required the creation of a cast rod for the bridge structure and a cast tube. The cast rod was inserted into the cast tube and drawn down to the desired size with nitrogen gas to maintain the fiber structure. The single material fabrication allowed for negligible loss in the fiber at 1700 nm and when 1557 nm light was pumped into the fiber single mode non-phase matched third harmonic generation was demonstrated.

Ebendorff-Heidepriem *et al*. demonstrated successful fabrication of lead silicate glass suspended core optical fibers [22]. The fabrication process revolved around a three-step process similar to Liao *et al*., however the overall achievable size of the fiber core region was smaller. In addition, the propagation loss in the fiber scales as the fiber core becomes smaller due to the surface roughness of the air holes inducing scattering.

Mukasa *et al*. demonstrated the first silica suspended core fiber [23]. Their method of fabrication revolved around the use of an ultra sonic drill to create three air holes in the fiber performs. This method of fabrication allows for the reduction of surface roughness in the preform and ease of fabrication. The fiber perform and final fiber cross-section is presented in Figure 7. The studied fibers were demonstrated to be low loss with a NA approximately to 1. Additionally, 25-30% of the optical power was carried within the air holes.

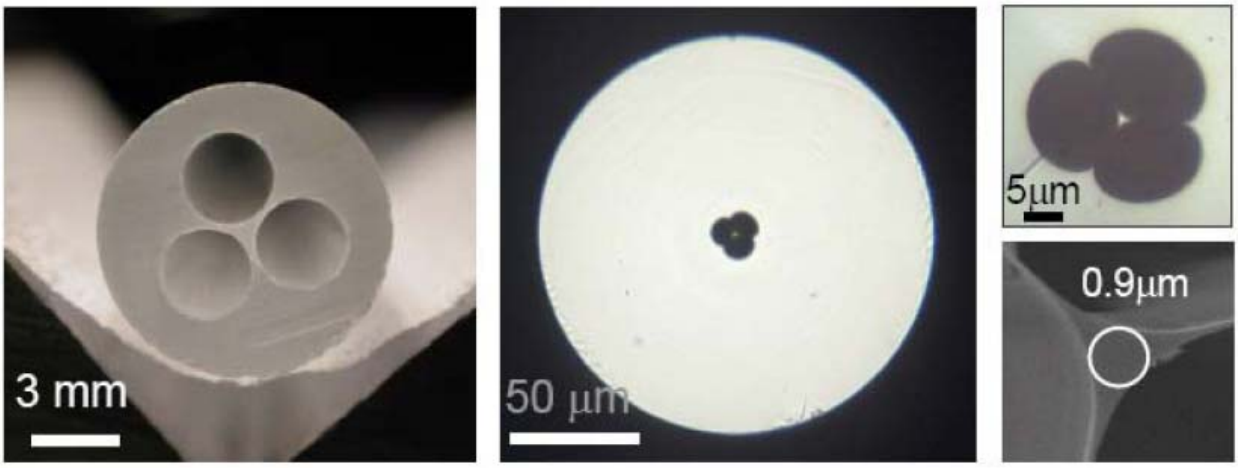

Figure 7: Fabrication of suspended-core holey fibre: drilled preform (left); drawn fibre (centre); magnification of the microstructured region (top right) and of the core (bottom right) [23] (© [2006] IEEE)

Webb *et al* performed work on evanescent field sensing with suspended core fibers [24]. The fiber was fabricated via the ultrasonic drill method, which allowed them to achieve silica bridge thicknesses of 0.2 μm. In addition, a correlation between the amount of optical power (at 1550 nm) contained within the air holes and the diameter of the fiber's core was demonstrated. To show the ability of this suspended core fiber to act as an evanescent field sensor a gas detection system was constructed to monitor the absorption of acetylene.

Dong *et al*. demonstrated a 6-hole suspended core fiber from silica [25] via the ultrasonic drilling method. This particular fiber geometry was able to produce fibers with a NA of 1.05. More importantly, it was demonstrated that by increasing the air cladding width it is possible to reduce the confinement loss. These fibers also demonstrated a low splice loss of 0.8 dB, the lowest confirmed to that point.

Tse *et al*. presented work on a 6-hole suspended core fiber with inscribed FBGs for use as a thermal and longitudinal strain sensor [26]. This fiber was different from the previously mentioned fibers, in that this fiber possessed a germanium-doped core. The FBG was inscribed using a KrF excimer laser and phase mask system. The FBGs produced in this fiber contained additional side peaks in addition to the central spectral peak. The occurrence of these side peaks is due to a variation in the air holes within the grating length. When exposed to an increasing temperature and applied longitudinal strain the FBG experienced lower sensitivities to each due to the decrease in the cross-sectional area of the fiber from the presence of the air holes. Figure 17 presents the strain response of the FBG in the 6-hole fiber and standard SMF-28.

2.0 BACKGROUND: PRESSURE SENSING AT ELEVATED TEMPERATURE

2.1 PREMISE

Power generation facilities and processes typically take place in harsh environments (>300C) which makes traditional sensing mechanisms difficult to deploy and have often included a probe tip that was coupled with a cooling or extraction system. There is a current need for high pressure monitoring at higher temperatures in order to obtain ideal operating parameters in real time while giving an entire system performance and lifetime health overview, including turbine operation, gas flow and overall integrity of the structures.

Sensor development must include additional considerations. The overall size of the sensor with respect to the packaging required for operation is necessary. Traditional pressure sensors are often bulky due to the package size typically required. The packaging is traditionally fabricated from stainless steel with either a male or female thread type for incorporation into the system. In order to compensate for higher temperatures, larger outer-casings are required. The power inputs and outputs for monitoring the pressure are multi-pinned connections or pre-connected to a cable. The feedthrough, casing and cabling in turn create a sensor that is typically between 10 and 20mm in width and several times that in length. The overall size of the sensor can cause difficulties for generation facilities and fuel cells as they have limited space available

for additional components. The large packaging required can make monitoring of smaller regions difficult or entirely impractical.

Power generation facilities have an abundance of electric machinery and transmission lines. These components in turn create an inherent amount of electromagnetic interference (EMI) due to their operation. In order to compensate for the EMI present in the environment, the packaging required can increase in size and require additional filter circuitry in order to ensure proper operation.

The number of sensors necessary for proper monitoring of the system and the intrusiveness of the sensor on the system must be considered. Complex systems typically can not be monitored with a single sensor and redundancy is almost always required. The size of the system and necessary redundancy dictate the number of sensors along with the overall placement. Feedthrough locations must be able to withstand operating conditions while connected to the control and monitoring systems being observed by the operator. Within harsh environments these feedthrough locations must be considered to ensure that the system does not suffer a structural degradation or a breach due to the seal failing.

From the above analysis it can be inferred that an ideal pressure sensor for high-temperature operation will not require bulky packaging, will not be susceptible to EMI and will allow for a single feedthrough multi-point sensing mechanism. We therefore propose the use of fiber Bragg grating (FBG) sensors in microstructured optical fiber for use as pressure sensors in high-temperature environments. FBG sensors are immune to EMI and do not require the bulky packaging required for traditional pressure sensors. In addition it is possible to multiplex several sensors onto a single length of optical fiber, allowing for only a single feedthough.

In this chapter I will review current state of the art technologies currently being developed for the monitoring of pressure in harsh environments. Including capacitive and piezoresistive pressure sensors, Fabry-Perot sensing techniques and current work on the development of microstructured optical fibers (MOFs) for pressure sensing will be presented

2.2 LITERATURE REVIEW

There is a great demand for pressure sensing mechanisms that have the ability to function in high temperature environments (>300C) in the oil, natural gas and nuclear power industries. Proper pressure monitoring is necessary to ensure safe and efficient operating conditions. However, the harsh temperatures in which the equipment operates pose significant challenges in deployment of sensing systems. Over the last decade there has been significant work performed in the manner of creating sensors that can monitor pressure in a harsh environment, including capacitive pressure sensors, peizoresistive pressure sensors, and extrinsic Fabry-Perot interferometer (EFPI) sensors.

Capacitive pressure sensors are MEMS devices that are created by suspending a diaphragm over a sealed cavity on a substrate creating a parallel plate capacitor. When a pressure is applied the diaphragm deflects downward, decreasing the distance between the diaphragm and the dielectric layer. This decrease in spacing induces a change in the capacitance and is given by $\Delta C = \frac{\varepsilon_0 A}{d^2}\Delta d$. Where ε_0 is the permittivity of free space, A is the area of the electrodes and d is the distance between the electrodes in the device [27-30]. A cross-sectional view of such a

device is presented in Figure 8. The two methods used to fabricate these sensors for high temperature operations require either the use of ceramic or silicon carbide (Si-C) diaphragms.

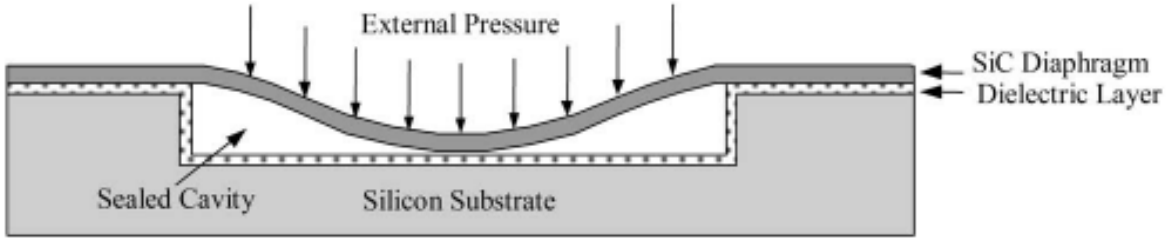

Figure 8: Cross-sectional view of Si-C capacitive pressure sensor [27] (© [2004] IEEE)

Sippola *et al.* [28] present a ceramic capacitive pressure sensor based upon thick film screen-printing. The use of ceramic components is due to their high temperature properties and their use in the microelectronics industry for over 30 years. The sensor was fabricated by using a thick-film approach employing the use of a sacrificial layer in order to create the cavity necessary for operation. Vias were laser drilled into an alumina substrate in order for the etchant to reach the sacrificial layer. The bottom electrode was fabricated by a screen-printing process using gold, the sacrificial layer was created in the same manner. The diaphragm is then screen-printed and the sacrificial layer is then removed by etching. A diagram of this process and the resultant device are presented in Figures 9 and 10, respectively. The sensor was exposed to pressure tests up to 50psi and a maximum temperature of 300C due to experimental limitations. The device materials and construction suggest that this pressure sensor could work at higher temperatures. However, the device experiences significant limitations in that it operates at low pressures and requires hermetic seals for proper operation.

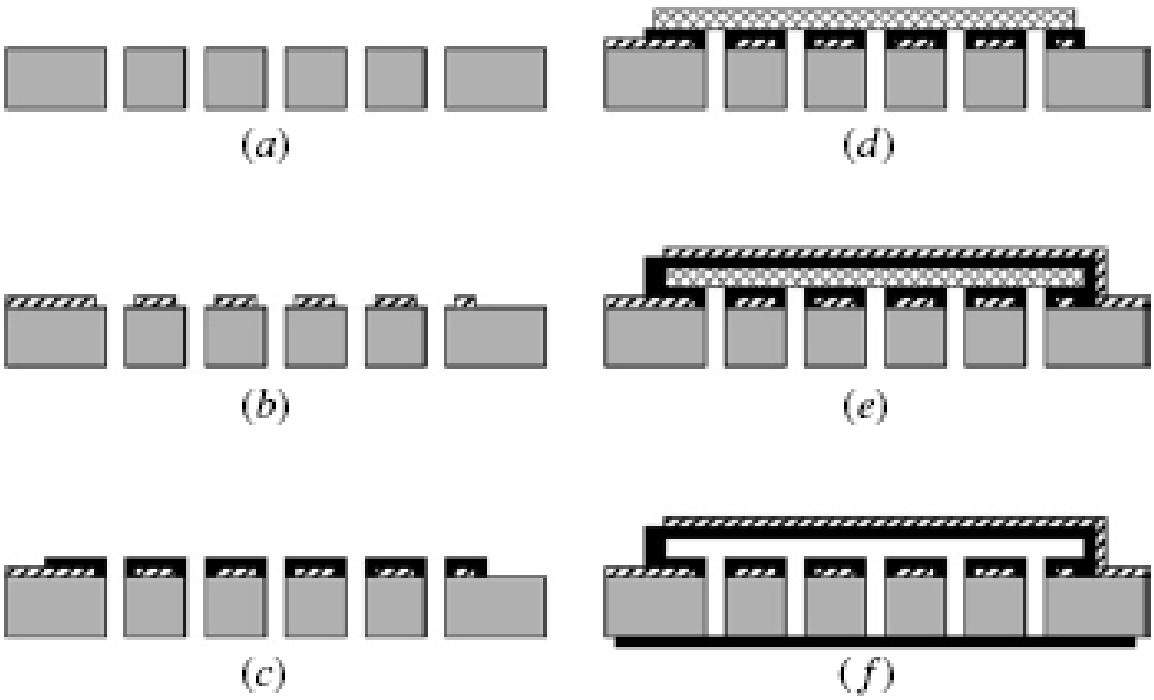

Figure 9: Ceramic cavity and sensor fabrication steps: (a) step 1 – laser drilling of through ceramic vias; (b) step 2 – screen-print bottom electrode; (c) step 3 – screen-print bottom dielectric layer; (d) step 4 – screen print sacrificial layer; (e) step 5 – screen-print top dielectric diaphragm and top electrode and (f) step 6 – etch sacrificial layer and screen-print backside sealing dielectric [28] ((c) [2006] IEEE)

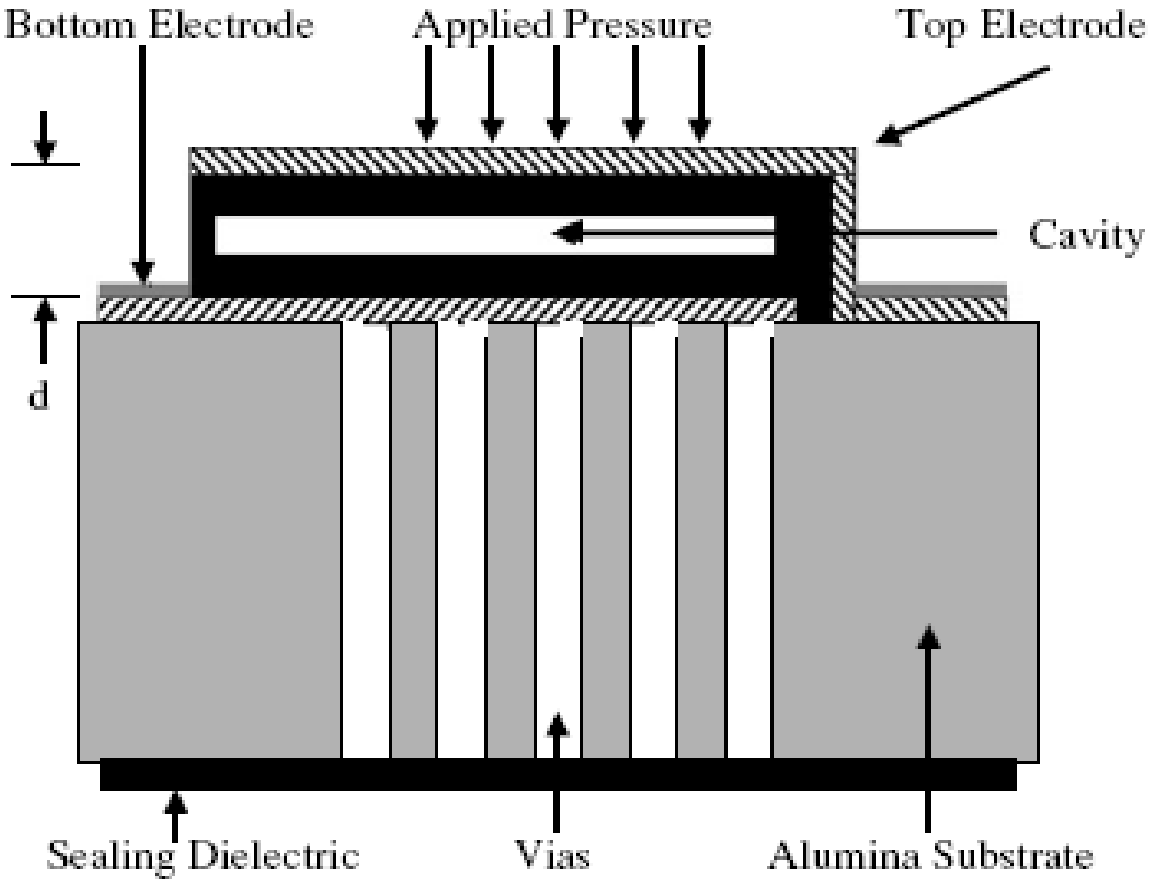

Figure 10: Schematic diagram of ceramic pressure microsensor [28] ((c) [2006] IEEE)

A wireless ceramic pressure sensor was reported by Fonesca *et al.* [29] that consisted of two ceramic diaphragms separated by an air-cavity that is then connected to a planar spiral inductor coil creating a LC resonator. The device is presented in Figure 11. The LC resonator possesses a resonant frequency ($f_0 = \frac{1}{2\pi\sqrt{LC}}$) which is pressure dependant due to the change in capacitance with an applied pressure. The device was fabricated using sheets of ceramic tape and the inductor coils and electrodes were fabricated using a screen-printing process. The overall size of the final device is 3.8cm square. The sensor was able to operate at temperatures between 25 to 400C and was tested up to an applied pressure of 7 bar (101.7psi). The pressure test was also performed up to 100 bars (1450psi) and continues to experience a linear response to the pressure. The major disadvantage is while a wireless sensing device is proposed the device requires the use of an antenna. The antenna adds another needed component that is susceptible to EMI. In addition the antenna can only be placed outside the pressurized chamber if there is no metal between the antenna and the sensor

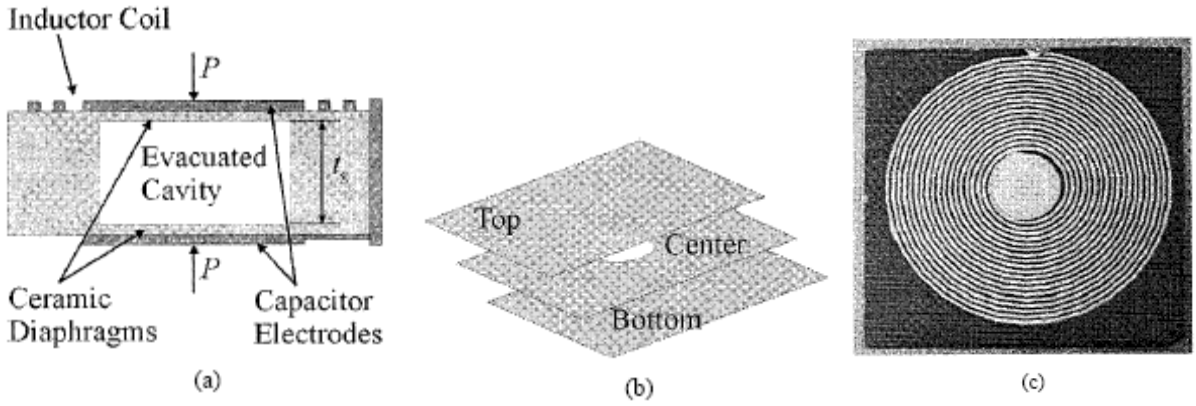

Figure 11: Schematic cross section (a), layered construction (b), top-view photograph of a ceramic pressure sensor with silver screen printed conductors [29] ((c) [2002] IEEE)

A high pressure, high temperature capacitive pressure sensor for in-cylinder monitoring was developed by Chen *et al.* [30] using a Si-C diaphragm. The sensor design is the same as was presented in Figure 8. The fabrication technique employed the sacrificial layer method that has been previously mentioned. For the high temperature operation (>300C) a specialty a hybrid high-temperature ceramic dual-in-line package (DIP) was necessary to reduce bulk CMOS degradation of the amplifier circuit for the pressure sensors. The sensor was exposed to an applied temperature of 300C and a pressure up to 5MPa (700psi) and experiences a linear pressure monitoring range of 1.4 to 3.2MPa (200-450psi). Higher temperature testing up to 574C up to 100psi was then performed. The major disadvantage of this device is in the necessary inclusion of the DIP package. In addition to the increase in overall size the DIP package requires a 4-wire input-output (I/O) configuration for operation.

Another approach to monitor pressure is to use piezoresistive pressure sensors, which are DC MEMS devices fabricated using standard silicon-on-insulator (SOI) technology [31-34]. The device operates by the applied pressure acting upon a silicon membrane with piezoresistors connected in a Wheatstone-bridge configuration. An example of the Wheatstone-bridge is given in Figure 23. When the device experiences an applied pressure the resistance changes due to an unbalance in the bridge and can be measured by a change in the output DC voltage. The change in the output voltage is given by $\Delta V = \frac{r}{(1+r)^2}\left(\frac{\Delta R_1}{R_1} - \frac{\Delta R_2}{R_2} + \frac{\Delta R_3}{R_3} - \frac{\Delta R_4}{R_4}\right)V_{in}$, where $r = R_2 / R_1 = R_3 / R_4$ [30].

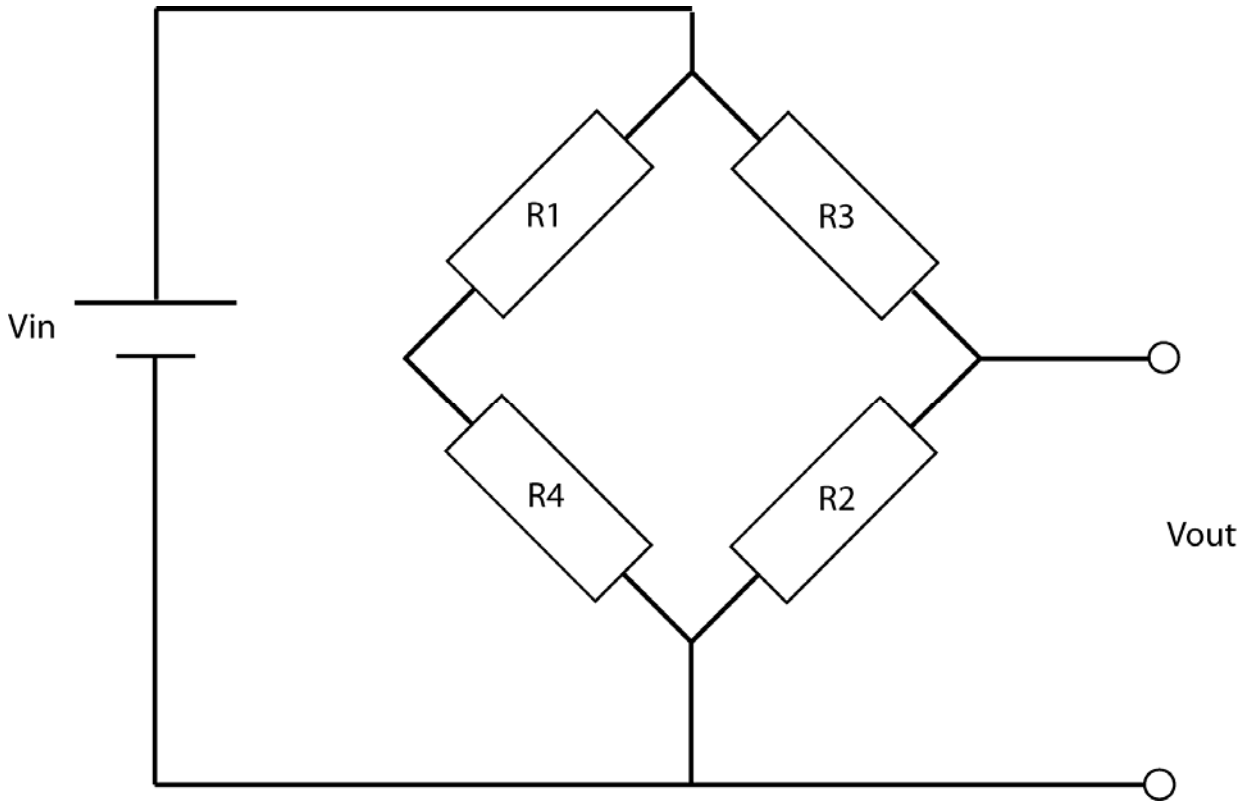

Figure 12: Wheatstone-bridge circuit configuration

A high temperature peizoresistive pressure sensor for operation in high frequency sensing environments was developed by Zhao *et al.* [32] The sensor was fabricated using the separation by implantation of oxygen (SIMOX) technique to ensure low leakage currents at temperatures above 200C. LPCVD was used to ensure proper film thicknesses for piezoresistivity operation and the Wheatstone bridge was created with reactive ion etching (RIE). The SOI sensor was then bonded to Pyrex rings that connect to a SOI silicon flat chip. The sensor was exposed to an increasing pressure up to a maximum of 25MPa (3625psi) at 20 and 200C and experiences a linear trend with respect to the increasing pressure. The disadvantages of this sensor are the fabrication processes and the final size of the sensor. The fabrication process requires many steps including the implantation of oxygen, RIE and bonding to a glass ring. The size of the device on the created chip is 2 mm, however the required packaging for operation is much larger and only allows for the monitoring of a single point.

Guo *et al.* [33] presented a peizoresistive pressure sensor for high temperature operation. The high temperature operation was accomplished by using very thin active layers as to avoid leakage effects that occur at higher temperatures in p-n junction devices. The sensor operates in a Wheatstone-bridge arrangement that was previously mentioned. The sensor was coupled with a temperature-sensitive resistor in order to monitor the applied temperature to the device. Platinum wires were used as the wire feedthroughs for the device as platinum has a natural ability to withstand elevated temperatures. The sensor had an upper pressure limit of 600psi up to a maximum temperature of 600C. This sensor was able to withstand an applied temperature of 500C for 50 hours with good stability. The sensor was also shown to respond to an applied pressure at temperatures up to 700C for a limited time duration. The disadvantages of this

device are again the final size of the package and ability to only monitor a single location. In addition the sensor requires the use of platinum wires as feedthroughs, in turn adding a significant increase in the cost of the sensor. The sensor schematics and device are shown in Figure 13.

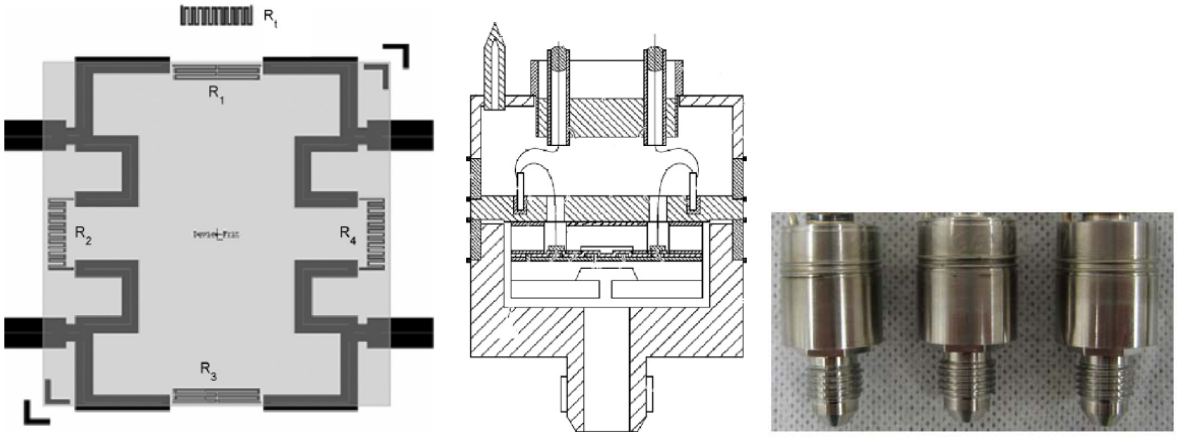

Figure 13: Plane view of piezosensor (left), schematic of packaged high temperature pressure sensor (center) and photograph of sensor package (right) [33]

Another method of monitoring pressures is the use of an extrinsic Fabry-Perot interferometer (EFPI) sensor [34-36]. These sensors are an optical method that can be used to monitor a pressurized environment. An EFPI is created by forming a low-finesse Fabry-Perot cavity between a polished end facet of an optical fiber and a reflective surface. This setup can be used to monitor pressure by using a pressure sensitive membrane as the reflective surface so that when a pressure is applied the path length between the fiber end and reflective surface will change. The change is path length will cause the two reflected light waves to interfere constructively or destructively causing a variation in the interference pattern. This relationship is given by $I_r = |A_1 + A_2|^2 = A_1^2 + A_2^2 + 2A_1A_2\cos(\phi_1 - \phi_2)$, where I_r is the optical power returned from the sensor, A_1 and A_2 are the amplitudes of the two reflected signals and ϕ_1 and ϕ_2 are the phases

of the reflected signals. A diagram of an EFPI and an example interference pattern are shown in Figure 14.

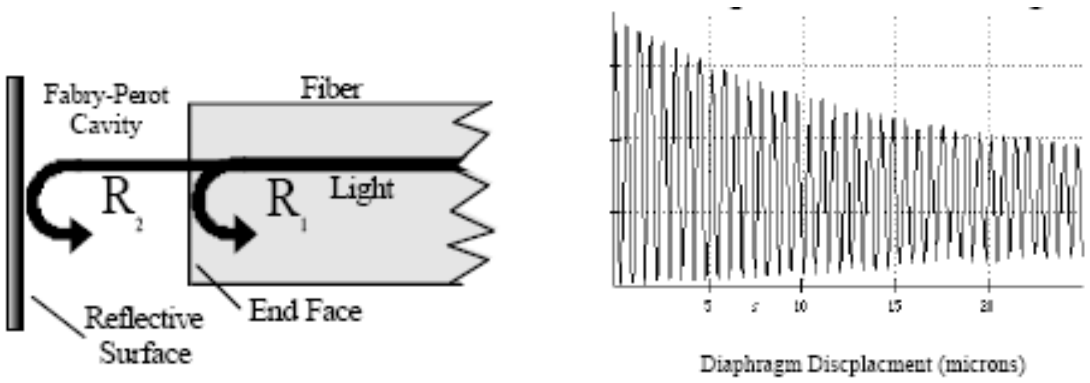

Figure 14: Extrinsic Fabry-Perot setup (left) and output with change in diaphragm (right) [34] (© [2001] IEEE)

Borinksi *et al*. [34] developed an EFPI system for aircraft health monitoring. The sensor was fabricated by epoxying the optical fiber to a Pyrex base with a silicon diaphragm as the reflection surface. A schematic of the device is presented in Figure 15. The sensor experienced no thermal shift with an applied temperature of 300C and was shown to properly operate up to temperatures of 600C with a pressure range from 0 to 16psi applied pressure. The sensor was also shown to have a high frequency operation. While the EFPI device does not suffer from EMI interference as is common among IC and MEMS pressure sensors the device package is significantly larger than the actual optical fiber and allows for only a single point of measurement within the high pressure system.

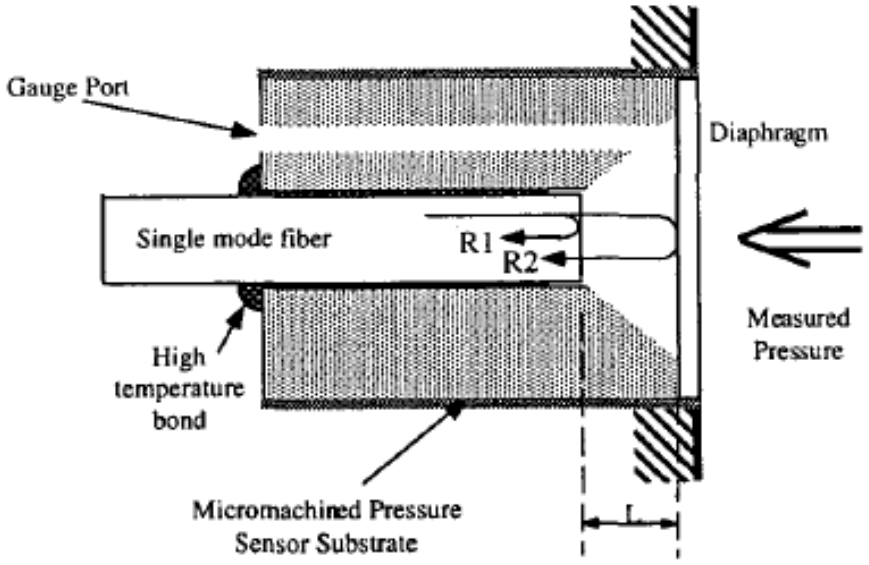

Figure 15: Schematic of fiber-optic pressure sensor [34] (© [2001] IEEE)

An EFPI with a fiber Bragg grating (FBG) pressure sensor and temperature multiplexed sensor system was presented by Wang *et al.* [35] for use in down-hole measurements. The sensor was fabricated by bonding the pristine fiber and the fiber containing the FBG in a glass capillary tube using a CO_2 laser. The gap between the fibers in turn creates the Fabry-Perot cavity with the end facet of the one fiber acting as the reflective surface. This configuration allows for the monitoring of pressure and temperature simultaneously. The configuration and reflection spectrum of this system is presented in Figure 16. The sensor allows for the detection of a temperature change by monitoring the shift of the FBG resonant peak while the interference pattern accounts for a change in the pressure. The sensor was immersed in a pressure transfer liquid for characterization. The sensor was exposed to a pressure and temperature range from 0 to 30MPa (4351psi) and 18-300C, respectively. Over a 300 hour time span the pressure and temperature sensitivities of the sensor were reported as 0.5MPa (43.5psi) and 0.5C. This sensor

design has the ability to monitor both pressure and temperature simultaneously, including the possibility of multiplexing several FBGs for the monitoring of temperature at several points. However, the pressure sensing mechanism only allows for the monitoring of pressure at a single point, resulting in the necessary inclusion of multiple feedthroughs for the monitoring of pressures at multiple locations.

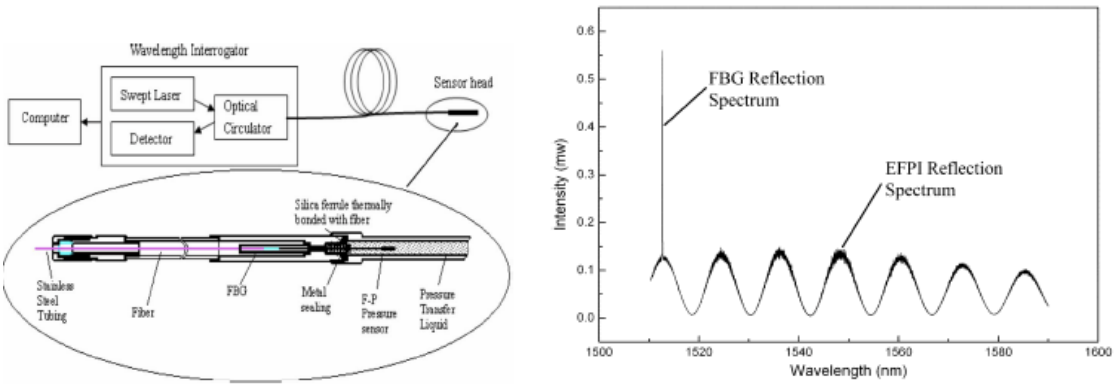

Figure 16: Configuration of FBG-EFPI combined temperature and pressure multiplexing sensor system (left), reflection spectrum of FBG-EFPI mulitplexed sensor (right) [35] (© [2004] IEEE)

Development of a high-temperature EFPI pressure sensor employing an alumina probe tip was developed by Fielder *et al.* [36] using a Si-C membrane. The sensor consisted of a length of stainless steel tube that acted as a heat sink for the optical components of the sensor, allowing for operations at higher temperatures. The probe length allows for a varied length based upon the optics available for the monitoring. The alumina tip allowed for the monitoring of pressure in a hot zone of 1100C while protecting the optics which were limited to 800C. The sensor was successfully demonstrated at a temperature of 800C and up to a pressure of 500psi. The EFPI presented also had the ability to function as a high-temperature sensor using Si-C and sapphire membranes. The sapphire membrane was demonstrated to operate to a maximum temperature of 1070C. The Si-C and sapphire membranes had accuracies of ±0.5C and ±1.6C, respectively.

The summarized advantages, disadvantages, and maximum pressure and temperature ranges are presented in table 1 for the capacitive, piezoresistive and EFPI pressure sensors.

Table 1: Summary of current state of the art pressure sensors

	Advantages	Disadvantages	Pressure Maximum	Pressure Sensitivity	Maximum Operating Temperature
Capacitive Pressure Sensor	Fabricated using traditional microelectronics process Materials have excellent high temperature characteristics High sensitivity	Single point sensor Fragile impedance wiring Requires larger packaging for deployment Cavity needs to be vacuum sealed Mostly low pressure operation (<100psi)	Max pressure: 1450psi	7.2fF to 9.2fF/psi	574C 300-400C typical maximum operating temperature
Piezoresistive Pressure Sensor	Fabricated using standard SOI technology DC output with low cost circuitry	Single point sensor Temperature dependence on pressure sensing Packaging size can be significant	Max pressure: 3625psi Dynamic Operation: 725psi	0.42mV/psi (25C) 0.29mV/psi (500C)	500C 700C for limited duration
EFPI Pressure Sensor	EMF immunity High Temperature operation High Pressure range Can also measure temperature	Single point sensor Fabrication and packaging much larger than actual sensor	Max pressure: 4351psi	±0.25psi (Max pressure: 500psi) 43.5psi resolution (Max pressure: 4351psi)	Silicon diaphragm: 300C Si-C diaphragm: 800C Sapphire diaphragm: 1070C

While the above mentioned pressure sensing technologies all have their advantages, a common trend is constant among them in that they are all single-point sensors that require multiple feedthrough locations for larger system monitoring. In order to overcome this disadvantage fiber Bragg grating (FBG) sensors can be deployed as a pressure sensing mechanism. The advantage of FBGs is that on a single length of optical fiber multiple gratings can be inscribed allowing for a multi-point sensing system with only a single feedthrough. In addition, FBGs are fabricated from silica fiber that is intrinsically immune to EMF interference, eliminating much of the packaging requires for IC and MEMS sensors. Over the past several years strides have been made in optical fiber research in order to create FBG pressure sensors that have the ability to operate in harsh environments.

Solid optical fiber possesses an inherent low sensitivity to transverse loads such as an applied pressure. In order to overcome this limitation the addition of air-holes in the fiber cladding was first proposed by Xie *et al.* [2] to create an optical fiber pressure sensor. The fiber designed had an outer diameter and air-hole diameter of 190μm and 58μm, respectively. The ideal cross-section, model of the fiber and cross-sectional photograph are presented in Figure 17. It was shown that there exists a pressure dependency upon the birefringence in the fiber.

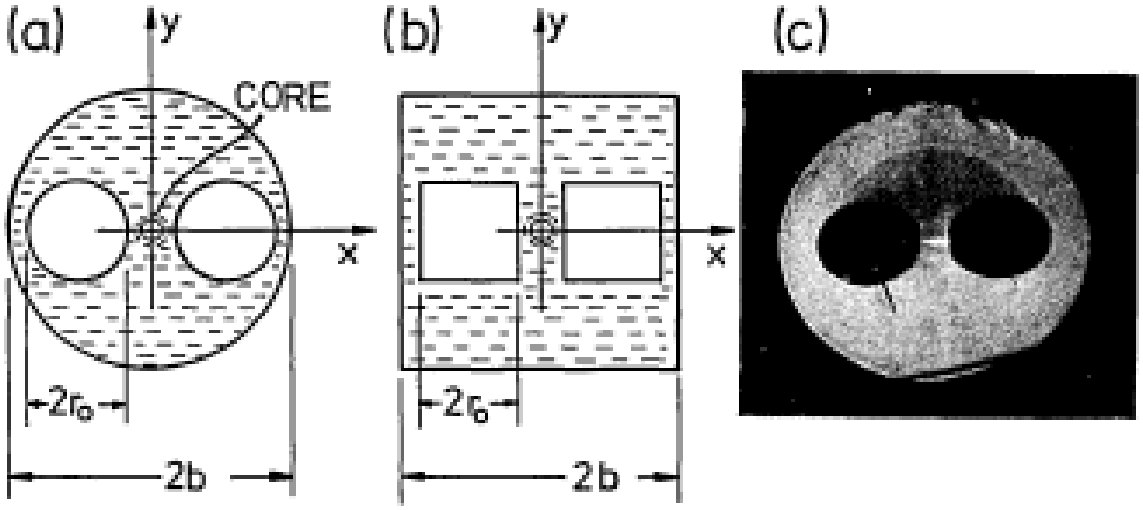

Figure 17: (a) Cross section of side-hole fiber. (b) Square model of side-hole fiber, used for approximate calculations. (c) Photograph of experimental fiber: approximate dimensions 2b = 190µm; 2ro = 58µm. [2]

Schroeder *et al*. [37] presented a high pressure FBG sensor inscribed in side-hole optical fiber in comparison to standard Corning SMF28 and polarization maintaining (PM) fiber. Side-hole fiber is a length of SMF28 that has had two air-holes fabricated in the cladding of the fiber. The fiber used for this research had two 35µm diameter air-holes in the cladding. Gratings were inscribed into the three different fibers which were then inserted into a high pressure vessel. Experimental tests were performed from 0 to 12000psi and 25 to 100C. For the three fibers there was an increasing linear shift with the applied pressure with the side-hole fiber having the greatest shift. The side-hole fiber then underwent pressure and temperature tests in which the birefringence between the two polarizations was monitored to determine the pressure. It was shown that at increasing temperatures the birefringence in the side-hole fiber was constant with only an applied pressure causing an effect.

Yamate *et al*. [38] demonstrated a thermal insensitive FBG in side-hole fiber for pressure sensing up to 300C. Lengths of SMF28 were fusion spliced to the ends of the side-hole fiber in

order to keep fluid from entering the holes during the experiment. The fiber with the FBG was inserted into a high pressure tube via feedthrough that was filled with lubricating oil. The sensor was exposed to an applied pressure of 8000, 10000 and 12000 psi at a temperature of 300C and experienced a constant 0.06pm/psi sensitivity. The overall temperature sensitivity was reported as being -0.03pm/C at 12000psi applied pressure which is approximately 300 times less than traditional FBG temperature sensors.

In this chapter, a literature review of current state-of-the-art pressure sensors for high temperature environments was discussed. The types of sensors discussed were capacitive, piezoresistive and SOI pressure sensors. Their advantages and disadvantages were discussed. An alternative solution using two-hole microstructured optical fibers was presented, along with current applications to pressure monitoring.

3.0 PRESSURE SENSING USING AIR-HOLE MICROSTRUCTURED FIBERS FOR HIGH-TEMPERATURE ENVIRONMENTS

Fiber Bragg gratings (FBGs) have received considerable attention as application specific sensors, due to their small size, electromagnetic interference immunity and multiplexing ability. More recently, microstructured optical fibers have been developed allowing for the design of fiber geometries that can allow for the monitoring of transverse loads in addition to axial loads. The two-hole microstructured optical fiber has shown great promise for the monitoring of an applied hydrostatic pressure due to the fiber geometry's ability to focus the induced stresses into the fiber core region.

Despite the benefits of using side-hole (two-hole) fiber as a pressure traducing mechanism, deploying these sensors is still limited by their upper temperature limit. The upper limit of FBGs is primarily because traditional FBGs written using the UV phase mask method in hydrogen loaded fibers are not well suited for temperatures above 400C due to instability in the grating and the trend of the grating to be washed out at higher temperatures. In order to overcome the temperature limitation Type II gratings written by an ultrafast laser have been demonstrated to operate just below the annealing point of fused silica (1140C) [39].

In order to create the most sensitivity pressure sensor possible finite element analysis (FEA) was performed to optimize the overall geometry of the two-hole fiber, specifically the placement of the fiber's core and the overall size of the air-holes. Hydrostatic pressure

monitoring testing was performed on different fiber geometries at room temperature in order to confirm the simulated results. Ultra-high temperature testing was performed with gratings written in SMF28 via an ultrafast laser for overall operation verification. Two-hole fiber was then inscribed with a grating using an ultrafast laser for monitoring of a transverse pressure at ultra-high temperatures. The limitations of the two-hole FBG at 1000C are presented along with further improvement upon the traditional two-hole fiber geometry.

3.1 FEA SIMULATION OF TWO-HOLE FIBERS UNDER A HYDROSTATIC PRESSURE

In order to properly predict the effect of an applied transverse pressure would have on our microstructured optical fiber, finite element analysis (FEA) was performed. FEA is a numerical method that discretizes a solid body allowing for structural analysis, including deformations and induced internal forces throughout the structure.

For a typical solid bodied structure it is not possible to easily obtain a solution due to the mathematical expressions determining the unknown parameters at any point within the body of the structure. These mathematical solutions consist of differential and partial-differential equations and can be quite complicated. Therefore, one must employ the use of FEA in order to obtain the solutions. FEA allows for the creation of simultaneous algebraic equations eliminating the need to solve differential equations by solving for the desired unknowns at discrete points throughout the structure. Therefore the operating principle behind FEA is to take a single solid body and in turn reduce it into several smaller bodies or “elements” connected to

one another via nodes, boundaries and surfaces. The solution method used by FEA is to determine the displacements and forces throughout the structure at each node in the presence of an applied load.

For modeling of an optical fiber cross-section under an external pressure it is possible to greatly simplify the geometry of the problem by reducing it to a two-dimensional problem. This reduction is possible because of the plain strain assumption from the generalized theory of elasticity. Plane strain is defined as a state of strain in which the normal strain to the X-Y plane (ε_z) and the associated shear strains (γ_{xz}, γ_{yz}) are assumed to be zero. The plane strain assumptions are valid for a long body along the Z-axis that possesses a constant cross-section in which the loads only act in the X-Y plane and are constant along the Z-axis. From this definition it is possible to see how the plane strain assumptions are ideal for the modeling of optical fiber under an applied transverse pressure as the length of the optical fiber containing the FBG is significantly longer (1 cm) than the diameter of the fiber (220 μm) and the hydrostatic pressure applied is constant along the entire length of the fiber [40, 41].

When a transverse pressure is applied to a two-hole fiber the air-holes deform under the applied load. Under this deformation the stress is focused between the air holes in the region containing the fiber core. Employing FEA it is possible to predict the effect an increasing load will have on the fiber and in turn use the induced stresses to predict the birefringence that will occur in the spectral response of the grating. For these simulations an optical fiber with an outer diameter of 220 μm with two 90 μm air holes and a 16 μm spacing between the holes was chosen.

The simulations on the pressure response were performed using the FEA software package ANSYS v. 11.0. The fiber model was created to take advantage of the fiber's symmetry

about the X and Y axes that when meshed would create a more uniform and symmetric mesh. It is necessary to use the proper material properties in the correct unit system for the analysis that is to be performed. This analysis was performed in the μMKS system of units and the needed material properties of fused silica [40] are presented in Table 2.

Table 2: Fused silica material properties in μMKS units

Young's Modulus (E)	74.52×10^{3} MPa
Density	2.201×10^{-15} Kg/μm^3
Poisson's ratio (ν)	0.17

The model was meshed using the PLANE183 element, a higher-order two-dimensional, 8 node element that has degrees of freedom in the X and Y planes that is well suited for modeling irregular shapes such as the edges of the fiber and air-holes. The fiber was meshed with an element size of 5 μm which was used for the majority of the fiber. In order for a more accurate model of the bridge spacing between the two air-holes a refined mesh of 2 μm was used. The model was constrained about the origin, in that the node at location 0, 0 would not experience any displacements. The hydrostatic load was applied to the outer edge of the fiber and varied up to a maximum of 200 bars applied pressure. The birefringence at an applied load of 200 bars is presented in Figure 18.

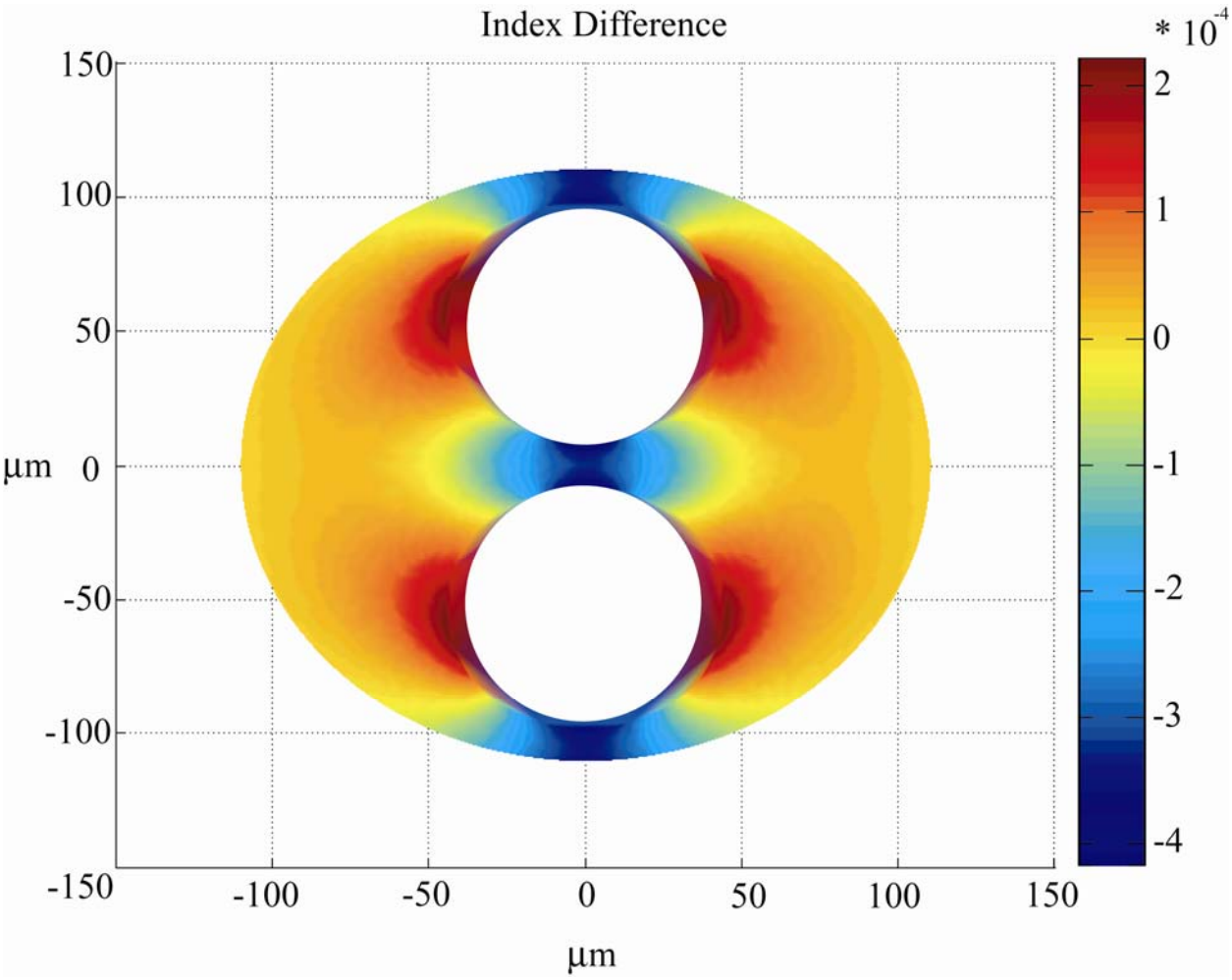

Figure 18: Birefringence of two-hole fiber at 200 bars applied pressure

The birefringence through the fiber cross-section was created via the output files from ANSYS and then imported into MatLab. The birefringence was calculated via Δn_x- Δn_y in which Δn_x and Δn_y are calculated from the following equations developed by Gafsi and El-Sharif [40].

$$\Delta n_x = -\frac{n_{eff}^3}{2E}\left\{\left(p_{11} - 2\nu p_{12}\right)\sigma_x + \left[(1-\nu)p_{12} - \nu p_{11}\right] * \left[\sigma_y + \sigma_z\right]\right\} \qquad (3.1)$$

$$\Delta n_y = -\frac{n_{eff}^3}{2E}\left\{\left(p_{11} - 2\nu p_{12}\right)\sigma_y + \left[(1-\nu)p_{12} - \nu p_{11}\right] * \left[\sigma_x + \sigma_z\right]\right\} \qquad (3.2)$$

Where n_{eff} is the effective index of the fiber, p_{11} and p_{12} are the Pockel's coefficients and $\sigma_x, \sigma_y, \sigma_z$ are the associated stresses induced from the applied load. Figure 32 depicts that when a transverse pressure is applied to a two-hole fiber the air holes deform under the applied load. Under this deformation the stress is focused between the air holes in the region containing the fiber core. Figure 19 is presented for a clearer understanding of the stress profile between the two air-holes. In addition to the 220 μm air-hole fiber, the birefringence for a fiber with an outer diameter of 125μm with the same diameter-to-hole aspect ratio is presented.

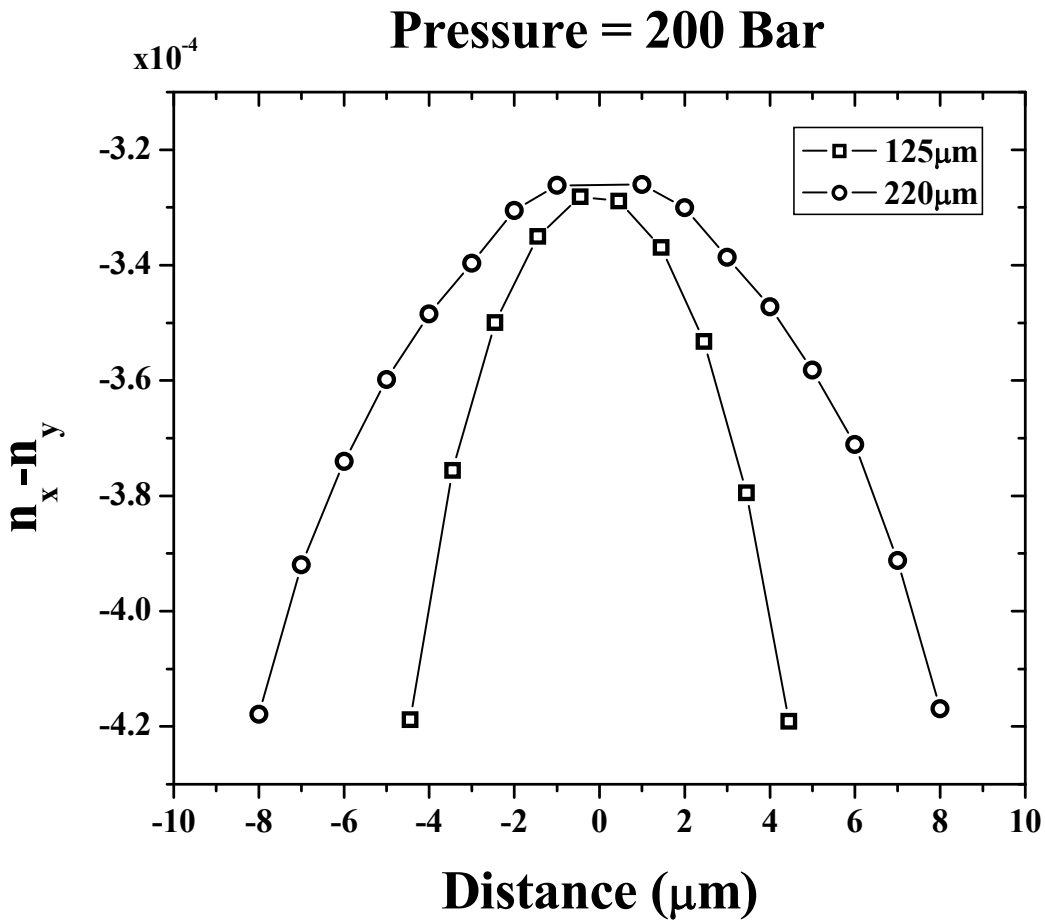

Figure 19: Birefringence between air holes for fiber for 220μm fiber and scaled down 125um fiber

The simulations signal that the farther from the edge of the air-hole the core is placed the smaller the birefringence. At the edge of the air-hole the simulated birefringence is -4.2×10^{-4} and decreases to -3.3×10^{-4} at the geometric center of the fiber. This suggests that in order to create a two-hole fiber possessing the highest possible sensitivity the fiber core should be placed as close as possible to the edge of one of the air-holes.

Also of importance is the effect the scaling of the fiber had on the overall sensitivity of the fiber. When the fiber was scaled down to 125 μm with the same aspect ratio there was not a noticeable change in the induced birefringence from the same applied load of 200 bars. The same sensitivity to pressure suggests that it is possible to fabricate smaller diameter microstructured fibers without sacrificing the overall sensitivity to the pressure, allowing for greater ease in fiber splicing and packaging.

It was next decided that simulations should be performed on the two-hole fiber by varying the size of the air-holes. These simulations were accomplished by reducing the overall size of the air-holes. A reduction in the size of the air-holes was chosen because the 90 μm diameter air-holes can not be increased much more without sacrificing the structural integrity of the fiber. The size of the air-holes was varied from 77 μm to 88 μm to allow for a large enough differential in the air-hole sizes. The air-hole to pressure sensitivity is presented in Figure 20.

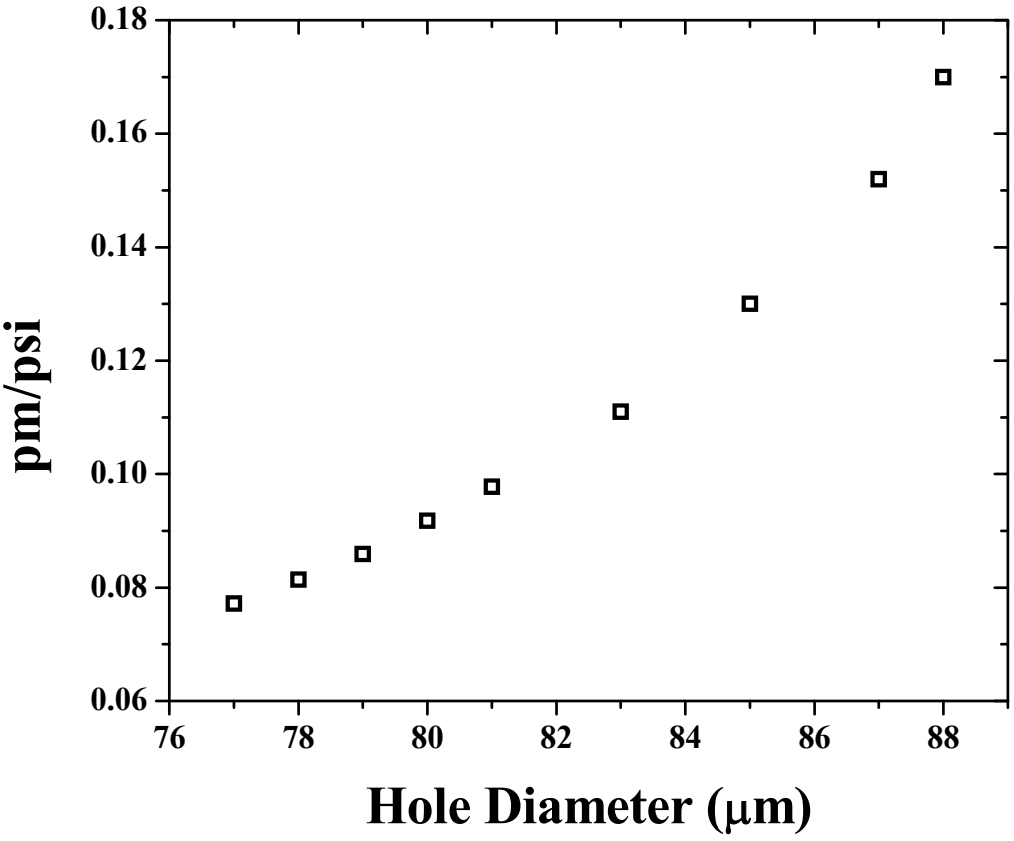

Figure 20: Simulated pressure sensitivity with increasing air-hole diameter

The overall sensitivity of the fiber increases significantly as the air-hole diameter increases. The increase in the sensitivity is due to a smaller bridge spacing between the air-holes, which in turn creates a higher stress profile in the core region of the fiber.

3.2 HYDROSTATIC PRESSURE TESTING AT ROOM TEMPERATURE

In order to properly verify the simulations, two fiber cross sections were chosen with different core placements. The two fibers can be seen in Figure 21 for the Fiber 1 and Fiber 2 respectively. Fiber 1 has a core 9.8 μm x 7.5 μm fabricated on the edge of one of the air holes while Fiber 2 has a core 10 μm x 4 μm fabricated 4 μm from the edge of the air hole. Both fibers possessed an overall geometry of 220 μm diameter, 90 μm air holes with a bridge spacing of 16μm.

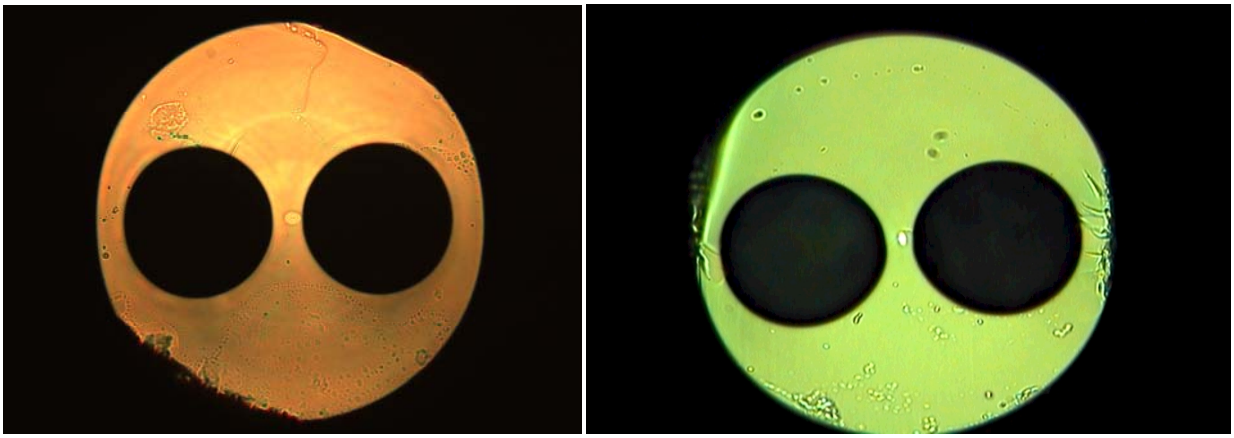

Figure 21: Microscope image of Fiber 1 (left) and Fiber 2 (right)

FBGs were written in both fibers using the standard phase mask inscription technique with a 248 nm KrF excimer laser. The fibers were first hydrogen loaded at 1900 psi for one

week in order to increase their photosensitivity. After the writing process the gratings were annealed at 120C for 24 hours in order to out diffuse any remaining hydrogen. All gratings were 1cm in length and were apodized to eliminate additional side lobes from the resonant peak.

The hydrostatic pressure experiment was performed using a sealed stainless-steel chamber. The length of two-hole fiber containing the FBG was fed through the chamber with both ends being sealed by ceramic ferrules. The internal pressure of the chamber was monitored via an external pressure gauge. The two-hole fiber was then fusion spliced to a length of SMF28 that was connected to a circulator. An OSA and ASE broadband source were connected to the circulator. On the OSA side a U-bench was inserted with a half-wave plate and a Glan-Thomson polarizer in order to observe the individual polarizations during the experiment. By rotating the wave plate it is possible to individually select one of the two orthogonal polarizations in the fiber. The experimental setup can be seen in Figure 22.

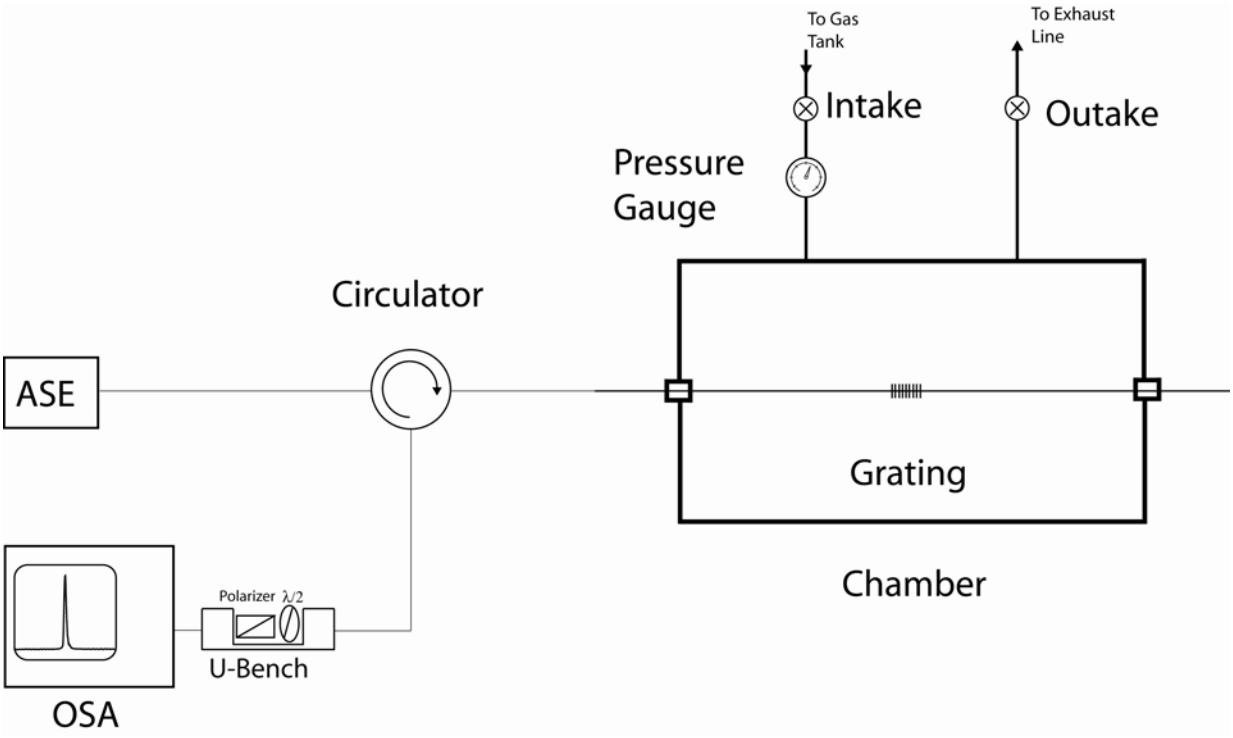

Figure 22: Experimental setup for hydrostatic pressure sensor at room temperature

The pressure was then ramped from room pressure up to 1900 psi. The pressure was limited by available pressure of our nitrogen tank. After the birefringence at 1900 psi was observed the pressure was released and re-applied in order to observe repeatability.

The spectral response of the FBGs can be seen in Figs. 23 and 24 for Fiber 1 and fiber 2, respectively. Under the applied pressure the base reflection spectrum for both fibers splits into two well defined peaks. Using the U-bench, polarizer and wave-plate it is possible to individually select each individual polarization, thus confirming that the applied pressure is in fact inducing a birefringence in the fiber core.

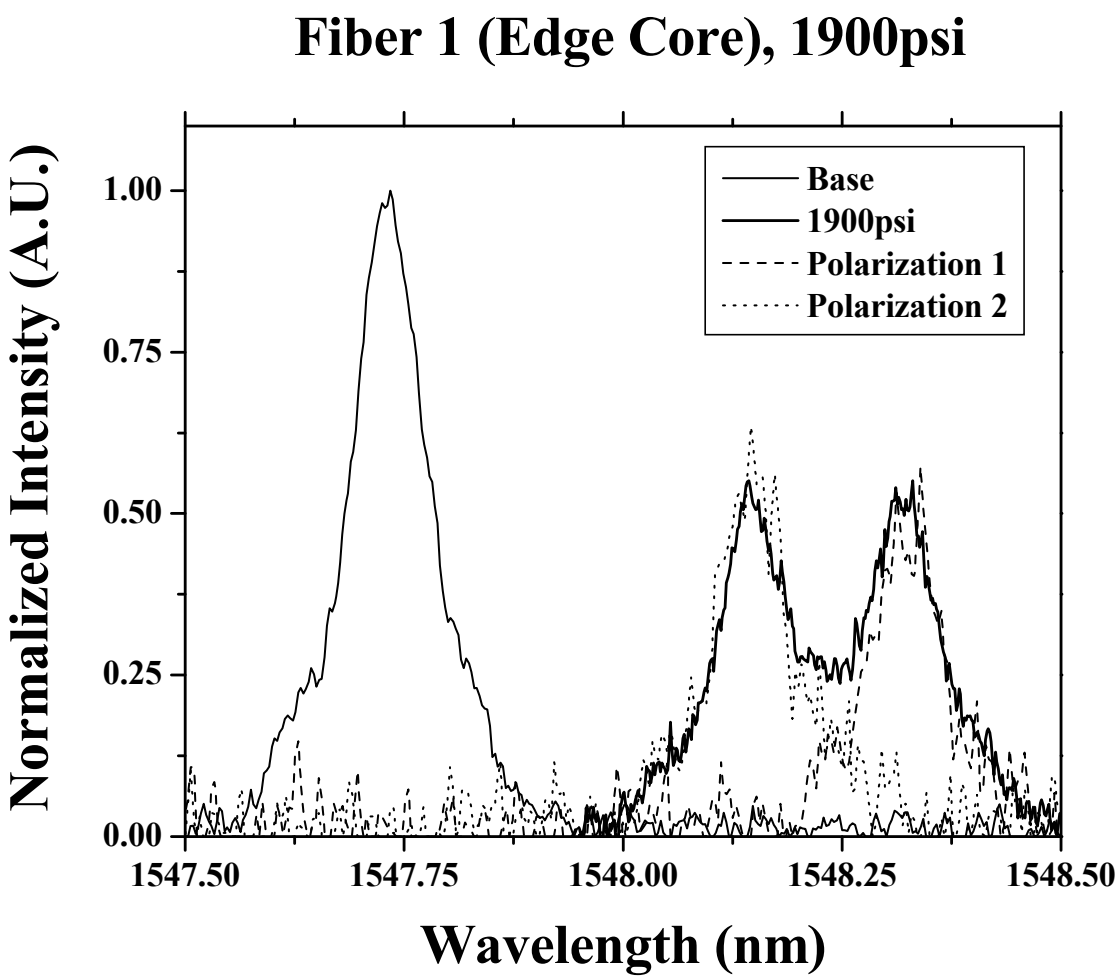

Figure 23: Peak splitting of Fiber 1 at 1900psi

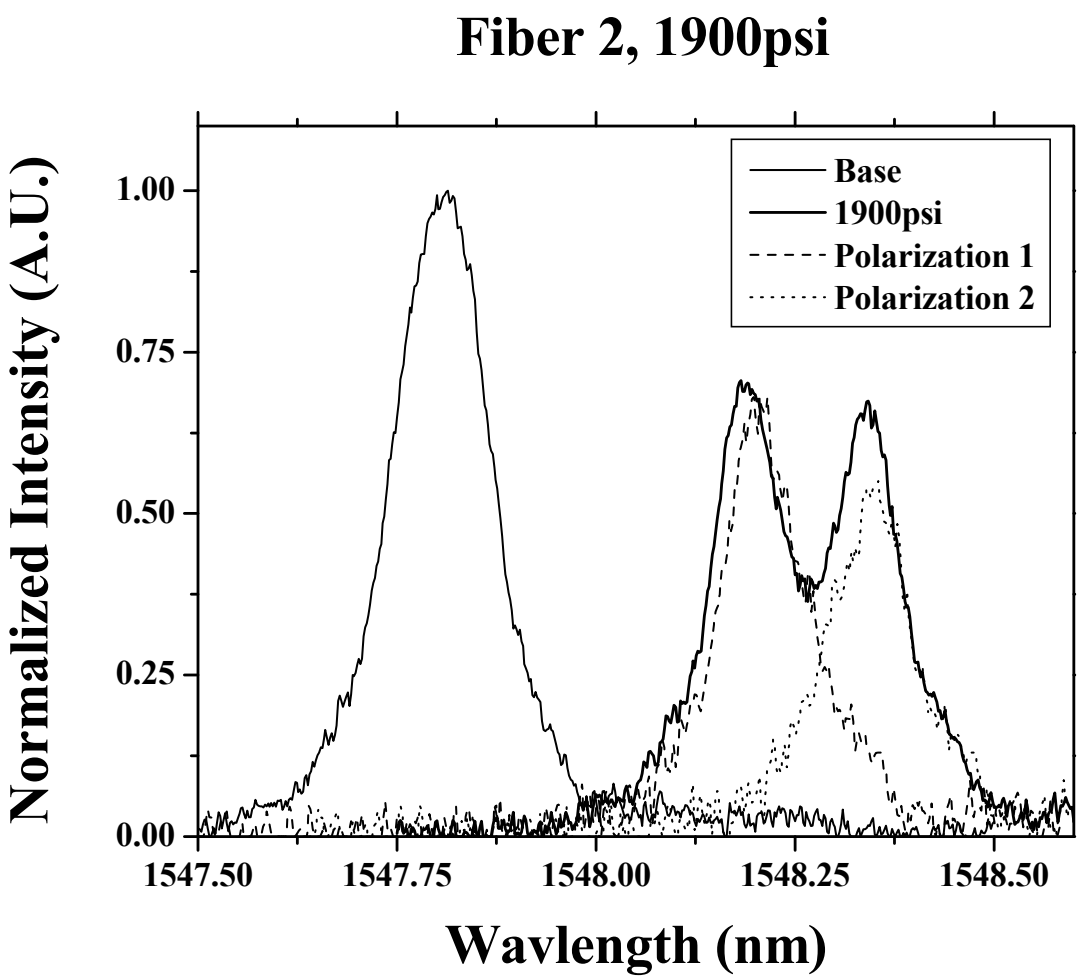

Figure 24: Peak splitting of Fiber 2 at 1900psi

For Fiber 1 a peak splitting of 0.182 nm is observed at 1900 psi, yielding a birefringence of 1.82×10^{-4}. However, this value is smaller than the value of 2.29×10^{-4} that the FEA simulations suggested. Despite the discrepancy the fiber shows a sensitivity increase of 6.5 times what has previously been reported. The overall birefringence between the two polarizations is presented in Figure 25. The two polarizations shift to higher wavelengths with a linear response to the pressure.

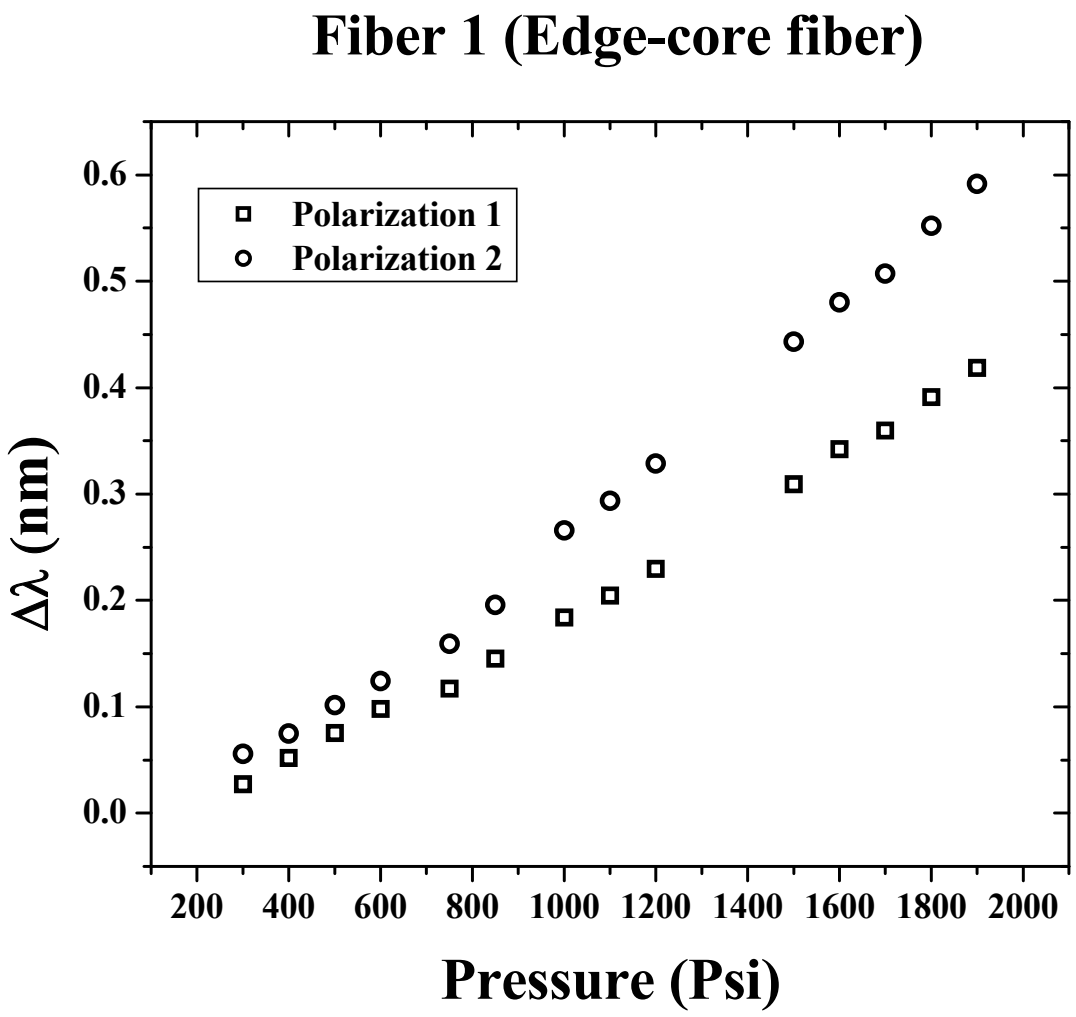

Figure 25: Polarization separation for Fiber 1 (Edge-core fiber)

For Fiber 2 the 4 μm shift of the fiber core results in a birefringence of 1.48×10^{-4}, or a 35% reduction from that of the Edge-Core fiber. The separation between the two polarizations is presented in Figure 26 for Fiber 2. It is unclear as to why Fiber 2 has significantly lower separations below 800 psi. The overall sensitivity of the two fibers is 0.11 pm/psi and 0.102 pm/psi for Fiber 1 and Fiber 2, respectively. These sensitivities present a significant improvement over what has previously been reported for air-hole fiber pressure sensors.

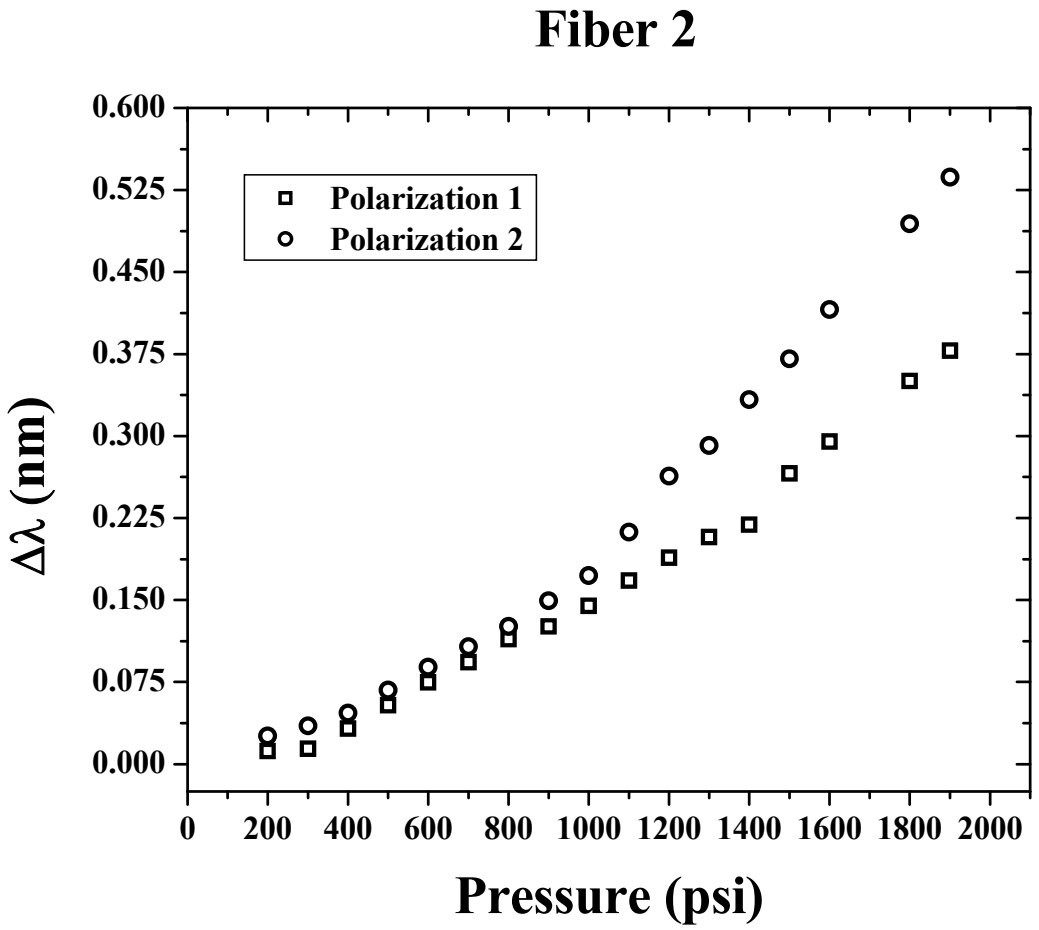

Figure 26: Polarization separation for Fiber 2

In order to verify the effect the air-hole size on the fiber's sensitivity to an applied pressure a two-hole fiber with an outer diameter of 220 μm and air-hole diameter of 77 μm was chosen. The air-holes would be increased via etching in order to observe the sensitivity change.

The gratings in the 77 μm air hole fiber were written in the same manner as mentioned previously. The same experiment that was performed with the Fiber 1 and Fiber 2 was performed for 77 μm fiber in order to obtain a baseline for sensitivity enhancement.

The air holes of the fiber were etched using a buffered oxide enchant (BOE) solution consisting of hydrofluoric acid (HF) and ammonium fluoride (NH_4F). The air holes were etched by first epoxying the fiber into the end of a syringe and then plunging the BOE solution repeatedly through the air-holes for a time of 4 minutes. After the etching process the fiber was then rinsed in de-ionized water for a time of 4 minutes in the same manner. The pressure test was again performed on the etched fiber. This procedure of etching and pressure testing was performed several more times. The results of etching the air holes on the birefringence trend versus increasing pressure and the gratings sensitivity to the applied pressure are presented in Figure 27.

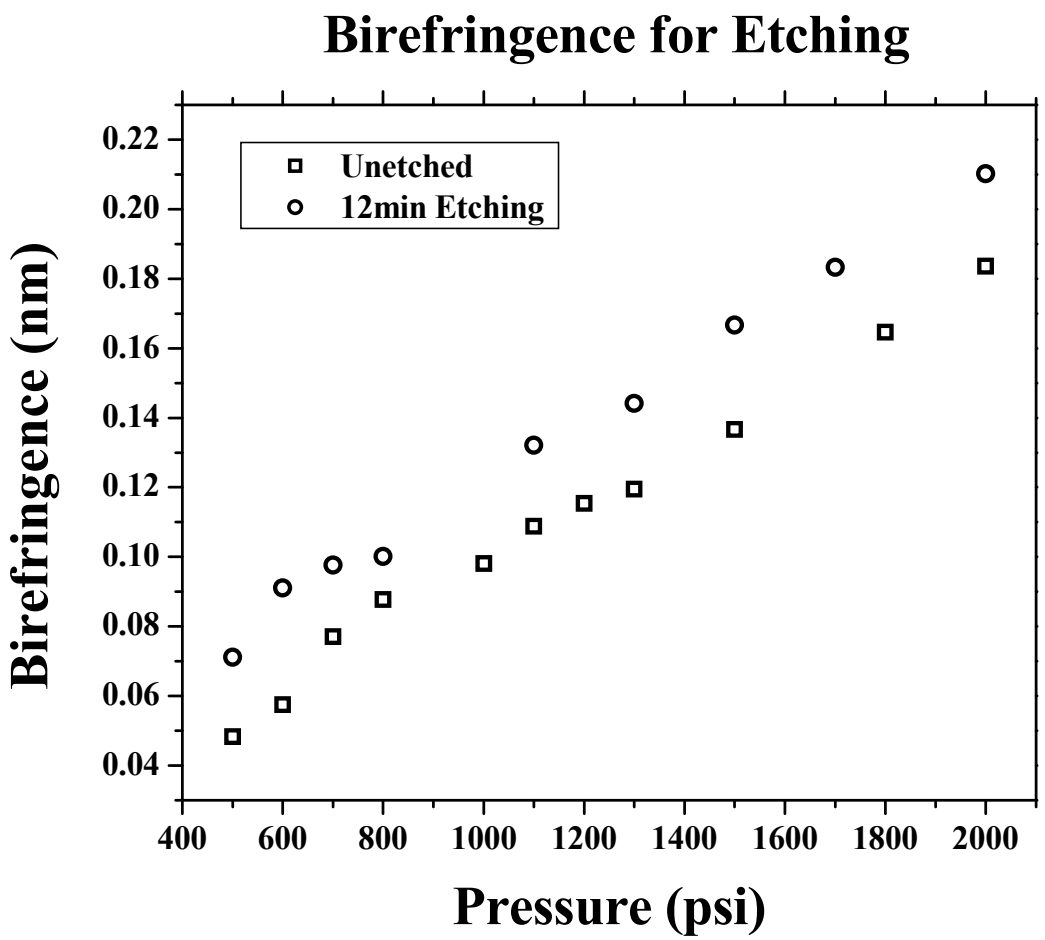

Figure 27: Birefringence of etching of fiber for unetched and 12min etching

Under both unetched and 12 minutes of etching the fiber experiences a linear trend in the birefringence with an increasing pressure. The unetched fiber possessed air-holes and an inner bridge spacing of 77 and 21 μm, respectively. After 12 minutes of etching, the air holes and bridge spacing were 81.1 and 16.9 μm, respectively. The base sensitivity of the fiber is 0.0917 pm/psi and 0.1051 pm/psi for the unetched and 12 minutes of etching, respectively. The overall sensitivity for the different etch times is presented in Figure 42. The insets in Figure 28 are for the air-hole diameter and the bridge spacing between the air-holes (in parenthesis). By decreasing the bridge spacing between the air-holes by 4.1 μm a 14.61% increase in the pressure sensitivity was obtained.

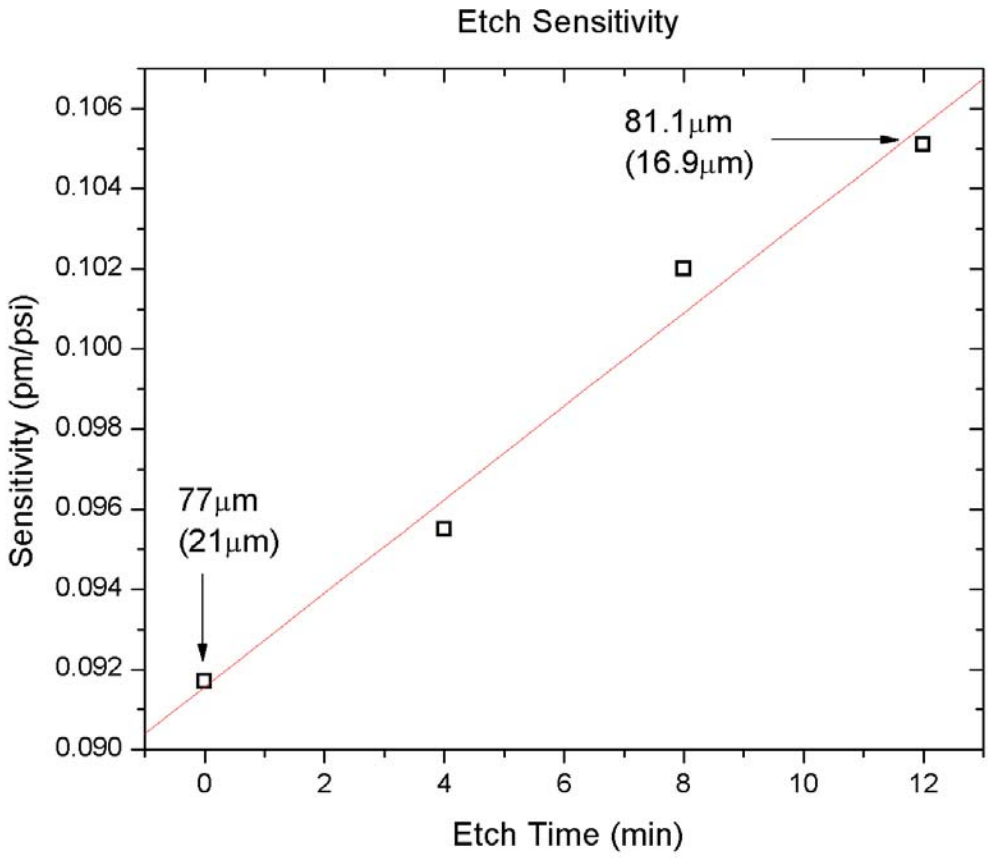

Figure 28: Sensitivity change of fiber vs. etch time

3.3 HIGH TEMPERATURE TESTING OF SMF-28 FBG WRITTEN VIA ULTRAFAST LASER

The use of fiber Bragg gratings (FBGs) as temperature sensors has been well documented over the years. The operating principle behind the temperature response of the FBG is due to the thermal expansion of the silica and the temperature dependency on the effective index of the fiber. The fractional wavelength shift due to temperature is given by

$$\frac{\Delta\lambda_B}{\lambda} = \left(\alpha + \frac{1}{n}\frac{\partial n}{\partial T} \right) \Delta T \quad . \tag{3.3}$$

Where the coefficient of the thermal expansion of silica (α) is approximately 0.55×10^{-6} and the temperature dependency on the index of refraction ($\frac{1}{n}\frac{\partial n}{\partial T}$) is approximately 8.6×10^{-6} and ΔT is the temperature change. The change in the index of refraction accounts for roughly 85% of the temperature dependency of the FBG with the typical sensitivity of the grating being 13.7 pm/C.

While FBGs have been shown to be ideal temperature sensors they have been limited to temperatures below 300C. The limitation has been because a FBG written with the standard UV phase mask technique in gemanasilicate fiber are unstable at higher temperatures. In order to overcome this limitation an ultrafast laser writing process should be used to inscribe the gratings.

The FBG used for this experiment was written using an ultrafast laser and had a spectral width of approximately 1nm. The fiber was fed through into a high temperature furnace. During the temperature experiment nitrogen gas at room pressure was used to ensure that the jacket on the fiber would not catch fire. The length of fiber with the FBG was fusion spliced to a circulator that was connected to an ASE broadband source. The spectral response of the grating

was observed using an optical spectrum analyzer (OSA). The temperature was ramped from room temperature to 700C.

The response of the grating can be seen in Figure 29, with the spectral shift presented as an insert. The temperature response of the grating is 11.43 pm/C. This is slightly lower than the sensitivity of 13.7 pm/C that has been reported in the literature. However, the response of the grating remains linear over the entire range of the experiment.

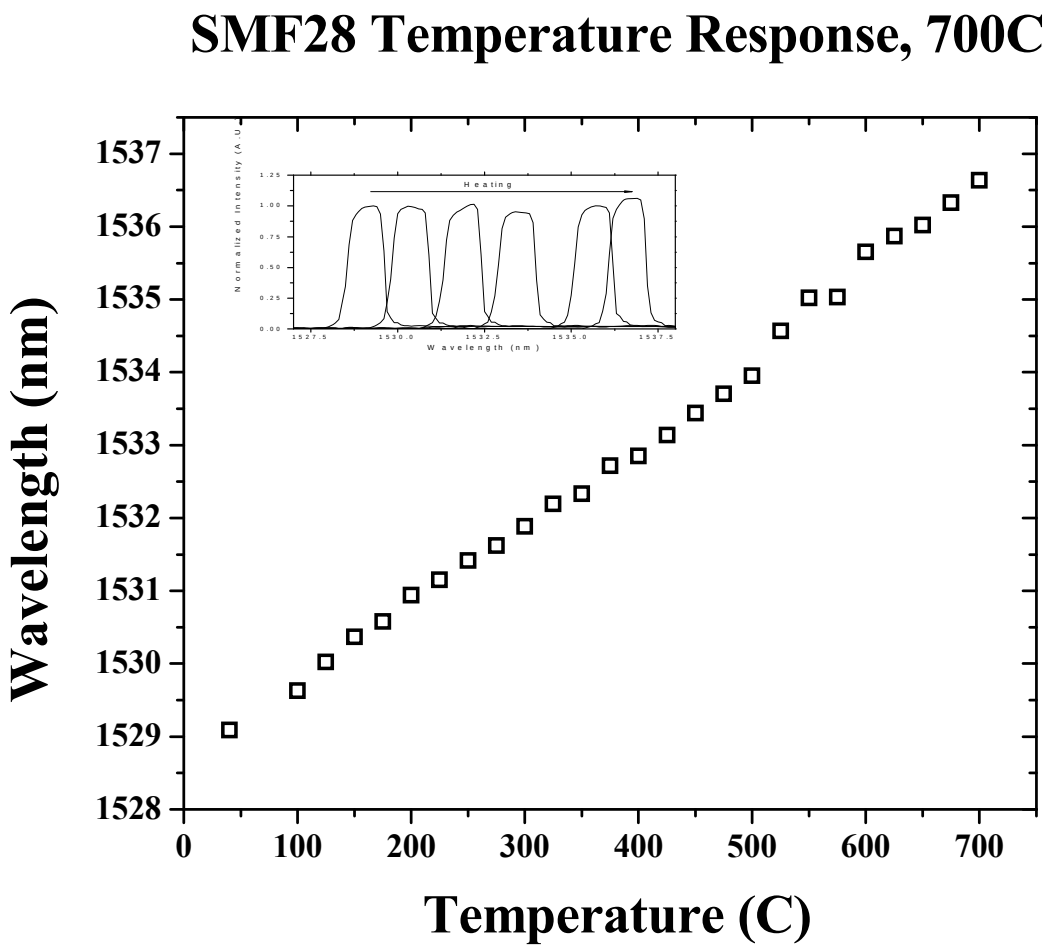

Figure 29: Temperature response of SMF28 up to 700C (insert, spectral shift of grating)

The intensity change of the grating is presented in Figure 30. The intensity of the resonant peak was normalized with respect to the spectrum taken at room temperature. With the applied temperature there is a slight change in the overall intensity of the spectrum, varying ±5%.

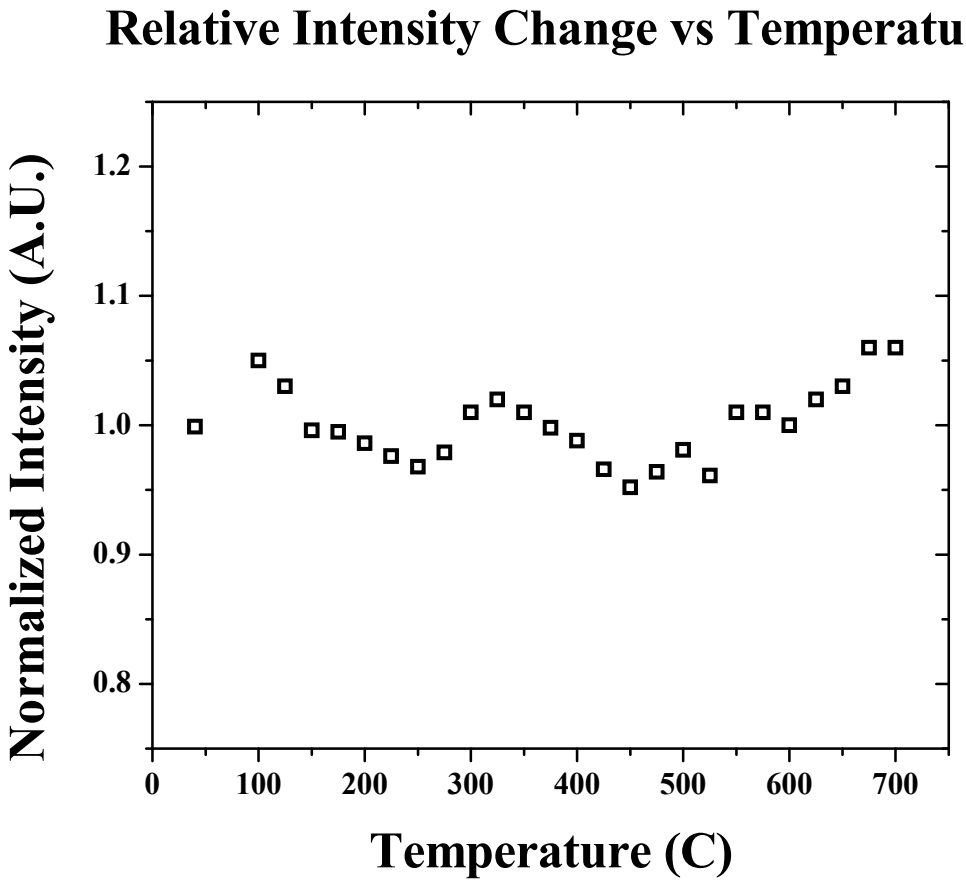

Figure 30: Relative intensity shift of grating over temperature

The grating remained heated at 700C for two hours in order to observe temperature stability and any hysteresis during cooling. After two hours the spectrum's intensity had returned to approximately the intensity at room temperature before heating with a slight decrease in the center wavelength. When cooled back to 40C the spectrum maintained the intensity before heating and exhibited no noticeable hysteresis in the spectrum. These results are plotted in Figure 31.

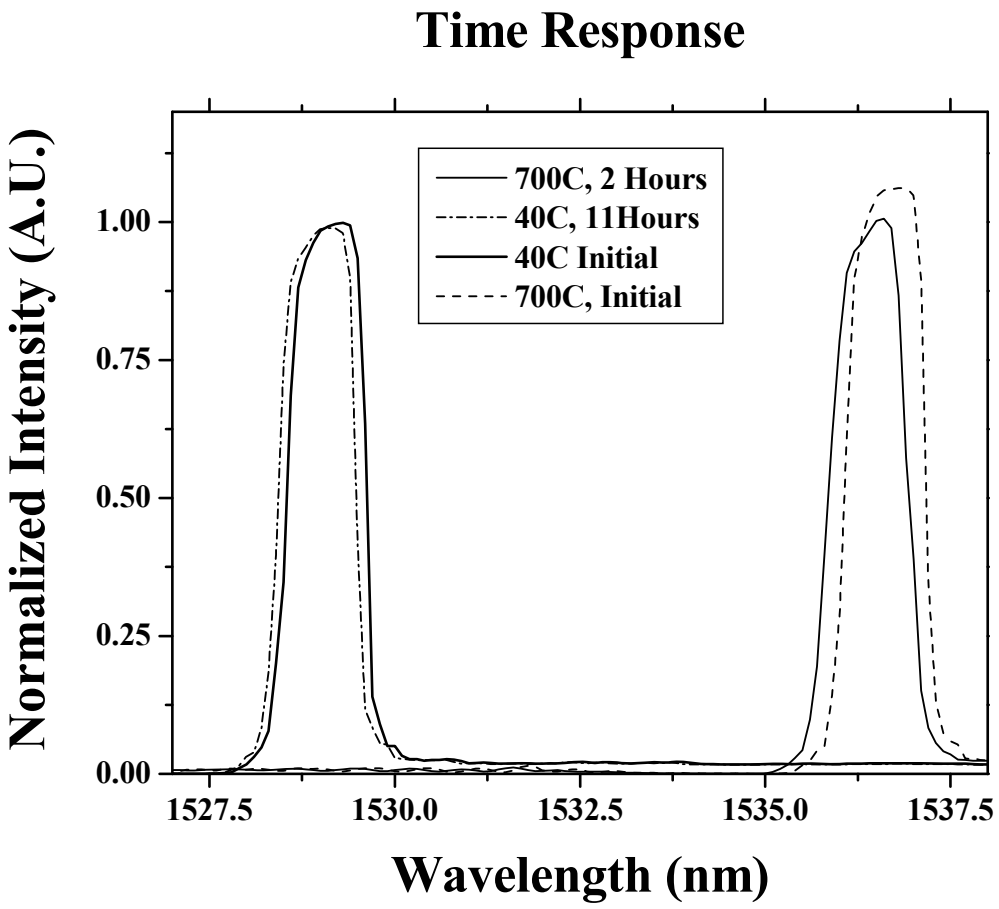

Figure 31: Grating response after 120min at 700C

The experiment was again performed in the same manner as previously mentioned with the temperature being ramped up to a maximum of 1050C in order to monitor the operation near the highest possible point for a silica fiber (1140C) with a grating. The spectral response of the grating can be seen in Figure 32 with the spectral shift presented as an insert. As with the previous temperature run the grating experiences a linear shift with increasing temperature and has a sensitivity of 12.16 pm/C.

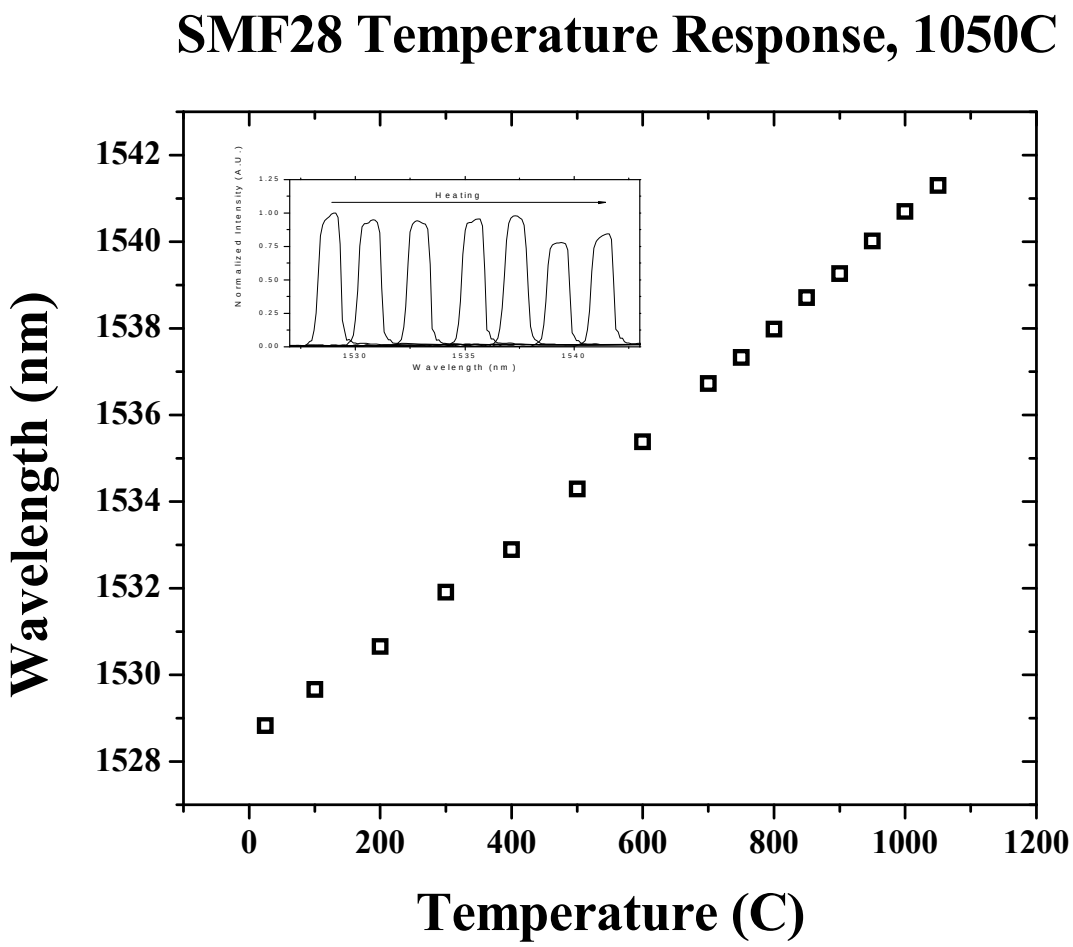

Figure 32: SMF28 temperature response up to 1050C (insert, spectral shift)

The intensity of the spectrum over the temperature range is presented in Figure 33. As with the previous temperature test the intensity varies approximately ±5% up to 700C. At temperatures higher than 700C the intensity of the grating reduces to approximately 80% of the initial intensity at 23C.

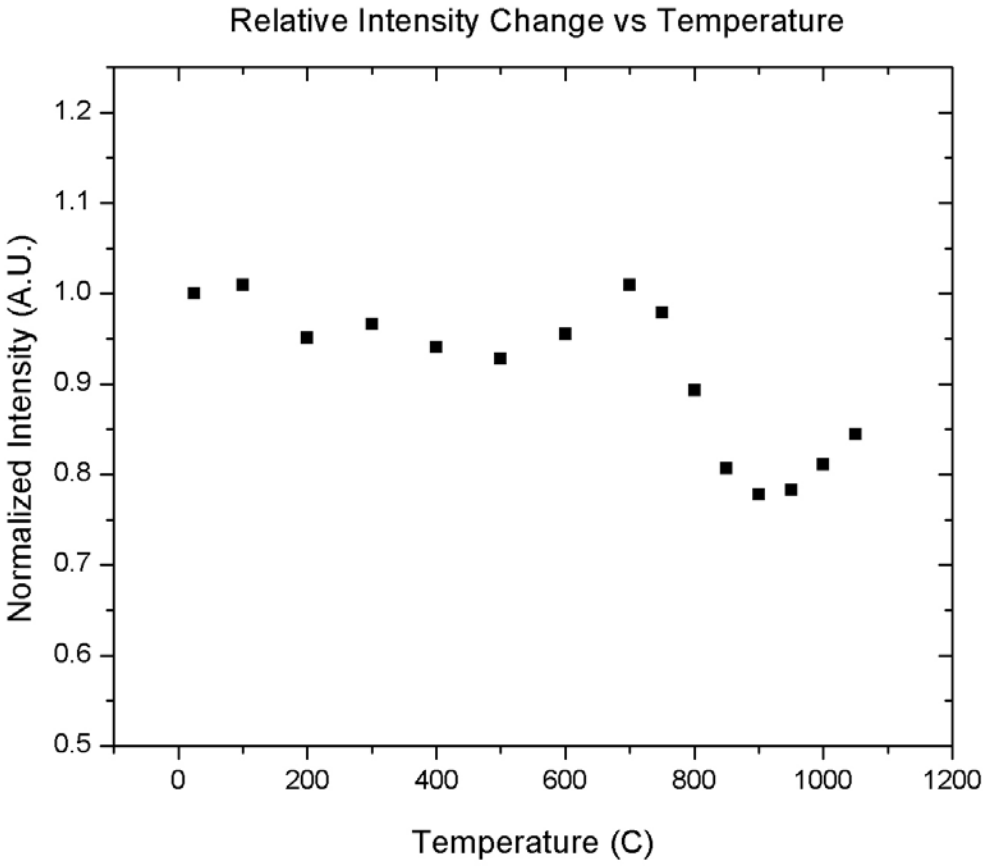

Figure 33: Relative intensity shift of grating over temperature, up to 1050C

The time response again shows that the FBG experiences little drift when held at 1050C for two hours. Over the time span little change occurs in the overall intensity of the spectrum and when cooled back to 23C the grating returns to the original intensity. The return to the base intensity is promising as it implies the decrease in intensity over 700C was not because the grating was damaged. The time results for 1050C are presented in Figure 34.

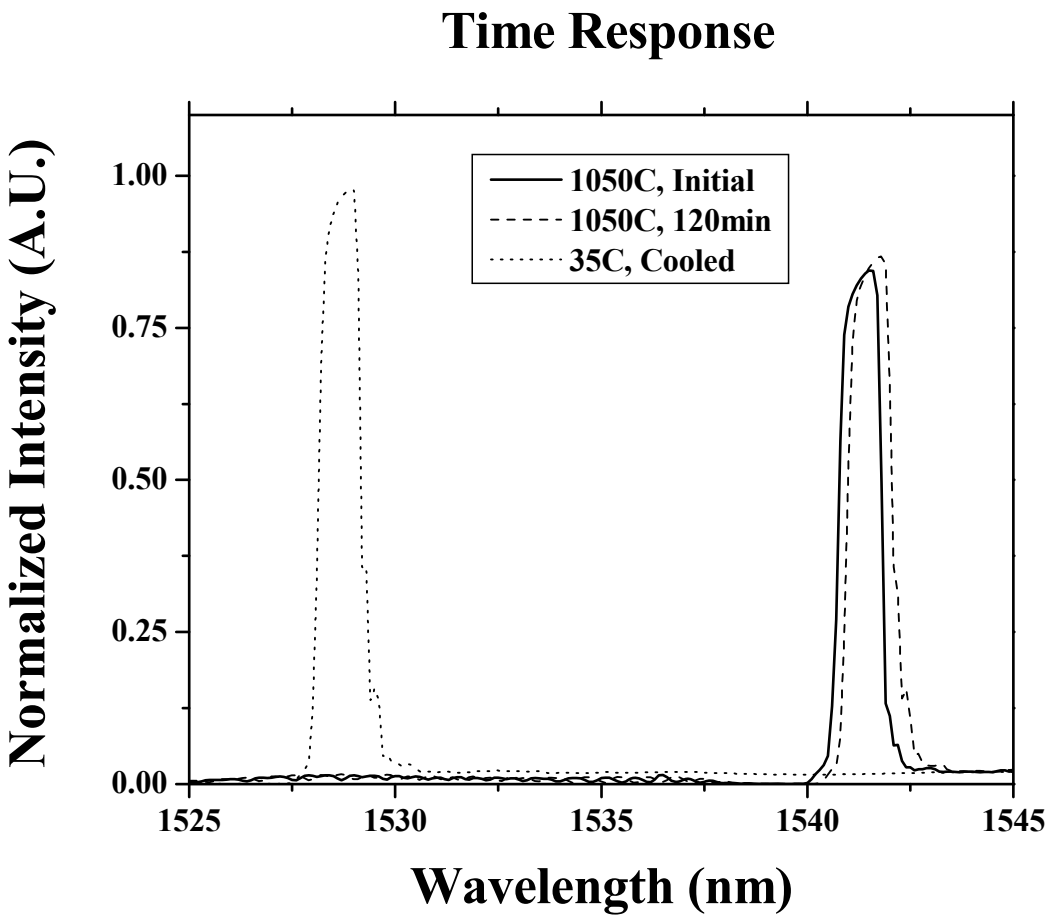

Figure 34: Grating response after 120min at 1050C

3.4 HIGH-TEMPERATURE HYDOSTATIC PRESSURE TESTING OF TWO-HOLE FBG

There has been great interest in optical fiber sensors for use as pressure sensors in harsh environments. However, standard FBGs written via the traditional UV phase mask technique have been limited in operation above 300C due to poor stability of the grating. In order to overcome this limitation it is necessary to write a grating via ultrafast laser inscription. This method creating the gratings is thought to be material compaction from a multi-photon absorption/ionization process. This method allows for higher operating temperatures. FBGs were written in two-hole fiber in the same manner as with the SMF28 grating presented earlier. The fiber referred to as Fiber 1 was used for this experiment due to the confirmation of this particular cross-section having the highest sensitivity to the applied pressure.

The fiber with the grating was spliced to a length of SMF28 and then fed through a length of stainless steel tubing using ceramic ferrules. The monitoring setup was the same as mentioned for the room temperature hydrostatic pressure test. The stainless steel tube was then inserted into a tube furnace with a thermocouple attached to the section containing the grating. A schematic of this setup can by seen in Figure 35 with the fiber cross section as an insert.

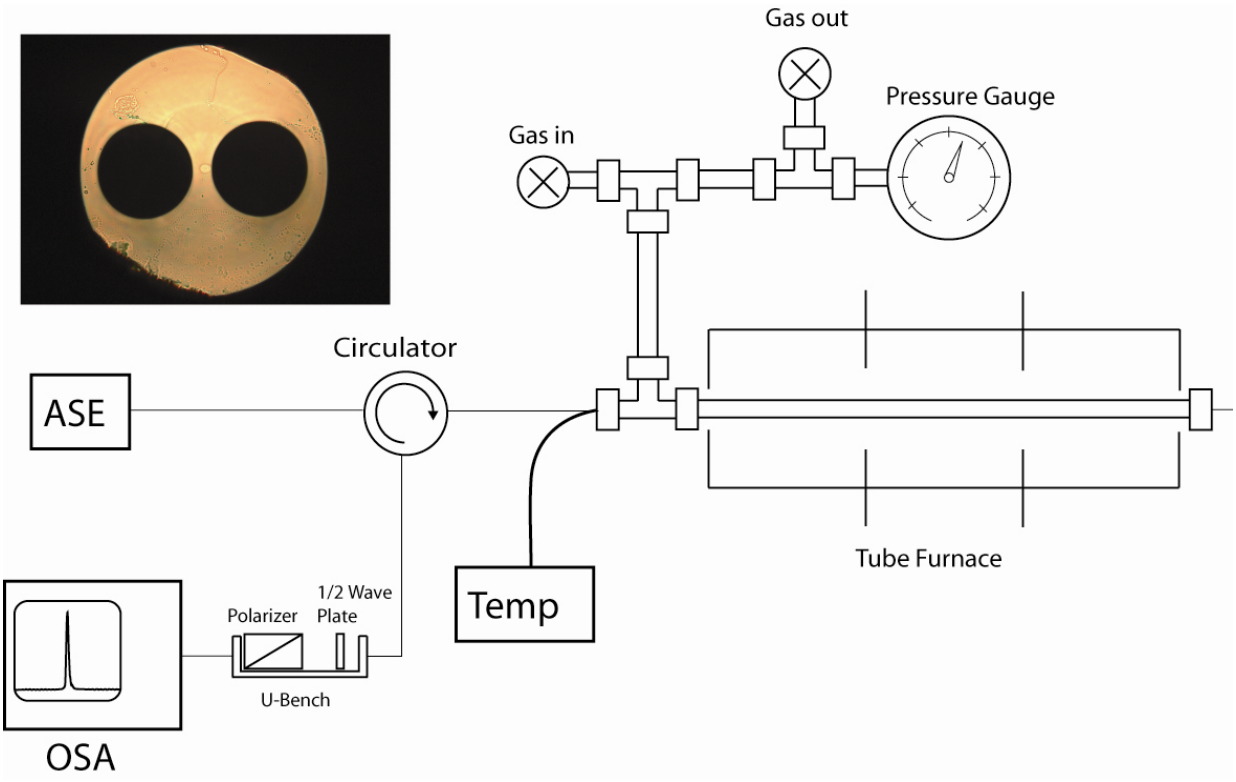

Figure 35: Experimental setup for high pressure-temperature test (insert fiber cross section)

The temperature response of the grating for heating and cooling is presented in Figure 36 with the spectral shifts of the grating presented as an insert. The grating experiences a linear shift with the applied temperature up to 858C. When cooled back to room temperature (23C) no visible hysteresis is present in the response of the grating. The grating experiences a temperature sensitivity of 14.9 pm/C.

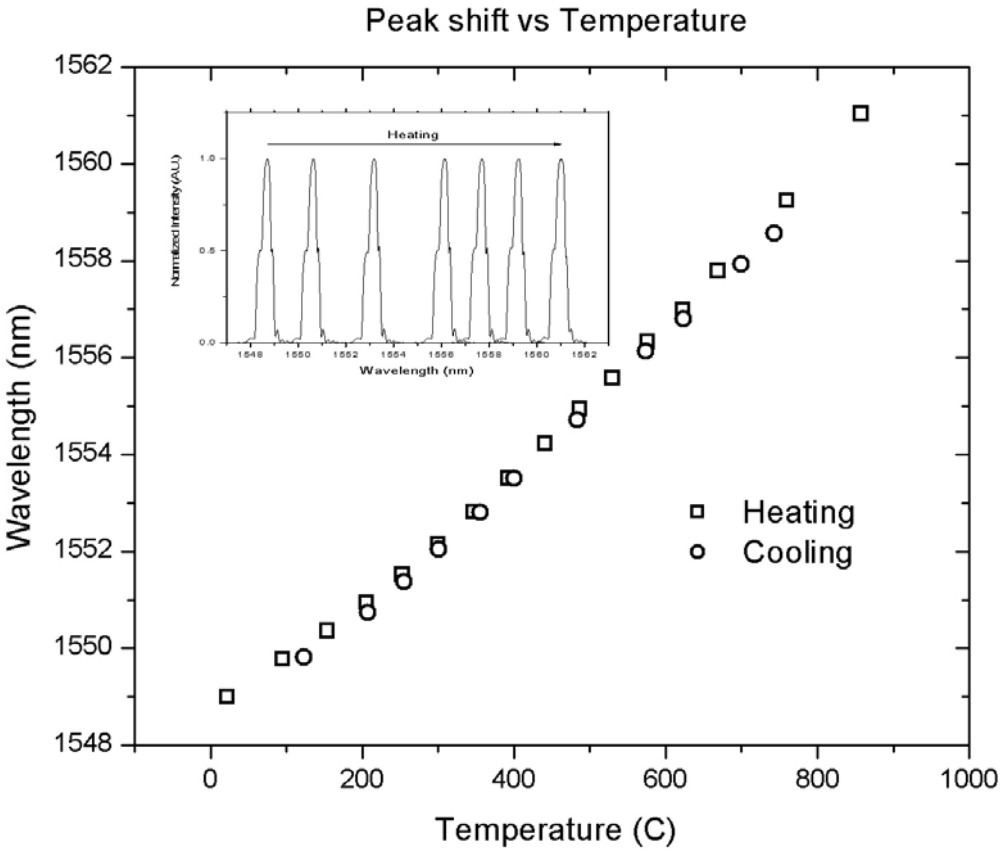

Figure 36: Temperature response of Fiber 1 to 858C and ramped down (insert, spectral shift of grating)

After the baseline temperature tests were performed it was necessary to determine the baseline pressure sensitivity of the grating. The stainless steel tubing was pressurized using nitrogen gas with a pressure range of 12 psi up to 2000 psi. The upper limit of the applied pressure was limited by the nitrogen tank available. The individual polarization modes were observed using the U-bench setup that was mentioned earlier. The spectrum at 23C and 15 psi (room temperature and pressure, respectively) is presented in Figure 37. The two polarizations when added together recreate the shape of the unpolarized spectrum, confirming that we are accurately monitoring the individual polarizations. The grating initially possessed a peak splitting of 0.19 nm, which accounts for the shoulders on the edge of the spectrum, yielding a birefringence of 1.9×10^{-4} which is much larger than the intrinsic birefringence of the fiber ($<10^{-5}$).

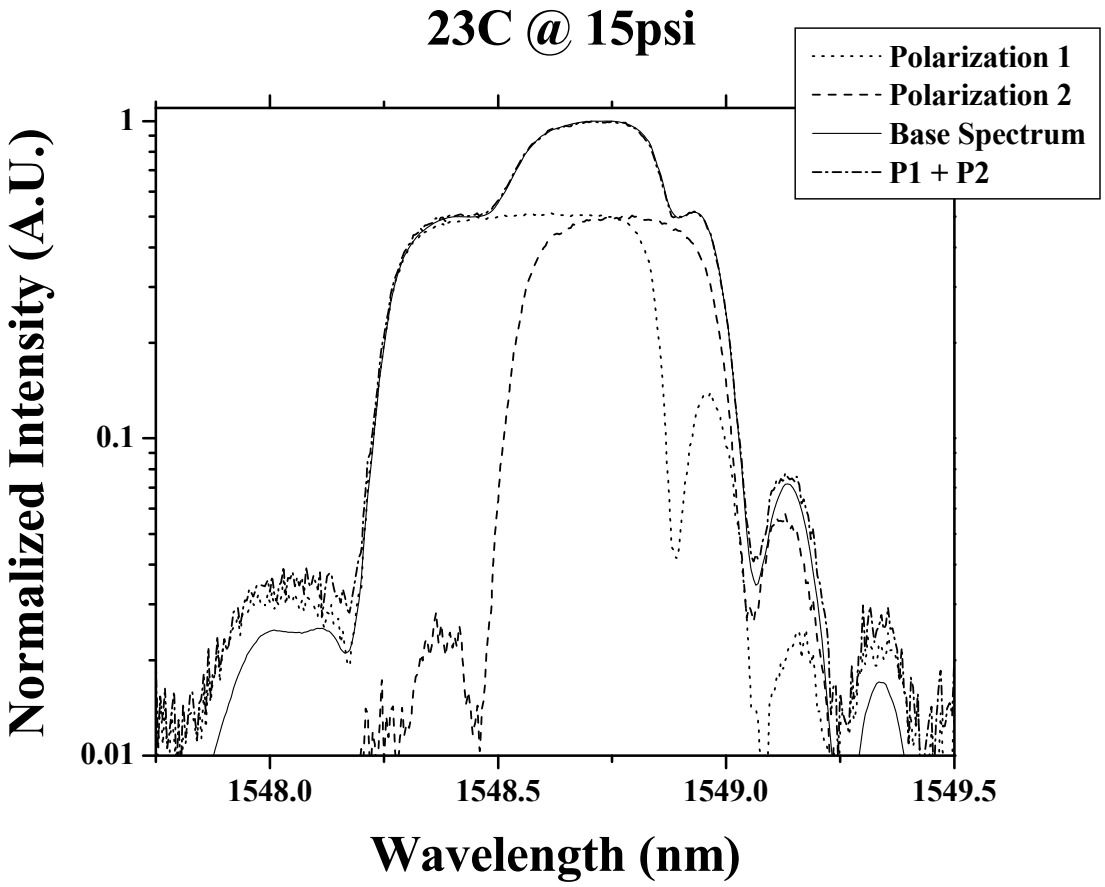

Figure 37: Base spectrum at 15psi and 23C

As the pressure was increased the splitting between the two polarizations decreased to -0.006 nm at 2000 psi. The spectrum at 23C and 2000 psi can be seen in Figure 38. The change in the shape of the spectrum is due to the pressure having an effect on one polarization more so than the other. The overall sensitivity of the grating at 23C is 0.0983 pm/psi, which is in agreement with the results for the FBG written using the UV phase mask technique.

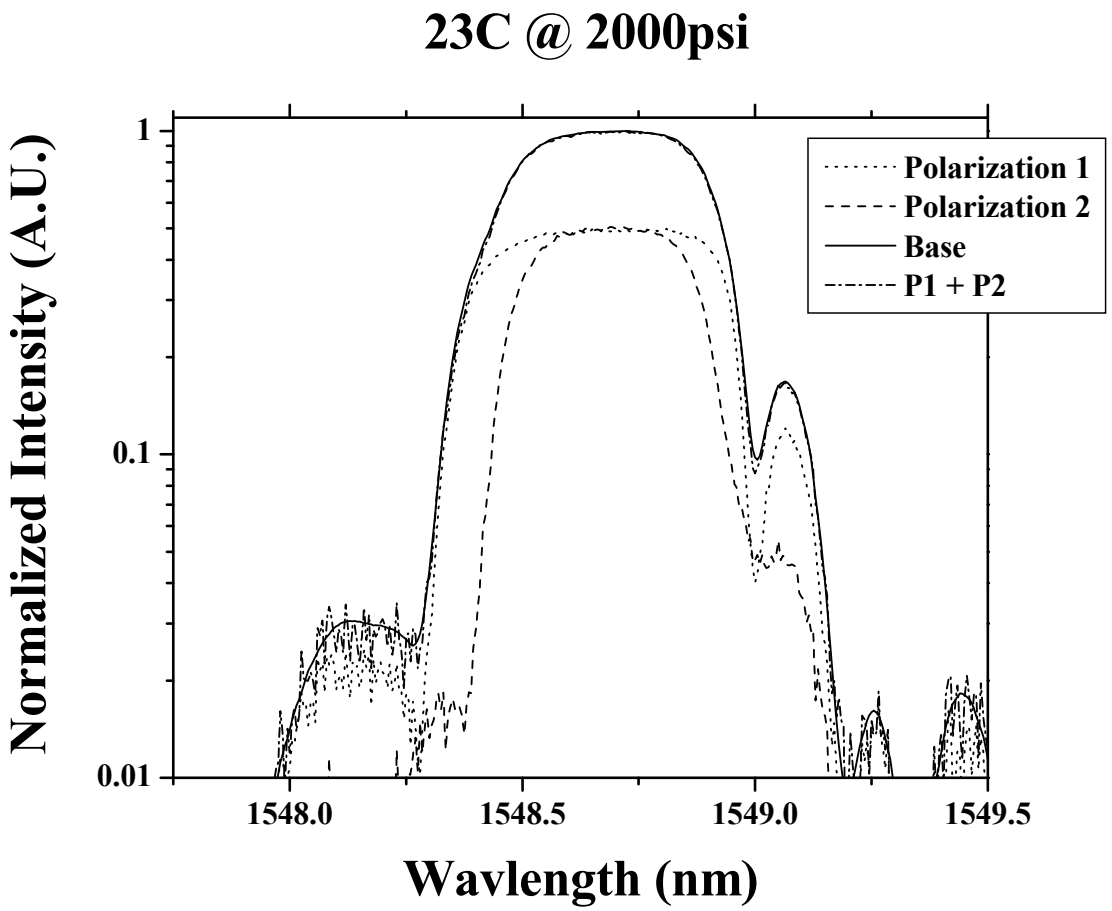

Figure 38: Spectrum for grating at 23C and 2000psi

The temperature was then ramped up from 23C to 858C. At several temperature intervals the pressure was ramped up to 2000 psi and the birefringence of the grating was again observed in the same manner as before. Figure 39 presents the spectrum at room pressure (15 psi) with an applied temperature of 858C. The overall shape of the grating is consistent with the spectral shape observed at room temperature (23C), confirming that the two orthogonal polarizations experience the same linear shift with increasing temperature.

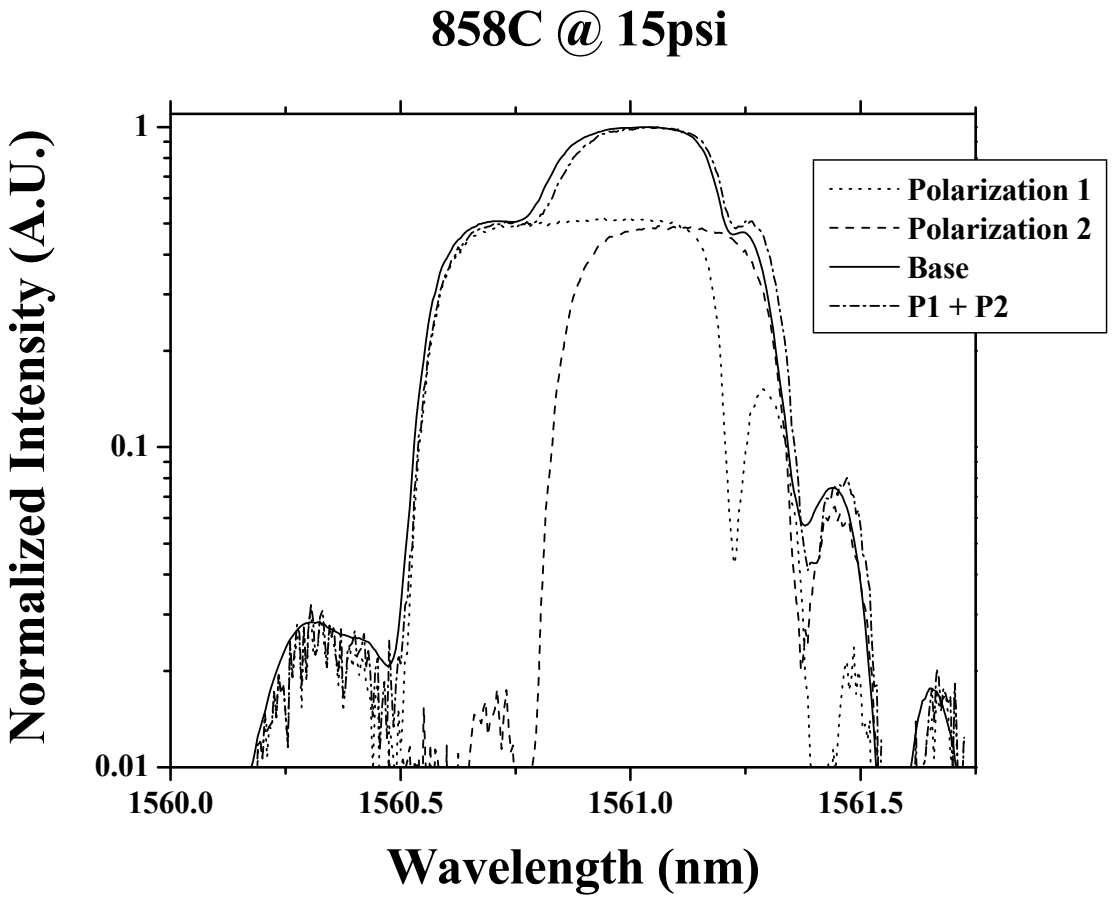

Figure 39: Base spectrum for grating at 15psi and 858C

Figure 40 presents the spectrum at 858C and 2000 psi. As with the pressure test performed at 23C, one polarization is affected more by the applied pressure than the other.

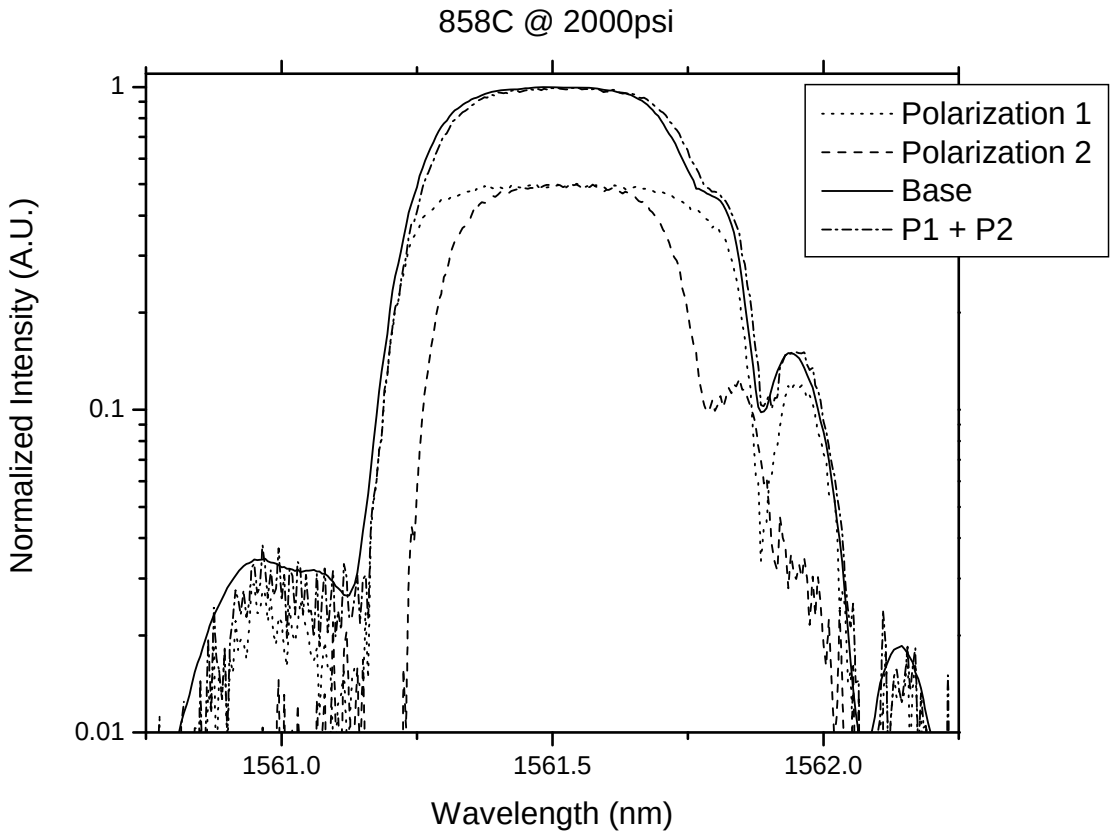

Figure 40: Spectrum taken at 858C and 2000psi

Overall the sensitivity to the applied pressure is predominately linear. However, at pressures higher than 1500 psi a nonlinear trend is observed in the birefringence. The responses of the grating at 23, 199 and 858C are presented in Figure 41. The pressure sensitivities of the grating are 0.0983, 0.1076 and 0.0993 pm/psi for 23, 199 and 858C, respectively. At the higher temperatures there is approximately a +10% difference in the pressure response of the grating from that of room temperature.

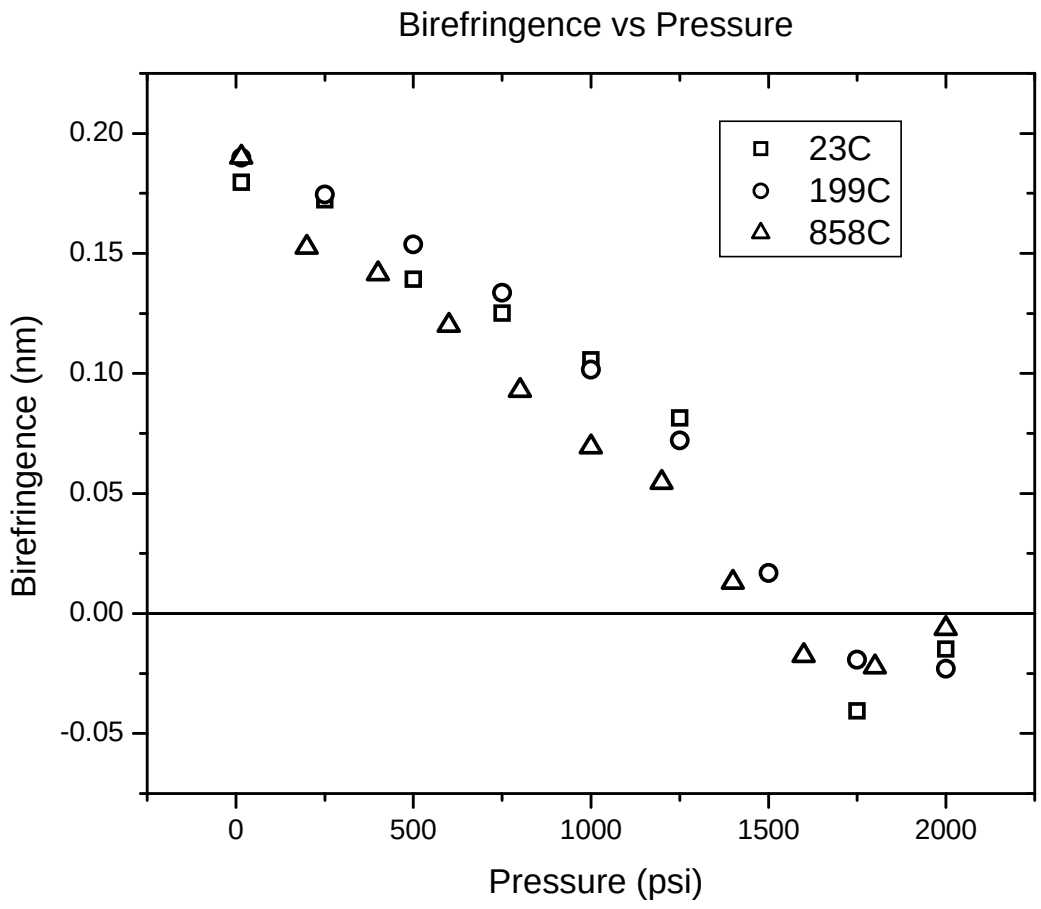

Figure 41: Pressure response of grating at 23, 199 and 858C

3.5 LIMITATIONS OF TWO-HOLE FBG AT 1000C

In order to observe the upper operation limit of the grating the temperature was ramped up to an applied temperature of 1000^{o} C. At 1000^{o} C the pressure was then ramped up to 2000 psi as with the previous tests. As the grating was heated to 1000^{o} C the shoulders of the grating disappeared and the baseline shape of the grating changed more into that of a typical grating. As the pressure was ramped up the grating's intensity increased to almost twice of the initial intensity at 1000 psi and then reduced to approximately 80% at 2000 psi. The spectrum also shifted approximately 3nm to a higher wavelength. The shape of the grating for the varying pressures at 1000^{o} C is presented in Figure 42.

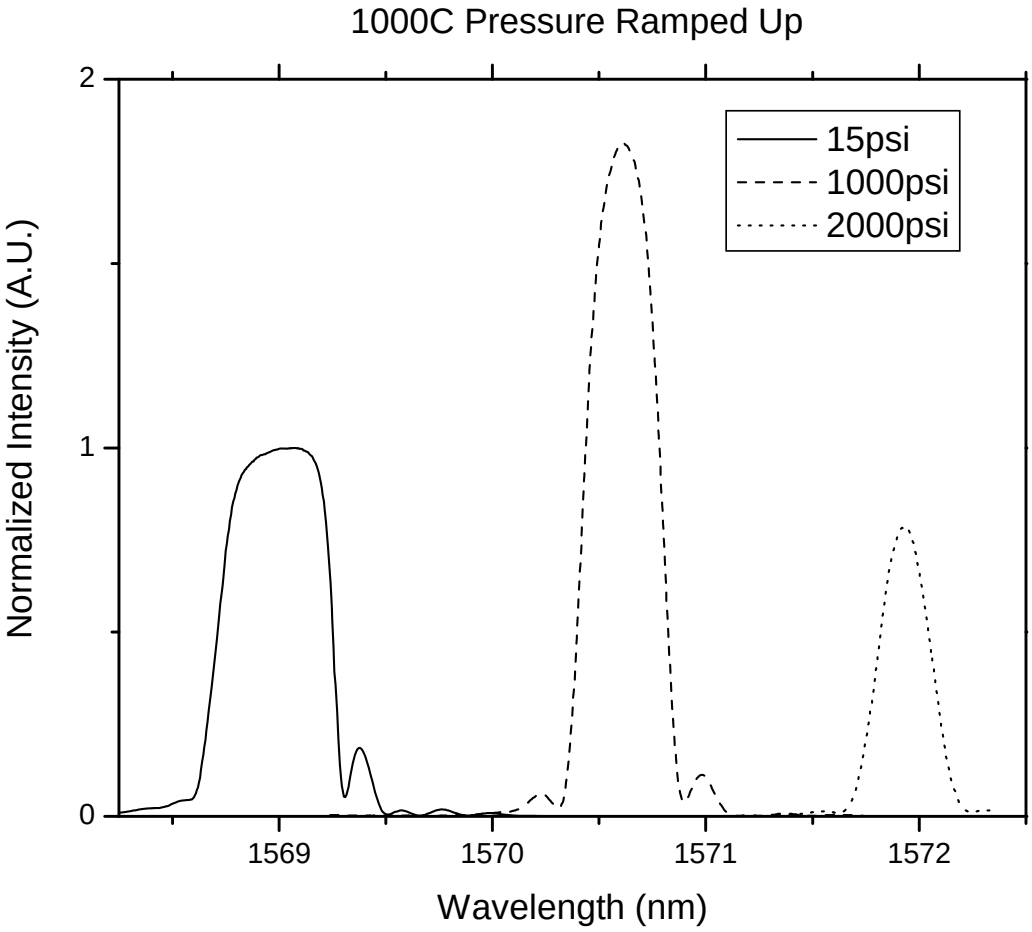

Figure 42: Spectral shape change and shift at 1000C with pressures of 15, 1000 and 2000psi

When the pressure was removed the grating's intensity returned to the base intensity as was observed with the SMF28 tests. However the overall shape of the grating was much different and the grating remained at the higher wavelength. These results are presented in Figure 43.

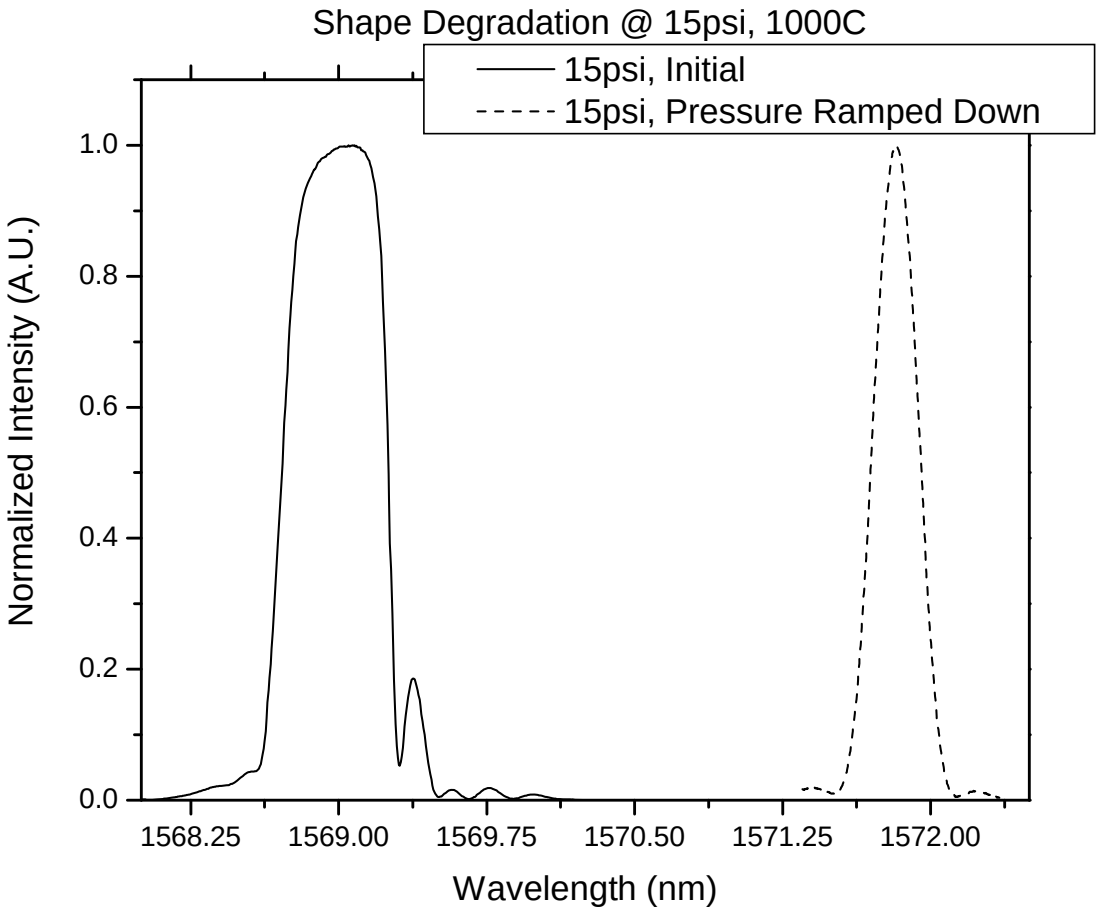

Figure 43: Spectral shape change and shift at 1000C, before pressure is applied and after pressure is removed

Despite the degradation in the spectral shape of the FBG the grating experienced a predominantly linear response to the applied pressure and is presented in Figure 44. The overall sensitivity did decrease significantly to 0.035 pm/psi which is approximately 33% of what was observed at 23 and 858C. It is believed that the degradation of the grating was due to the softening of the fiber at the higher temperature.

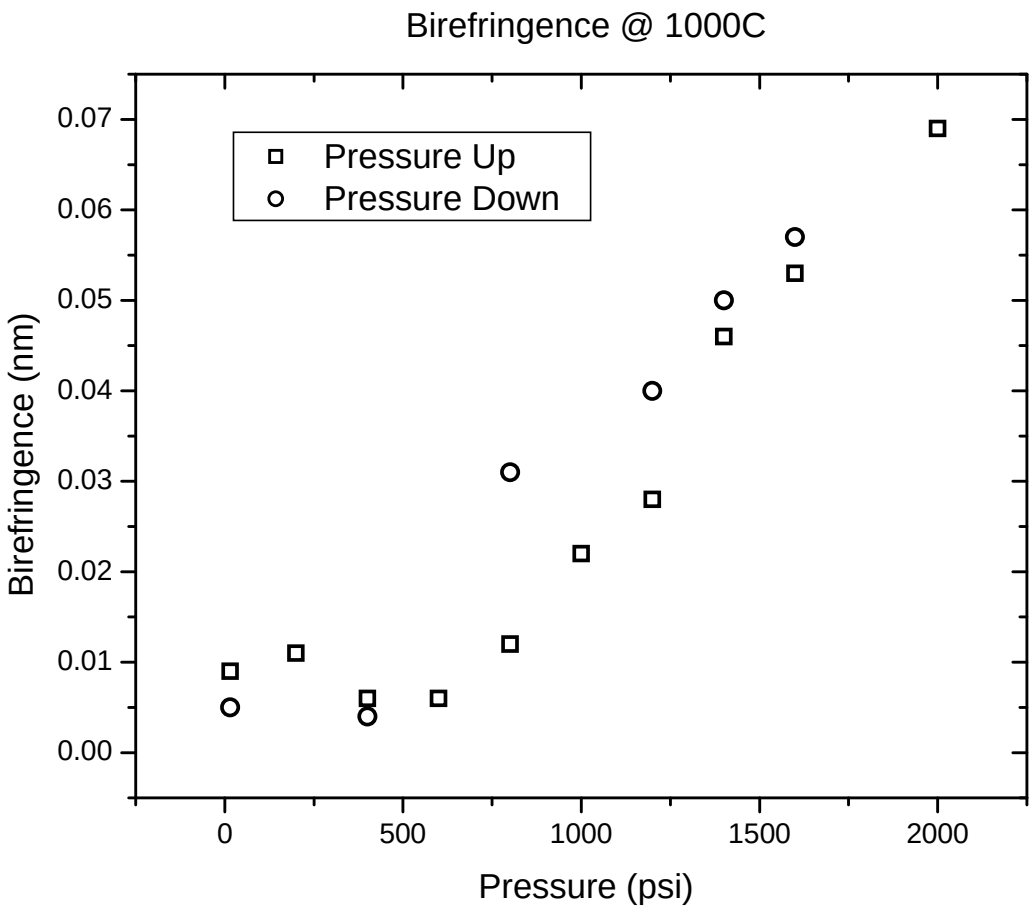

Figure 44: Pressure response of grating at 1000C for pressure ramped up to 2000psi and back down to 15psi

4.0 DESIGN OF A HIGHLY BIREFRINGENT PHOTONIC CRYSTAL FIBER FOR HYDROSTATIC PRESSURE SENSING

4.1 PREMISE

Fiber sensors based on air-hole microstructured fibers have received considerable attention recently for their versatility in tuning mechanical, thermal, and optical properties through the design of the fiber. This flexibility has enabled the fabrication of many new and exciting fibers with unique properties that are unattainable in conventional fibers. For example, in many fiber sensing applications, polarization maintaining (PM) fibers are desired because they provide a better signal-to-noise ratio and allow for simplification of the measurements. Using air-hole microstructured designs, PM fibers with birefringences in excess of 1×10^{-3} [8, 15, 17, 42, 43] can be readily manufactured, which is more than an order of magnitude than that of conventional fibers.

Given the importance of PM fibers, a number of air-hole fiber designs have been proposed and studied.

In this chapter I will present a new air hole design for increasing the induced birefringence in optical fibers with an applied hydrostatic pressure. This design will be modified and applied to a highly-birefringent photonic crystal fiber design. The operating parameters of this fiber are to be reported as well as a novel fabrication method.

4.2 NEW TWO-HOLE DESIGN

It was previously demonstrated how the structural engineering of the optical fiber can allow for the creation of new sensors. I now present simulations on the improvement over the previous work for use as a hydrostatic pressure sensor. In this case we again consider a MOF with a two-hole structure. However, instead of maintaining the circular shape of the air-holes it is necessary to create an air hole shape that resembles a tear-drop. The tear-drop shape itself has several advantages over the traditional two-hole fiber in that the shape in turn focuses more of the stress into the center of the fiber as the air-holes do not deflect any of the stress about their outer edges into the fiber cladding not containing the core.

The fiber was designed using three parameters for the shape and size of the air holes; the length, angle and radius of the hole. A diagram of the fiber shape is presented in Figure 45. The shape of the air-holes was then optimized for the highest sensitivity to the applied load. The final design of the fiber had 220 μm, 45^{o}, 30 μm and 97.5 μm for the outer diameter of the fiber, angle, radius and length of the tear-drop air hole, respectively. The fiber core was taken to be 3μm in diameter and directly touching one of the air-holes. This design resulted in a pressure sensitivity of 0.4148 pm/psi while a fiber cross-section with two round air-holes with the same bridge spacing and core size as the tear-drop fiber has a sensitivity of 0.194 pm/psi.

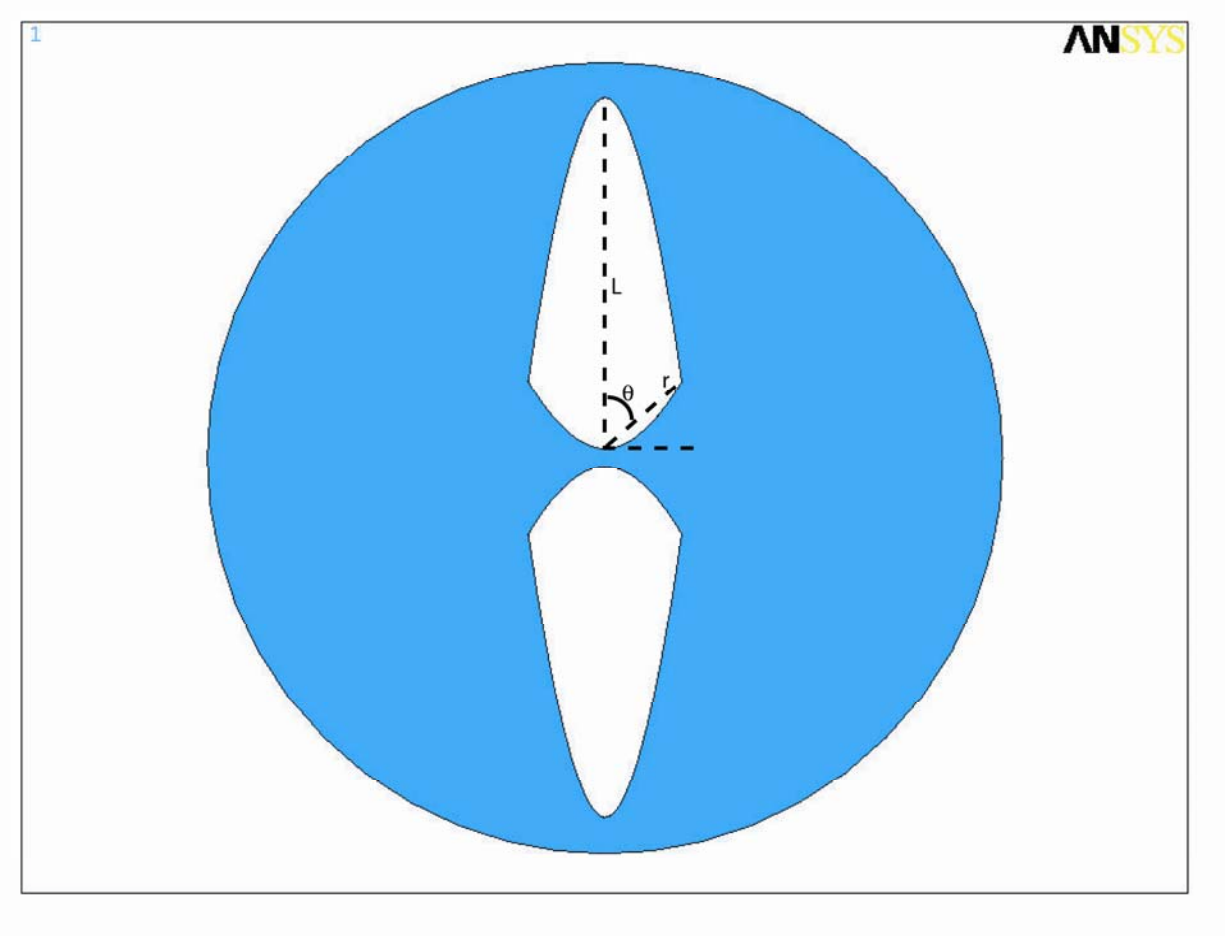

Figure 45: Schematic design of tear-drop fiber

The sensitivity of the fiber for an angle of 45^{o} with a varying radius is presented in Figure 46. For this fiber shape the radius can vary between 20 and 40 μm with little change in overall sensitivity. This is a promising result because this allows for a larger tolerance when creating the fiber perform and during the drawing process.

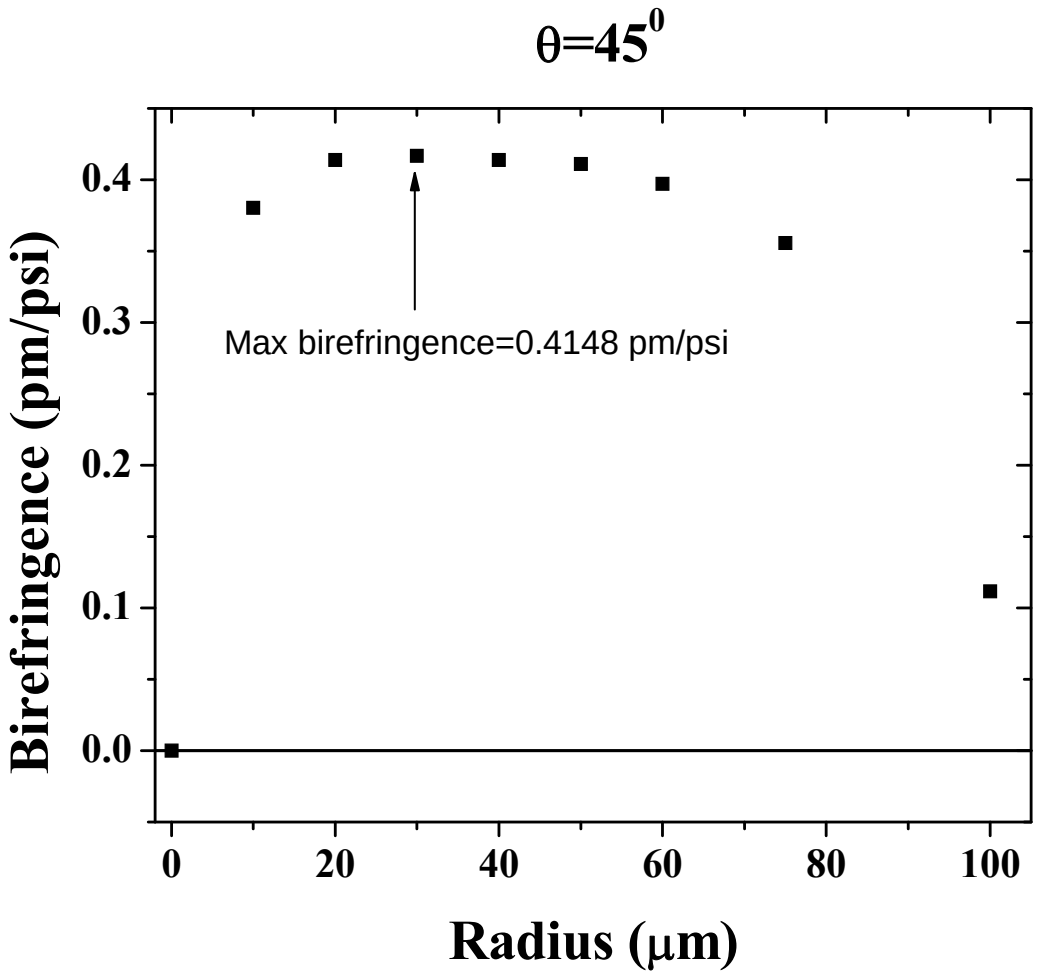

Figure 46: Sensitivity to pressure vs. radius of tear bottom

The birefringence over the cross section of the fiber with an applied pressure of 200 bar is presented in Figure 47.

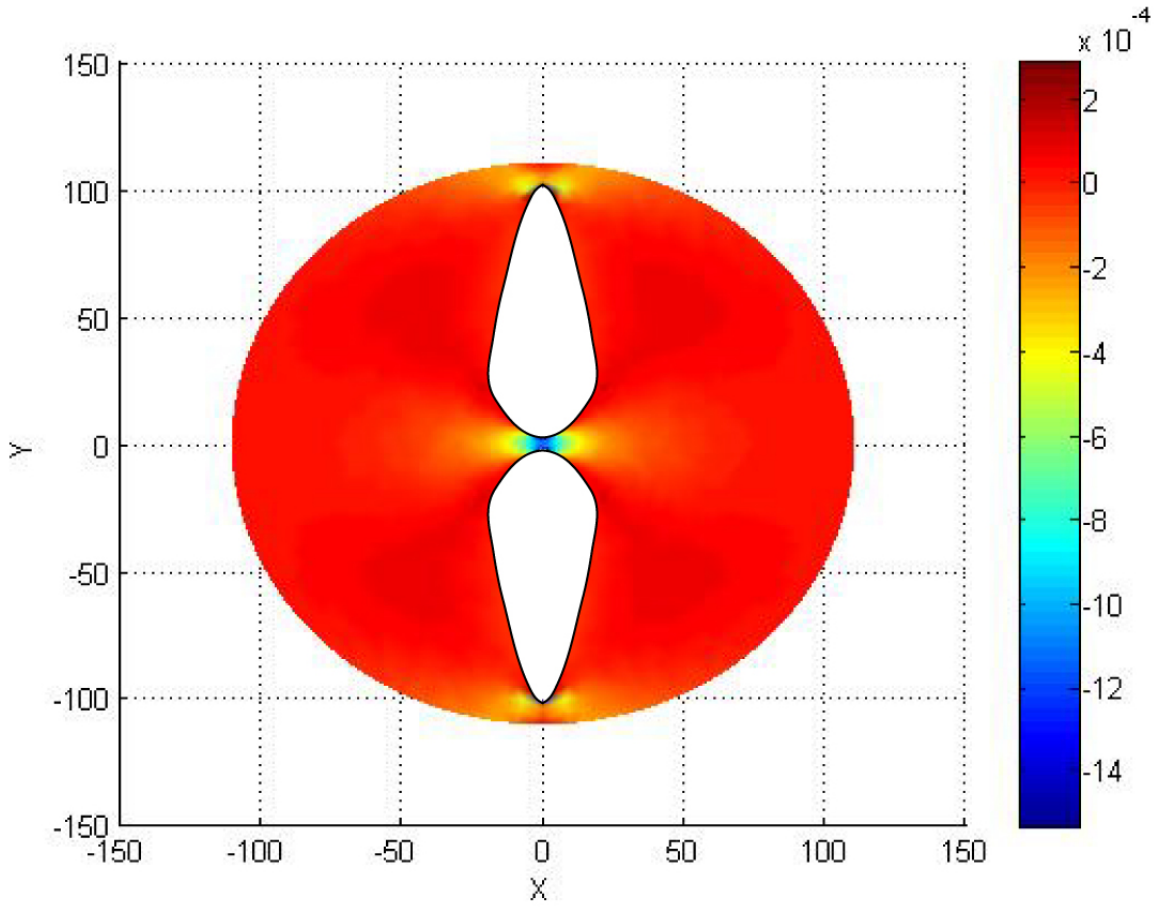

Figure 47: Birefringence in tear-drop fiber with 200 bar applied pressure

Figure 48 confirms that as the core moves further from edge of the air-hole there is a significant decrease in the observed birefringence, as was observed for the round air-hole fiber. Therefore even with a highly sensitive cross-section proper placement of the core must still be considered in order to create the highest possible pressure sensor.

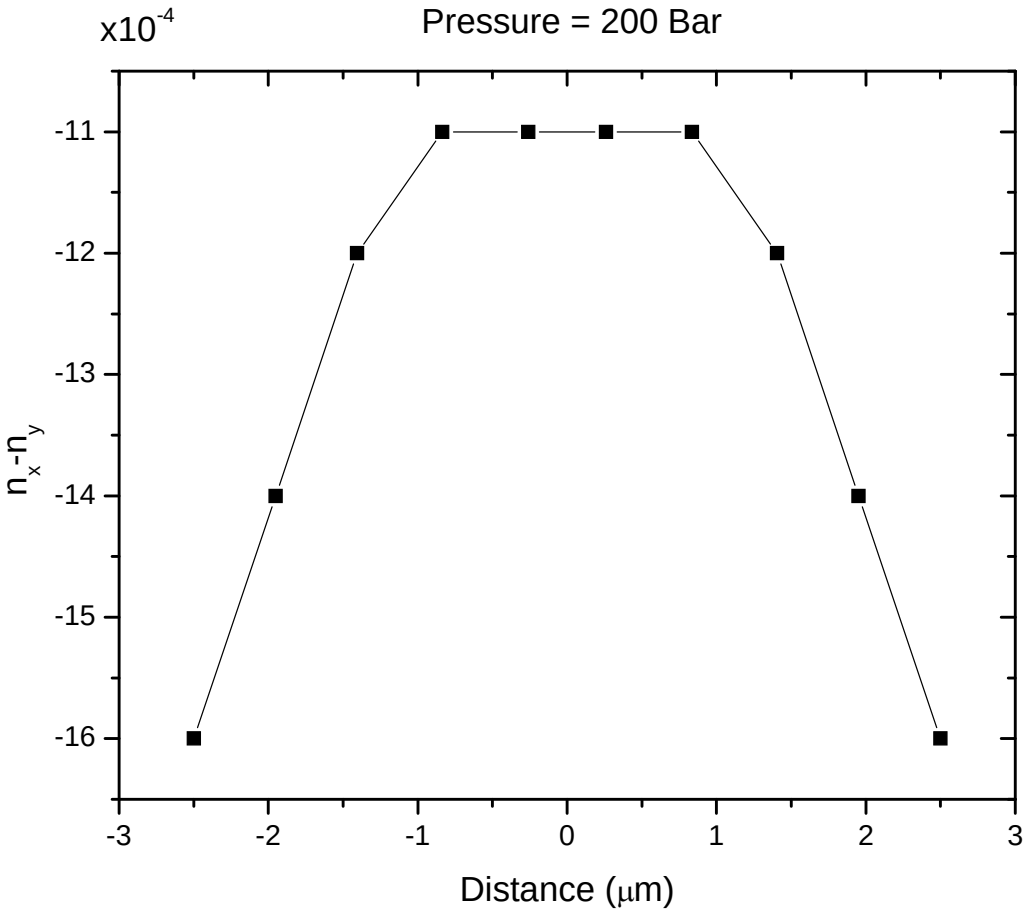

Figure 48: Birefringence between air-holes for Tear-drop fiber

While the tear-drop fiber design presents a significant increase in the pressure sensitivity there are issues concerning its fabrication. Microstructured optical fibers are fabricated by either stacking glass capillary tubes to create an air-hole matrix or via ultrasonic drilling of air holes to create a fiber perform. The overall shape of the tear-drop possesses significant problems for fabrication; therefore it is ideal to do an air-hole integration of the tear-drop by using an ultrasonic drill to drill circular air-hole. These air-holes will allow for the overall shape of the tear-drop to be maintained. The proposed cross-section and birefringence at 200 bars are presented in Figure 49.

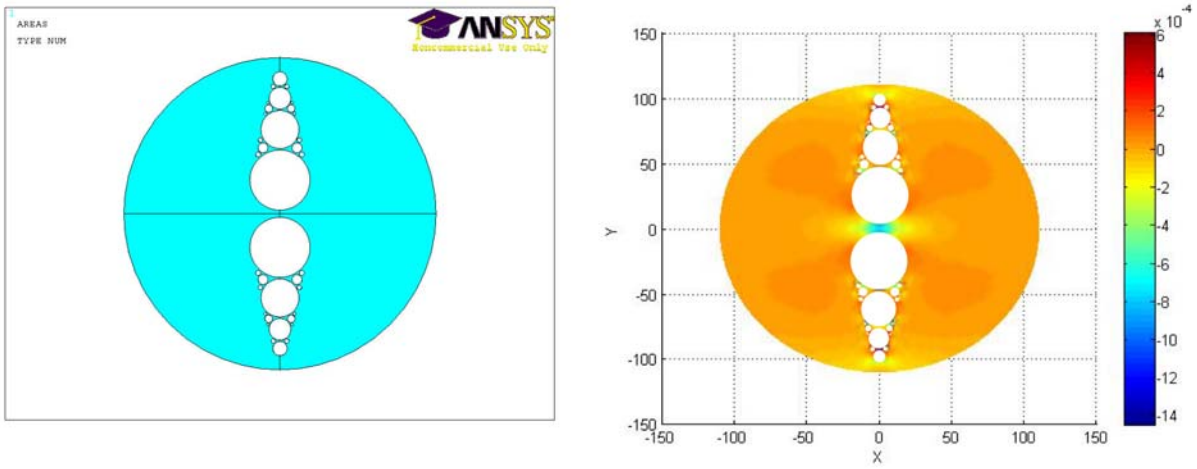

Figure 49: Tear-drop fiber design via circular air-holes (left), birefringence at 200 bars

The shape was maintained by using four larger air-holes to create the general shape and then smaller air-holes added to eliminate the majority of the material between the holes. This overall shape has a 0.275 pm/psi pressure sensitivity. While not as sensitive as the original design this still presents a significant improvement over the traditional two-hole fiber design. It is also suggested that by using the BOF etchant solution used to enlarge the air-hole of the two-hole fiber it should be possible to etch out the spacing between the air-holes to in turn create the

tear-drop shape and significantly improve the sensitivity of the fiber. Simulations were performed by increasing the diameter of the air-holes up to a maximum increase of 0.5 μm. The results are presented in Figure 50.

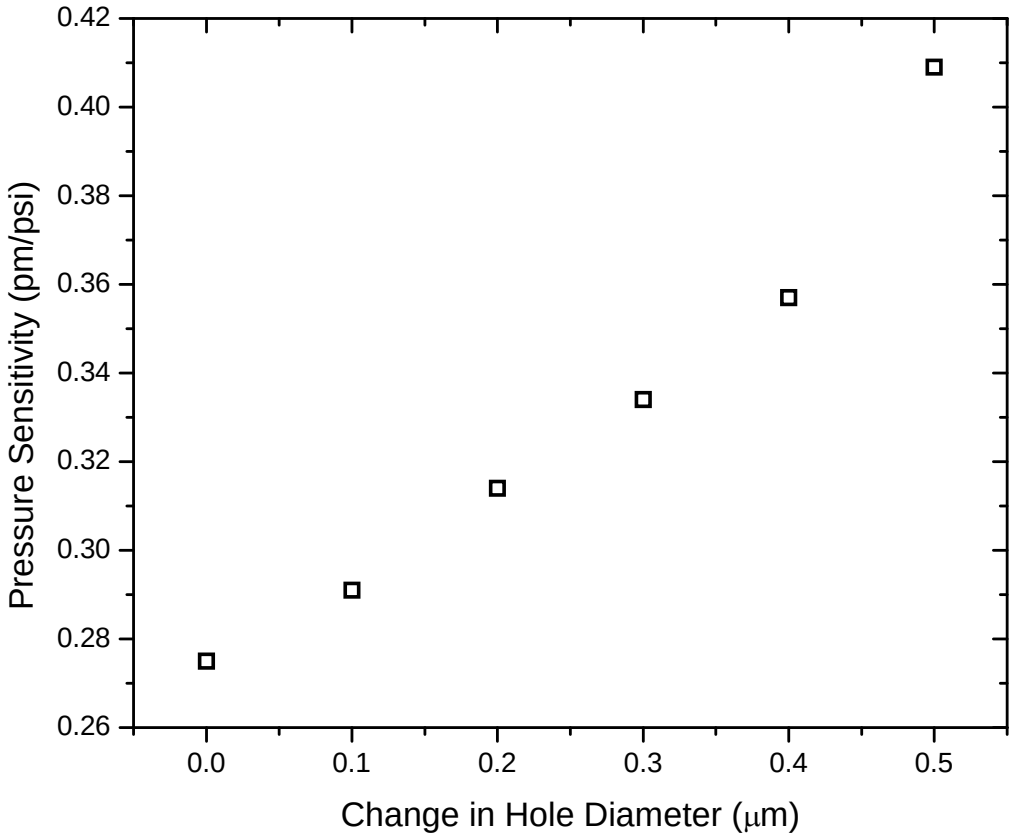

Figure 50: Simulated sensitivity increase with etching

Figure 50 clearly shows that by increasing the air-hole diameter it is possible to increase the overall sensitivity of the fiber. This is in good agreement with previous results for the etching of the two-hole fiber. With an increased diameter of 0.5 μm in the air-holes the overall sensitivity of the sensor is 0.409 pm/psi. This is a significant improvement over the unetched fiber and approaches the sensitivity of the tear-drop fiber design.

In order to obtain the best shape and pressure sensitivity there must be an increase of 1μm in the diameter of the fiber cross section. The etching results in the removal of the bridge spacing between the air-holes and an increase in the sensitivity to an applied transverse pressure. The maximum sensitivity obtained for the shape is 0.429 pm/psi. The shape of the fiber and the birefringence through the cross section can be seen in Figure 51.

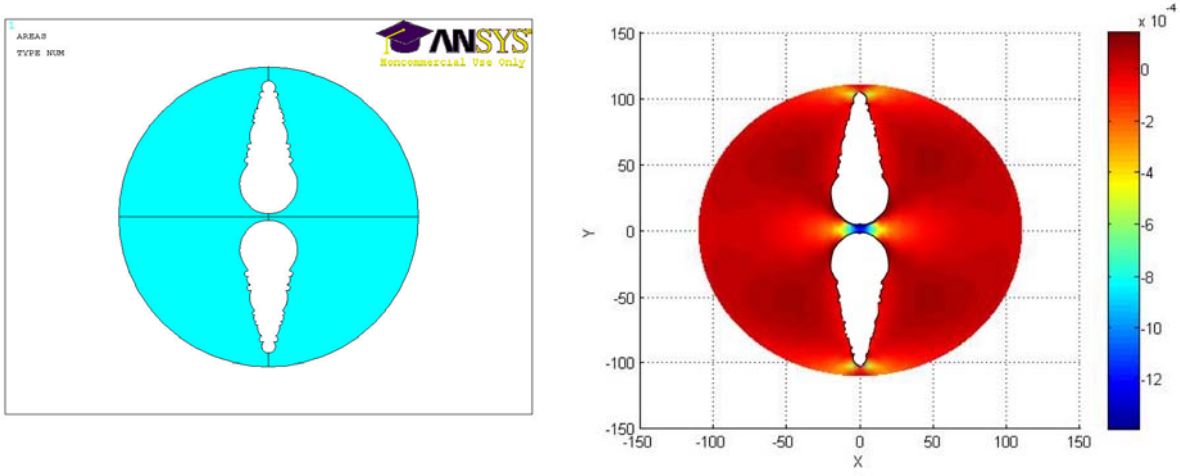

Figure 51: Etched tear-drop fiber (left), birefringence through etched cross-section with 200 bar applied pressure

4.3 PHOTONIC CRYSTAL FIBER DESIGN

The fiber was designed to be in single-mode operation at 1550 nm and at the same time to have large intrinsic birefringence. The air-hole matrix design is based on a square lattice, which can be modified to exhibit large birefringence [18, 19]. The air hole matrix has a 1.34μm pitch (Λ) and 0.66 μm hole diameter (d), respectively based on an existing PCF design [6]. These values led to an effective cladding index of 1.4 [7]. To form a fiber core, a single air hole in the middle row was taken out to create the fiber core. The asymmetry was introduced by displacing the central row of air holes on both sides of the fiber core by 0.46 μm. This displacement value was determined from the V-number calculation [7] that a core radius of 1.9 μm was the largest possible size to retain single-mode operation. All dimensions were measured from the center of the fiber core to the center of the adjacent air hole. This resulted in the core having radii of 1.99 μm and 1.34 μm along the x and y axis, respectively. This photonic crystal lattice design ensures single mode operation at 1550 nm with an intrinsic birefringence of 8.04×10^{-4}, this is obtained by the finite element analysis using COMSOL package using 3 rows of air holes above and below the fiber core.

To measure an applied hydrostatic load using fiber grating sensors, large air holes should be introduced into the fiber cladding [3, 44, 45]. Previous studies have shown [44] that improved sensitivity can be achieved by placing the fiber core close to the air holes. To ensure optimized pressure sensitivity, the air-hole photonic crystal lattice was placed in a close proximity of the large air holes with only one row of the air hole lattice separated between the fiber core and large hole as shown in Figure 52. The introduction of large air holes reduces the cladding index,

therefore, ensuring optical confinement using only one row of air hole above and below fiber core.

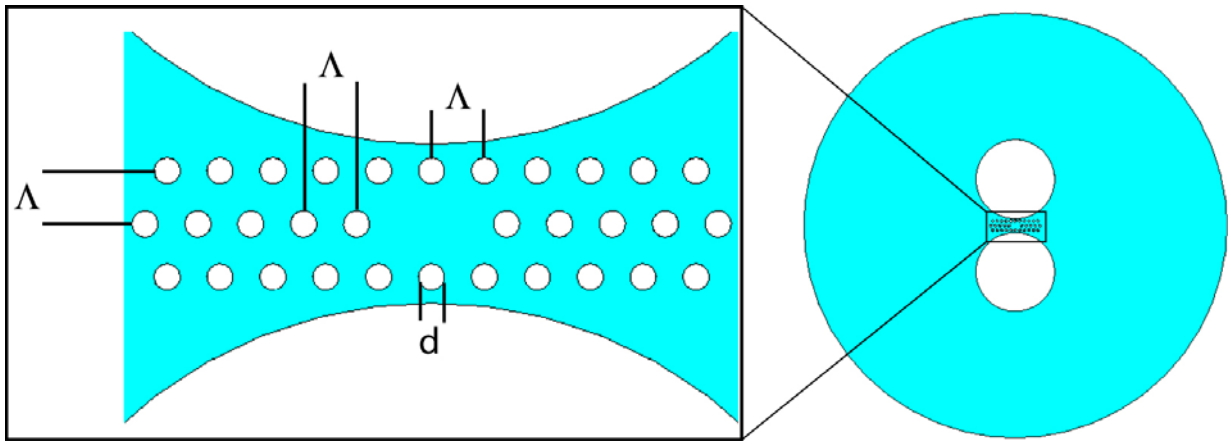

Figure 52: Schematic design of PCF matrix

Figure 53 shows the electrical field distribution of the fundamental mode for x and y polarization with the air hole radius of 11.629 μm. The distance between the edges of the large air hole to the center of the upper row of air hole matrix is 0.66 μm. The index of refraction of silica was calculated using the three-term Sellmeier polynomial [46] where it was assumed to have a refractive index of $n = 1.44504$ at 1550 nm, while the air-holes had a refractive index of n = 1. The resulting initial birefringence for the two-hole PCF with the asymmetric core at 1550 nm is 1.16×10^{-3}. The electric field distributions of the fundamental mode for the x (n_o=1.406739) and y (n_o=1.405579) polarizations are presented in Figure 53. The introduction of two air holes actually increases the birefringence to 1.16×10^{-3}, which is 1.44 times larger than the fiber core that used three rows of air holes for the optical confinement.

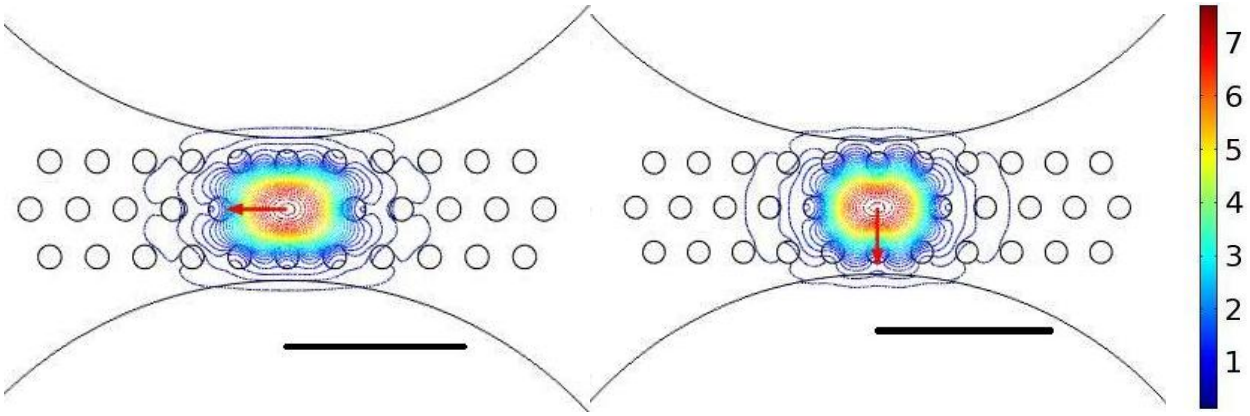

Figure 53: Electric field distribution of the fundamental mode for x (left) and y (right) polarizations, the scale bar in the Figure indicate 5 µm.

Numerical simulation also reveals that the air hole lattice cannot support a well confined single mode if only one or two rows of air holes were used above and below the fiber core, due to reduced index contrast between the fiber core and the effective cladding index. This is confirmed in Figure 54 for the case of one row of air holes.

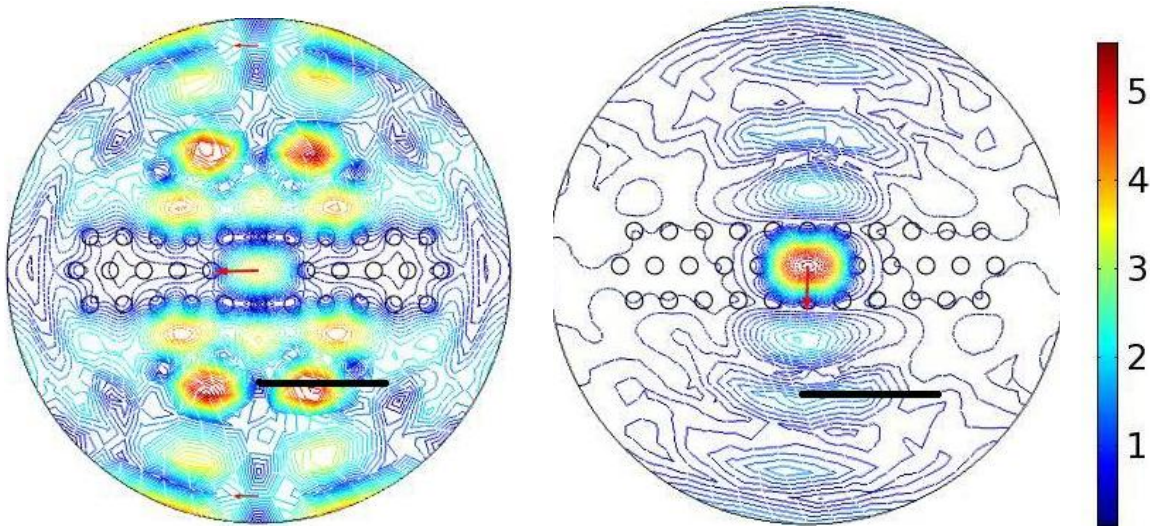

Figure 54: Electric field distribution of the fundamental mode for x (left) and y (right) polarizations for single-row PCF matrix in the center region of the fiber, the scale bar indicates 5 µm.

Given the fact that one row of air holes above and below the fiber core cannot confine guided modes, the replacement of the additional rows of air holes by a pair of single large air holes will have a significant impact on the fiber core's optical confinement. Therefore, the overall radius of the single large air hole was studied to observe how the air hole radius effects modal confinement. To observe the dependency of the radius of curvature of the air-hole, the radius of the round holes were increased while maintaining the spacing between the PCF matrix and the edge of the air-hole in order. The effective index for the two Eigen-modes (n_x and n_y) for the fundamental mode are presented in Figure 55.

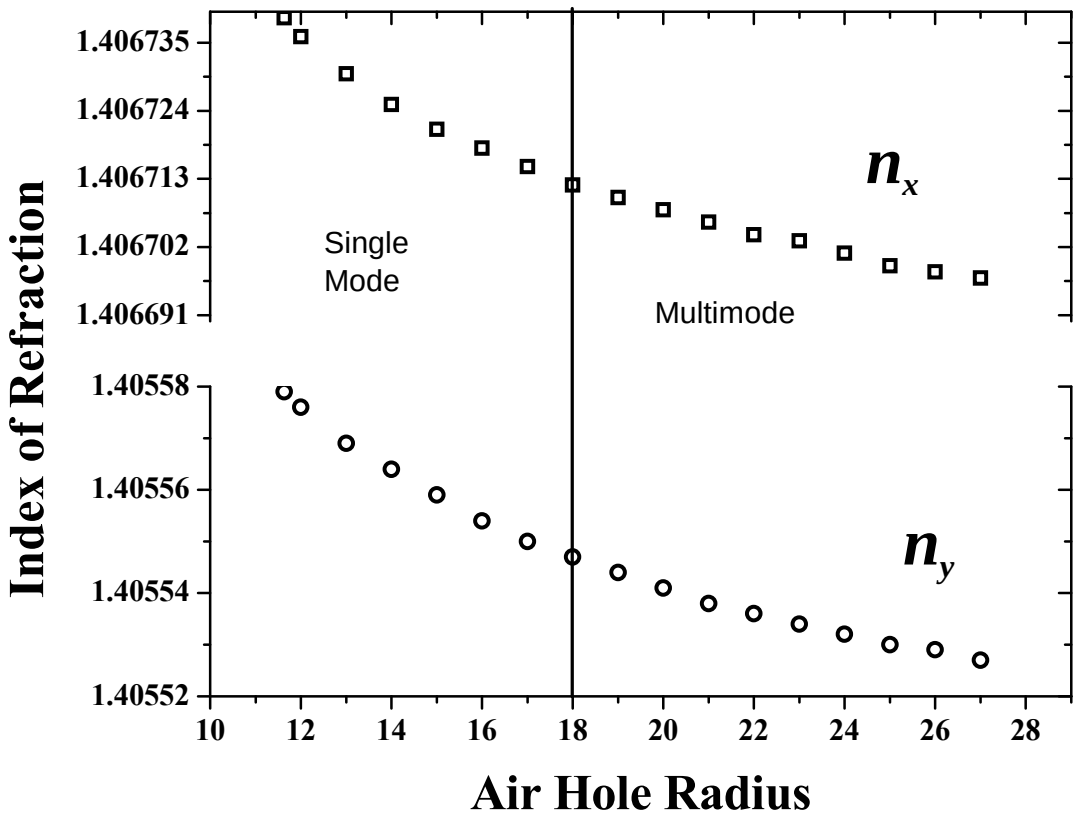

Figure 55: Effective index of refraction for nx (top) and ny (bottom) vs hole radius

As the radius of curvature for the air-hole increases the indices of refraction for the two polarization modes decrease exponentially. The fiber remains in single mode operation up to an air-hole radius of 19 μm, at this limit, higher order modes begin to appear. The fiber that possessed the large air-hole with a radius of 11.629 μm possessed effective indices of refraction of 1.406739 and 1.405579 for the two orthogonal polarized modes, respectively, which results in a birefringence of 1.160×10^{-3}. The fiber birefringence changes to1.165×10^{-3} when the radius of air hole increases to 18 μm.

Although the indices of refraction for both polarizations and the birefringence of guided modes are only moderately affected by the change in the air hole sizes, modal confinement is heavily influenced by the radius of the large air hole. Higher order modes are produced when the air hole radius goes beyond 19 μm, which is due to the reduction in effective index of the cladding due to the increased size of air holes. Figure 56 presented guided mode profiles for both x- and y- polarization with the air hole radius of 24 μm. The trend of the fiber to shift into multimode operation with an increasing air-hole radius also eliminates the possibility to use a pair of large air-hole to effectively transfer the hydrostatic load to the core region as demonstrated with the fiber with a conventional fiber core made of Ge-doped silica [3, 44, 45].

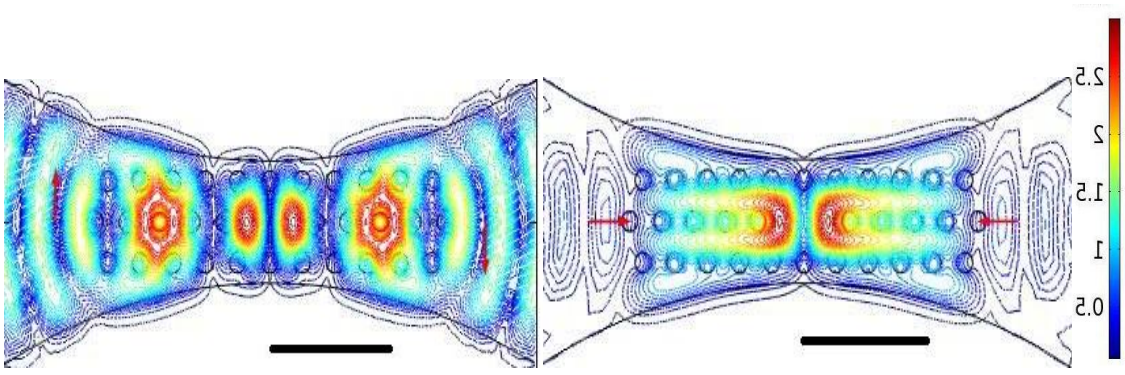

Figure 56: Higher order mode profiles with air hole radius of 24μm.

4.4 FIBER OPTIMIZATION FOR PRESSURE MONITORING

When a microstructured optical fiber is placed under an applied transverse load such as a hydrostatic pressure, the air-holes in the fiber cladding deform and transfer the induced stress into the central core region. The resulting stress induces a birefringence that is governed by the following equations [20, 21]

$$n_x = n_0 + C_1\sigma_x + C_2\left(\sigma_y + \sigma_z\right)$$
$$n_y = n_0 + C_1\sigma_y + C_2\left(\sigma_x + \sigma_z\right) \qquad (3.1)$$

where n_x and n_y are index of refractive for two linear polarization, C_1 and C_2 are the stress optic coefficients with values of $-6.9\text{x}10^{-13}$ m^2/N and $-41.9\text{x}10^{-13}$ m^2/N, respectively and σ_1-σ_3 are the principal components of the induced stress. Only the first two components of the index change are needed due to a two-dimensional reduction of the model via plane-strain assumptions. The pressure sensitivity of the phase modal birefringence is determined by the difference between the loaded and unloaded birefringence with respect to the applied load:

$$\frac{dB}{dP} = \frac{B_{Loaded} - B_{unloaded}}{P}, \qquad (3.2)$$

The phase and group modal birefringence are two important parameters that are used to characterize birefringence in optical fibers. The phase modal birefringence is defined by the difference between n_x and n_y

$$B = \Delta n = n_x - n_y \,, \tag{3.3}$$

corresponding to the slow and fast axis, respectively. The group birefringence, $G(\lambda)$ is defined as

$$G = B - \lambda \frac{dB}{d\lambda} \,, \tag{3.4}$$

Where $dB/d\lambda$ is the chromatic dispersion of the phase modal birefringence

The phase model birefringence as a function of wavelength (1.0 μm-1.6 μm) for an unloaded fiber was calculated for the asymmetric core design. The discrete values of B(λ) were numerically adjusted with a second-degree polynomial, allowing for the calculation of the dispersion term dB/dλ and determination of G(λ). The phase and group modal birefringence are plotted versus wavelength for the initial design at base pressure and the initial design, small circle design and the etched design for an applied hydrostatic pressure of 20 MPa in Figure 57.

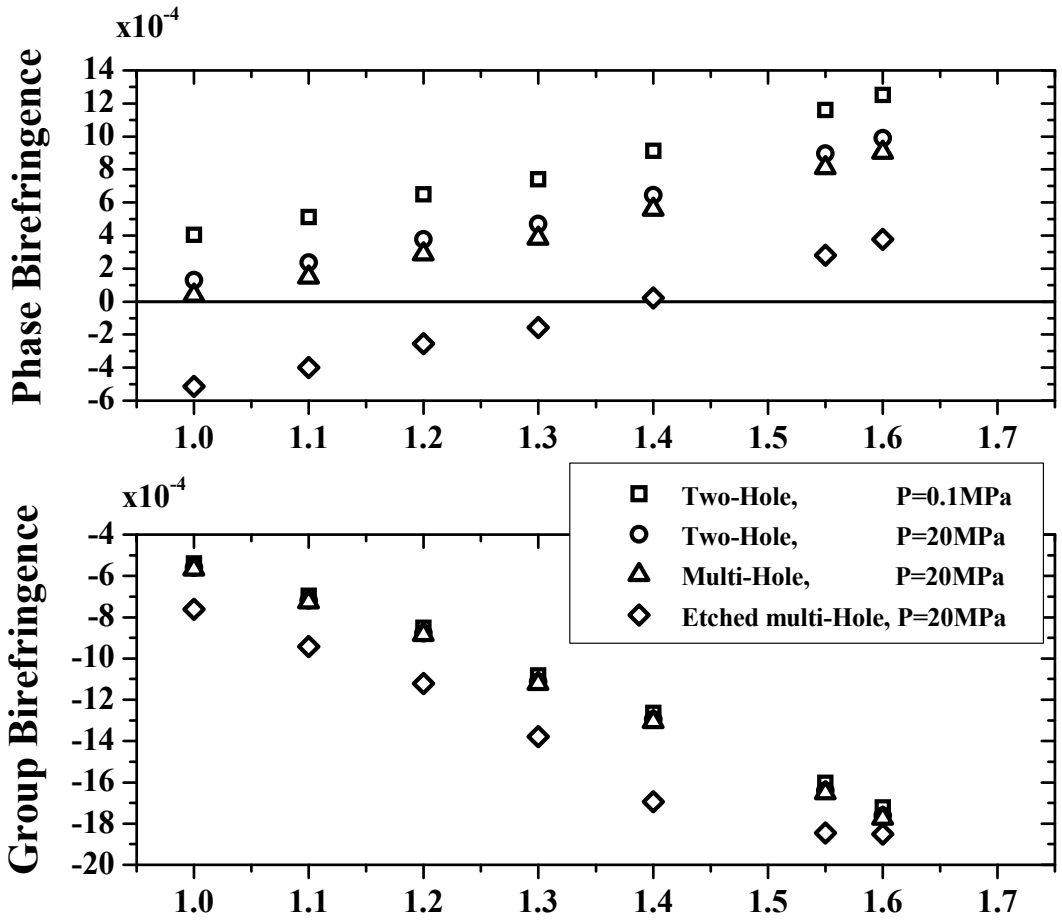

Figure 57: Wavelength dependence of the phase and group modal birefringence

In the selected coordinate system the phase modal birefringence (B) is positive, whereas the group modal birefringence (G) is negative. The difference in sign between the phase and group birefringence is caused by a highly anomalous chromatic dispersion in the phase modal birefringence ($dB/d\lambda>0$). This is different than what occurs in traditional highly birefringent fibers where the chromatic dispersion ($dB/d\lambda$) is significantly smaller [47, 48].

Figure 57 also simulates the fiber sensitivity to external pressure. Under an external hydrostatic pressure of 20 MPa, the two-hole fiber with the PCF core incurs a birefringence to pressure sensitivity of 0.1317×10^{-4}/MPa, if a fiber Bragg grating (FBG) sensor is inscribed in the fiber, this pressure sensitivity will lead to ~13.34 pm/MPa. This is 11% less than the previous report using larger air hole solid core fiber (~ 14.79 pm/MPa) [44]. This is not a surprise due to the smaller air holes used as pressure transducers. As revealed in the simulation, the further increase of the air holes will induce multi-transverse modes, which is not desired for sensing applications.

To increase the sensitivity of the fiber while maintaining single-mode operation for the PCF fiber core, a row of smaller air holes are added to the cladding, which extends from the out-edge of the 30 μm air hole to the edge of the fiber as shown in Figure 58. This row of air holes has diameters of 5.68 μm and 0.5 μm spacing, which is manufacturable in the fiber perform preparation stage. The addition of air holes has no impact on the single-mode operation of the PCF core, while increasing the compressive stress in the x-polarization in the core region. It is also possible to increase the fiber sensitivity by etching away the silica bridge between two adjacent air holes using a buffered oxide etching (BOE) process [44]. This can be accomplished in the fiber perform before the drawing process, with the core region being able to be sealed from the BOE process. The etching process will remove the silica bridges by etching an amount of the

small air holes as shown in Figure 58, which improves the pressure transduction into the core region.

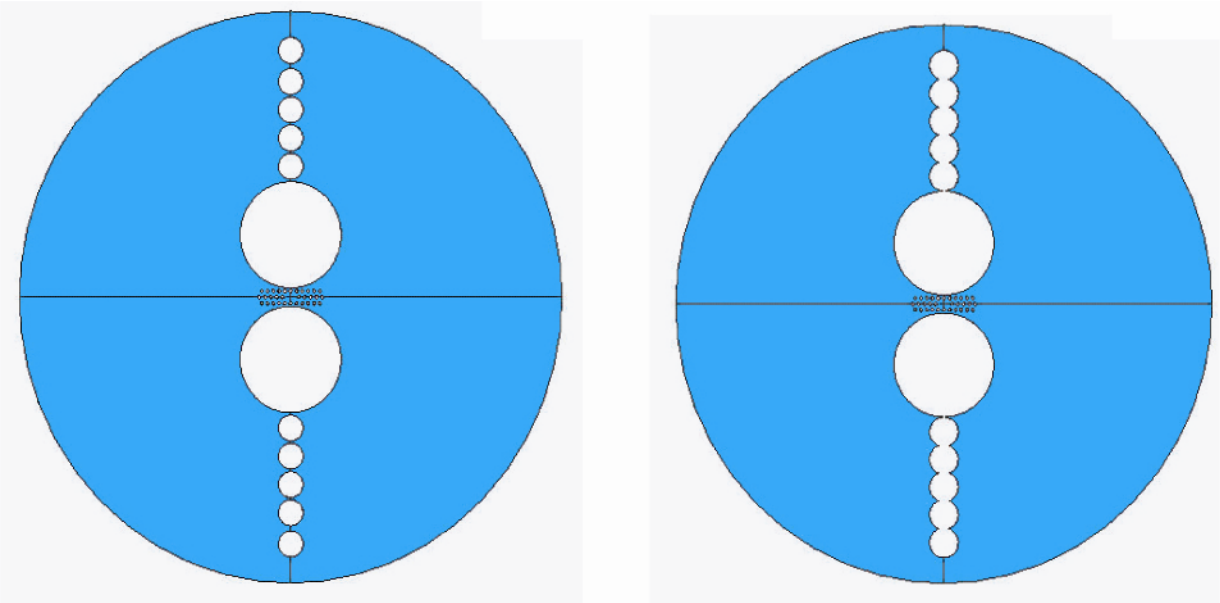

Figure 58: Multi-hole fiber geometry (left), etched fiber geometry (right)

Figs. 59 presents the finite element analysis (FEA) stress analysis of the air-hole fibers before and after etching along x-axis, which is the dominant stress component. The etching process leads to significant increase of compressive stress along x-axis in the core region. The average compressive stress over the entire PCF core region is increased by 2.55 times (from -119.947 to -304.328 at 20 MPa). Figure 60 presents the overall induced birefringence through the fiber cross-section of the etched geometry.

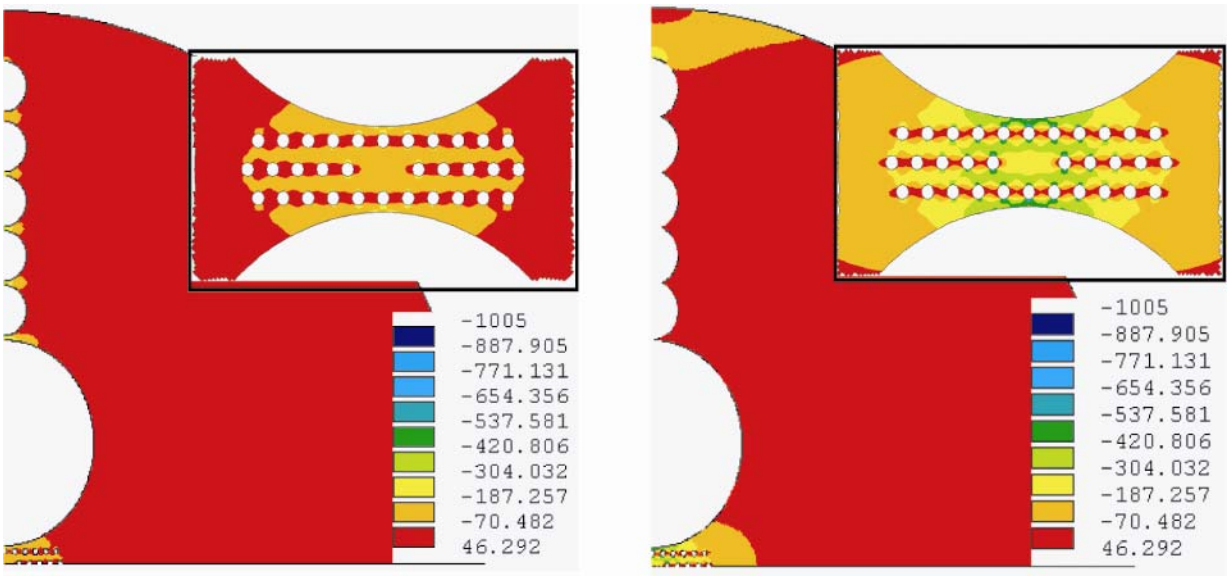

Figure 59: Stress profile for x-component of stress for the Multi-hole Fiber before (left) and after (right) chemical etching, the color bar has unit of MPa

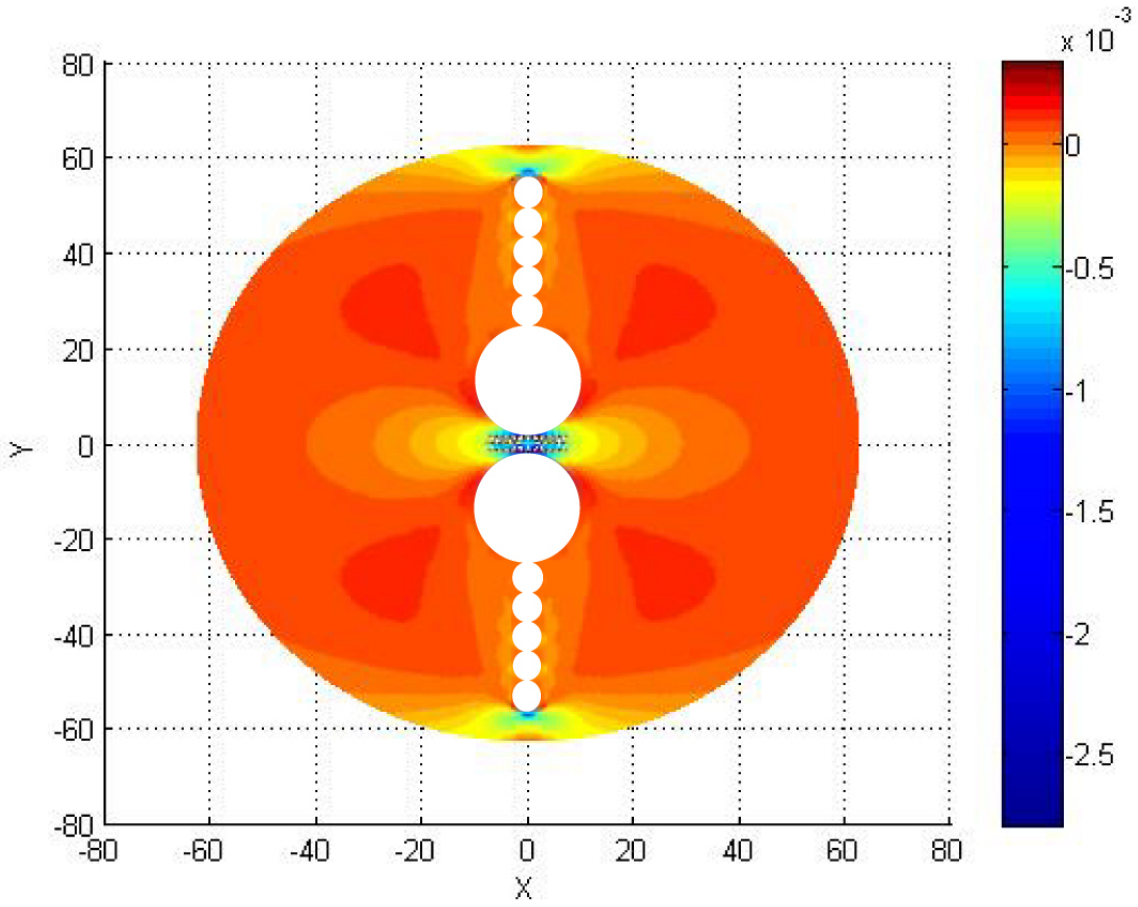

Figure 60: Birefringence (n_x-n_y) for the etched PCF fiber at 200 bars

The FEA analysis also confirms the significant increase of birefringence pressure sensitivity. Figure 61 presents the phase modal birefringence as function of the pressure for two-hole PCF (11.6 μm diameter air hole), two-hole PCF with addition of air-holes before and after the BOE process. Etching the air holes in the cladding results in a birefringence-pressure coefficient and FBG pressure responsivity of $43.89 \times 10^{-6} MPa^{-1}$ and 44.15 pm/MPa, respectively, a 3 times improvement over the multi-hole fiber and a 17 times improvement over what has previously been demonstrated in PM-PCFs [10-12, 23, 24] and more than four times better than the recent results in the Hi-Bi microstructured fiber [14].

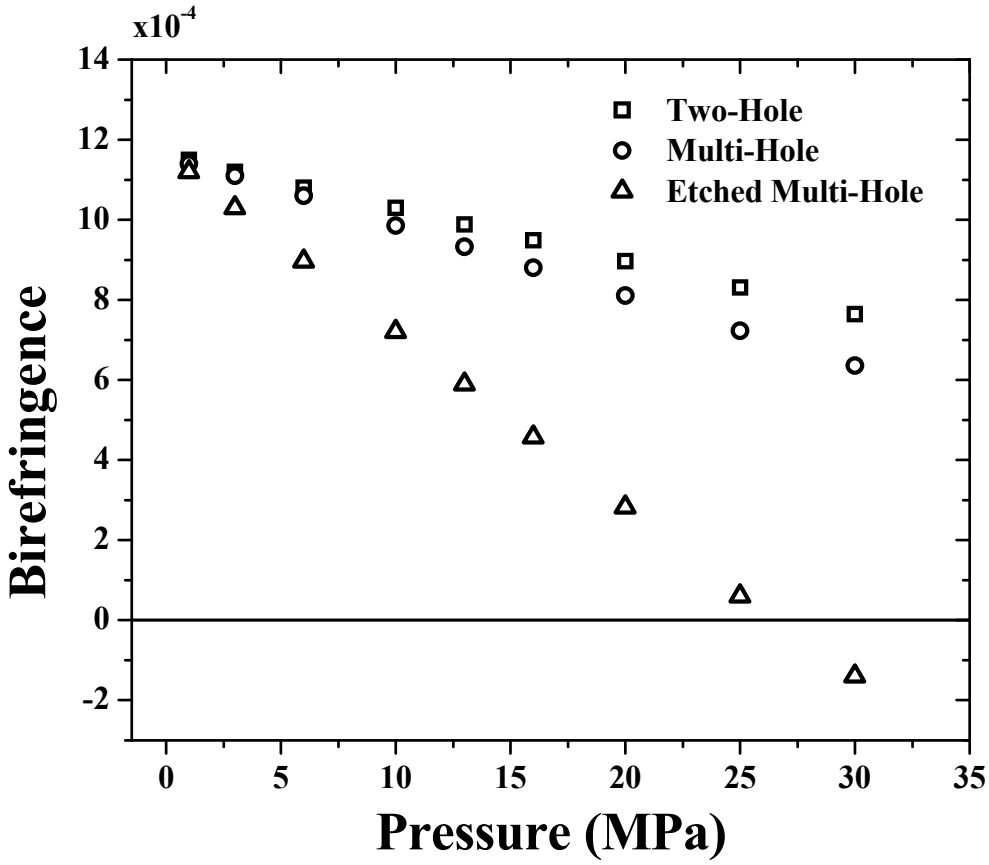

Figure 61: Pressure sensitivity of phase modal birefringence

4.5 SUMMARY

In Summary, this chapter presents numeric studies of side-hole fiber with a highly birefringent PCF core. It shows that the introduction of large air holes in the fiber cladding for sensing applications has a significant impact on the optical properties of the PCF fiber core. Special considerations have been given during the fiber design to ensure single-mode operation with good modal confinement. At the same time, the configuration of the air holes in the fiber cladding also influence the sensitivity of the fiber sensor. Both facts have to be considered simultaneously to achieve an initial high birefringence and side hole array to maximize the sensor's sensitivity.

In this chapter, I presented an air hole matrix in the fiber cladding and a practical chemical etching process during the fiber perform preparation stage to produce a highly birefringent photonic crystal fiber with a birefringence-pressure coefficient of 43.89×10^{-6} MPa^{-1} or a FBG pressure responsivity of 44.15 pm/MPa.

5.0 SUSPENDED CORE FIBER SENSORS

5.1 PREMISE

The inception of air-hole microstructured fibers over the past 20 years has brought fiber optics into a new era. The incorporation of an air hole matrix brought a new dimension of flexibility in designing and fabricating optical fiber with various peculiar properties useful for optical communication and sensing. One of the interesting air-hole structures incorporated in microstructured fibers is the suspended core fiber with thin bridge supports.

The suspended core optical fiber (SCF) has benefits over that of traditional microstructured optical fibers, the first of these being primarily the confinement of the optical signal. SCFs typically rely on modified total internal reflection (mTIR) due to the small core, bridge thickness, overall size of the air holes and the resulting index contrast. The lack of a doped core can allow for the creation of optical fibers with increasingly small cores with low loss, low dispersion and strong confinement.

Despite these benefits, the mechanical behavior of these fibers is not well understood. In this chapter I will present several applications of these fibers as optical sensors including the ability to be directional dependent sensors, bending insensitive sensors and new designs that are immune to an applied transverse load.

5.2 DIRECTIONAL DEPENDENT SENSOR

5.2.1 Introduction

In the past decade, fiber Bragg grating (FBG) sensors have found many interesting applications in the field of structural health monitoring. Their compact size field ruggedness and immunity to electromagnetic interference makes FBG sensors excellent candidates for sensing applications in harsh environments. Currently, most FBG strain gauges used in structural health monitoring applications are inscribed in standard telecommunications fiber. As strain gauges, the measurement sensitivity and directionality is inherently limited by the fiber structure and the mechanical properties of the silica material [20]. For example, FBG sensors inscribed in standard fibers cannot measure the orientation of transverse load due to the cylindrical symmetry of the fiber [20]. To overcome these limitations, microstructured optical fibers (MOF) have been developed to improve the functionality of these fiber sensors [49-51]. The addition of varying air-holes geometries within the fiber cladding has allowed for the creation of fibers that posses properties that are unattainable with normal silica fibers.

Recent work has been performed on MOFs with an initial large birefringence in addition to photonic crystal fibers (PCFs) [10-14, 22-27, 44, 45, 47-49], examining increased sensitivity and directional dependence on the induced birefringence due to an applied transverse load. The problem arises in that the fibers either experience a slight change in sensitivity based upon the orientation [49, 50] or experiences a sensitivity that is of equal magnitudes [51] making data processing difficult. To overcome these limitations, a fiber structure must be used that possesses a single orientation that is highly sensitive to the applied load.

In this section, I present FBG sensors inscribed in a four-hole suspended core fiber [19, 20, 52, 53]. FBGs with this fiber structure are more sensitive to the applied transverse load than standard fibers and posses an orientation dependency to transverse loads. With this unique trait, it is possible to create an embedded fiber strain gauge that can simultaneously measure both magnitudes and directions of axial and transverse strains.

5.2.2 Simulation

When an air-hole microstructured fiber deforms under an applied transverse load, the induced stress throughout the fiber is affected by the air hole geometry. It has been shown that it is possible to focus or deflect the stress away from the fiber core by proper design of the air hole matrix [44]. The stress distribution throughout the fiber can be simulated using a finite element analysis (FEA) model and can then be related to induced birefringence in silica glass using the model developed by Gafsi and El-Sherif [20]. Figure 62 shows a SEM photograph of the four hole suspended core fiber. Birefringence data was calculated from the stress distribution using a 2-D plane-strain FEA model (ANSYS v. 11.0). The diameter of the fiber, air holes and bridge thickness are 123.2 μm, 25 μm, and 0.9 μm respectively. Simulations of the induced birefringence under a transverse load of 50 N/cm for the two fiber orientations (bridge and hole under the vertical applied load) are shown in Figure 63. The birefringence ($B=\Delta n_x-\Delta n_y$) induced in the vertical stem orientation is 5.948×10^{-4}, which is over 22 times larger than that for the vertical hole orientation of 2.624×10^{-5}. The birefringence over the face of the fiber for an applied load of 50 N/cm is presented in Figure 64.

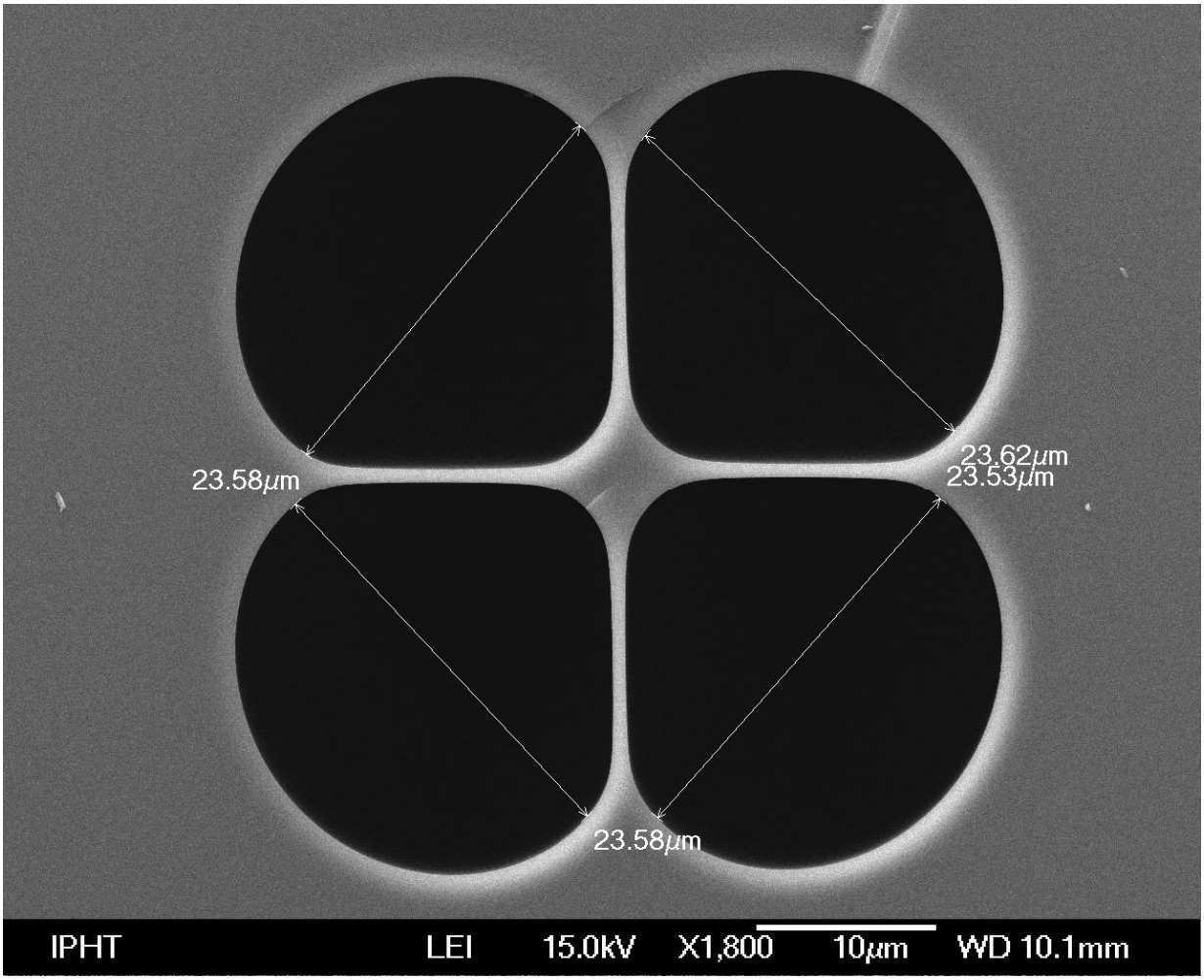

Figure 62: SEM photograph four-hole suspended core fiber (provided from the Institute of Photonic Technology, Jena, Germany)

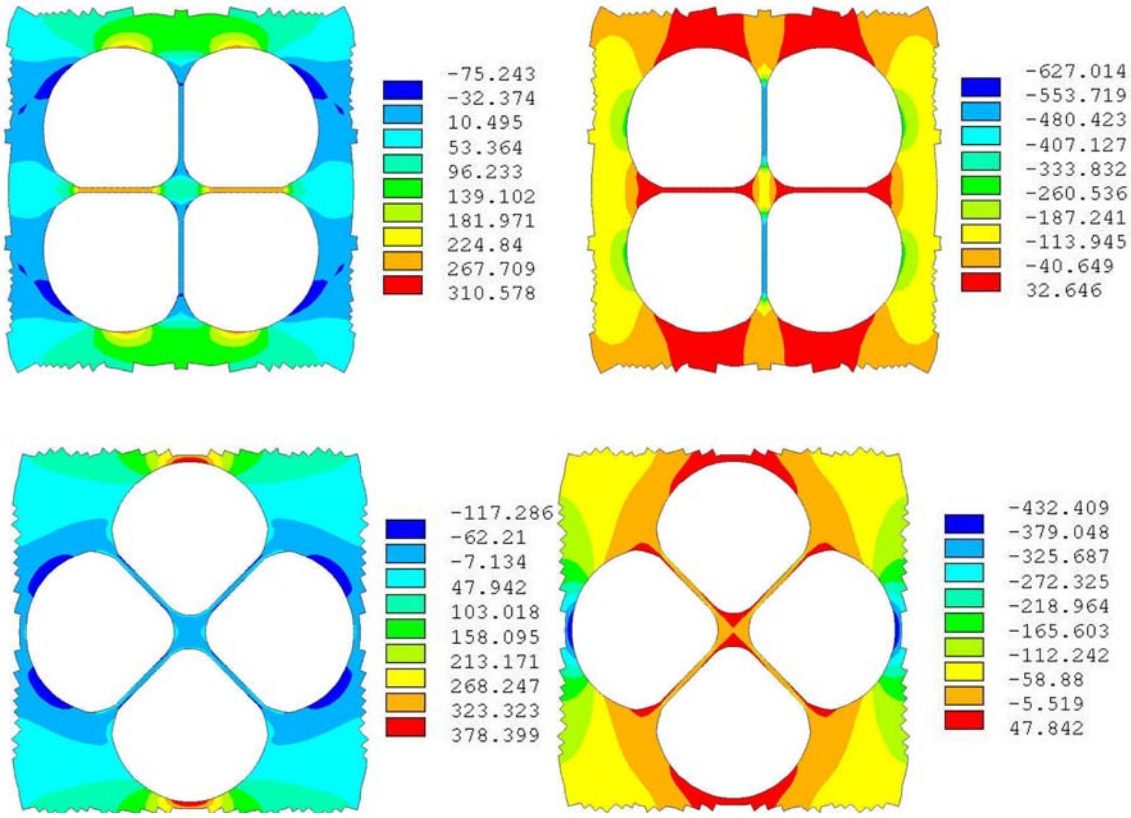

Figure 63: FEA simulation of birefringence of the fiber under a 50 N/cm vertical load.

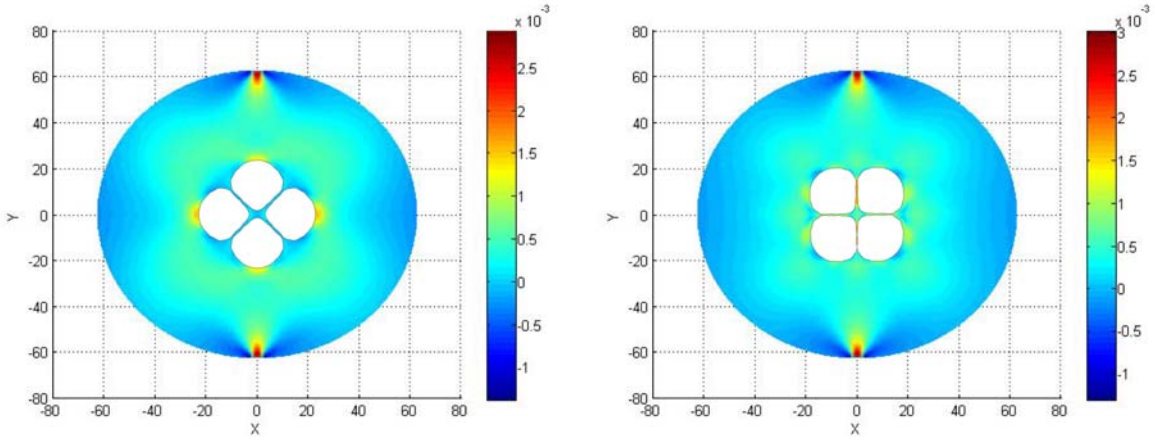

Figure 64: Birefringence (nx-ny) for hole (right) and stem (left) under a 50 N/cm load

5.2.3 Experiment

In order to verify the simulated results, a directional compression test was performed on the four hole suspended core fiber with fiber Bragg gratings included. Due to the pure silica material of the fiber conventional UV writing of Bragg gratings is not possible and also hydrogen loading is also difficult because of the fast out diffusion of the small core region. Therefore all gratings were generated by using an UV fs laser inscription technique with a Talbot interferometer [54]. Because of the femtosecond laser radiation there is no conventional photosensitivity needed. A master oscillator with power amplifier configuration consisting of a Mantis oscillator source together with Legend amplifier, (both by Coherent) was used. The resulting IR femtosecond laser beam is then frequency tripled to a wavelength of 262 nm with an average power of 0.7 W (with 1 kHz repetition rate). Thanks to the interferometric configuration it is possible to adjust the grating wavelength in the entire telecommunication C band [54]. The gratings in the suspended core fiber have a wavelength of around 1542 nm with reflectivity higher than 70%.

A schematic of the compression experimental setup can be seen in Figure 65. The transverse load testing was performed using a custom-built compression stage. A suspended core fiber containing the FBG was placed between the upper plate and the anvil that contained the load cell. In order to determine the fiber's orientation a rotation stage was used in conjunction with a microscope objective, CCD camera and television monitor. A second dummy fiber was placed under the plate to ensure an evenly distributed load across the test fiber. The fiber was fusion spliced to the output port of a fiber circulator. A randomly polarized broadband ASE source was coupled into the input port of the circulator, reflection spectra of FBG was monitored by an optical spectrum analyzer (Ando 6317) connected to the return port of the circulator. To monitor the birefringence change, a U-bench was inserted in front of the OSA. A half-wave plate and a Glan-Thomson polarizer can be placed in the U-bench. By rotating the wave plate, the polarizer can select one of two orthogonal polarized modes of the fiber. The experiment was performed under two fiber orientations in order to properly monitor the directional dependency on the induced birefringence. The fiber was then rotated between the two orientations under a constant load to observe the angular dependency.

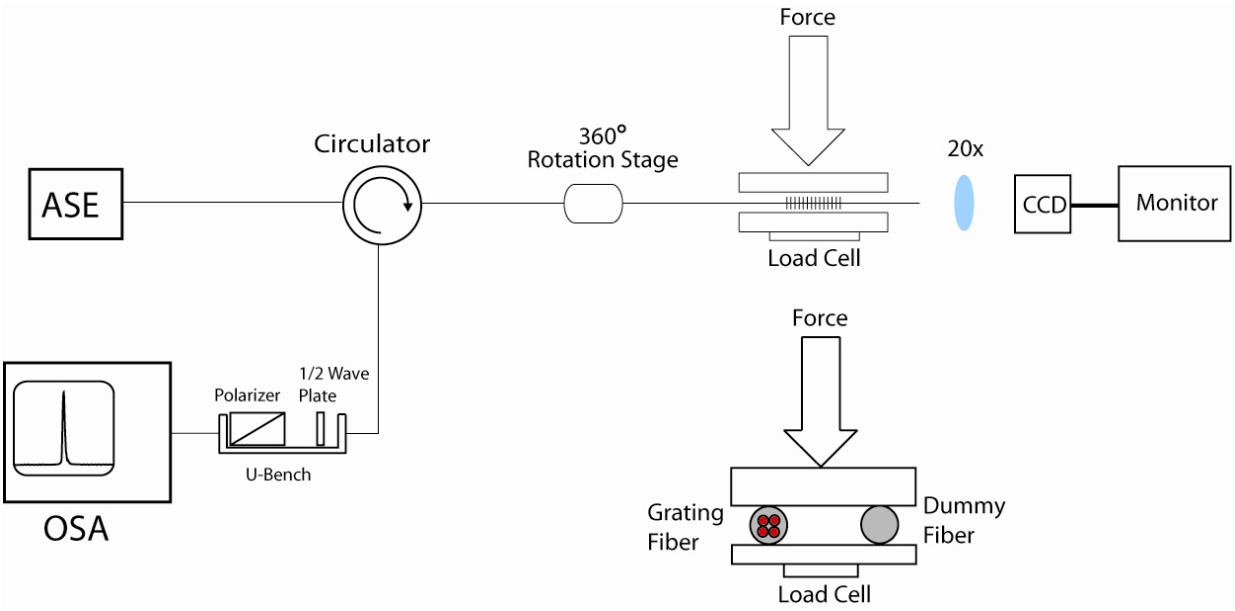

Figure 65: Compression Setup

The reflection spectrum of the FBG for the stem under the applied load is presented in Figure 66. It is clear that under the applied transverse load that the FBG resonance peak split into two separate from the original unperturbed state. Each peak represents one of two polarization eigen-states. To confirm that the two peaks were induced by the pressure-induced birefringence, a half-wave plate and a polarizer were dropped into the U-bench. The wave plate and polarizer allow the two eigen-states to be measured independently, confirming that the peak splitting is indeed due to the stress-induced birefringence. Figure 67 presents the FBG spectrum when the air hole is oriented under the applied load. In this case a significant decrease in the induced birefringence was observed.

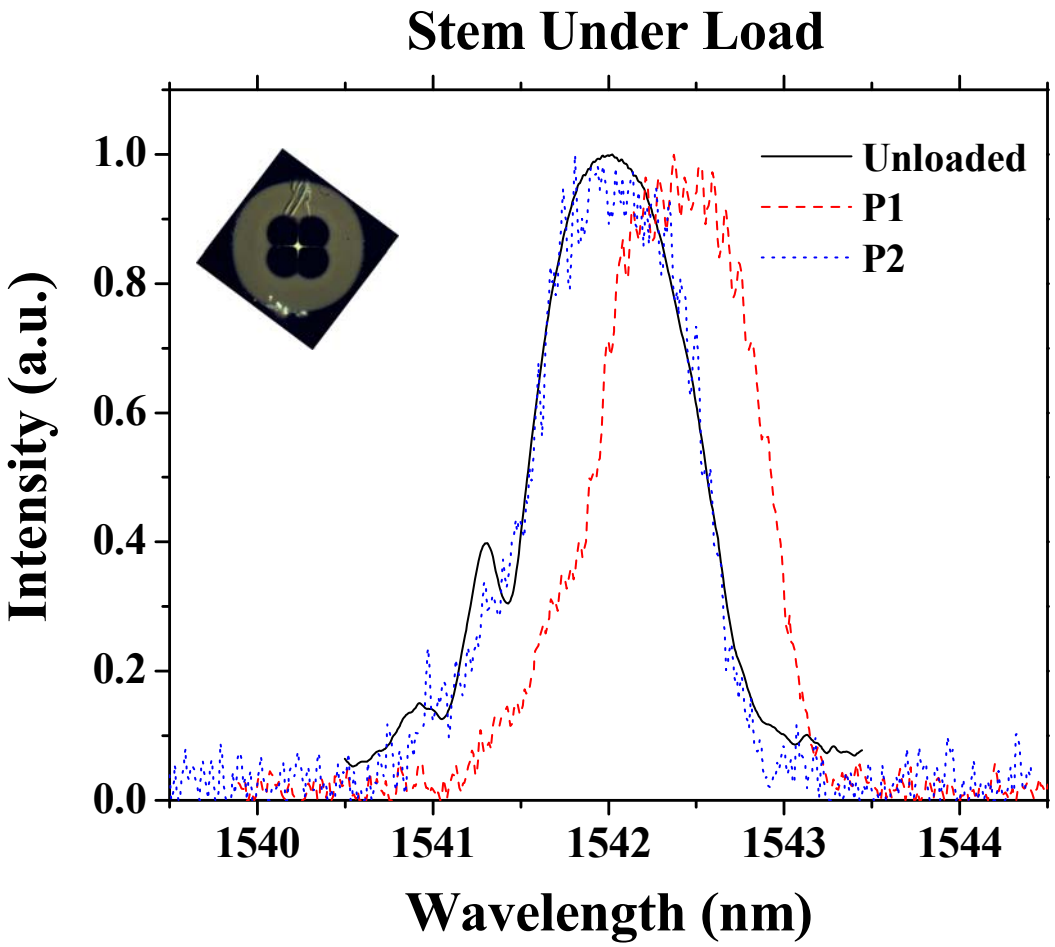

Figure 66: FBG peaks from two orthogonal polarizations under an applied transverse load of 47 N/cm for silica bridge under load.

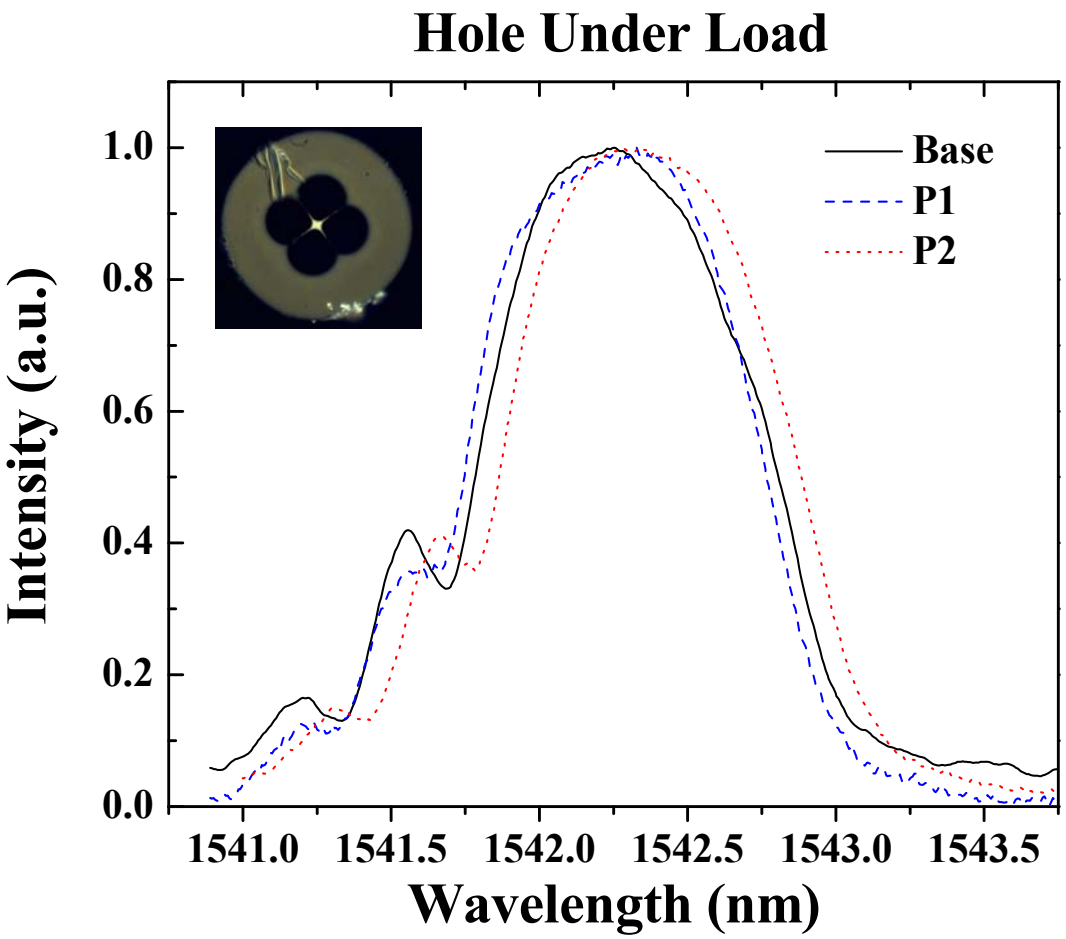

Figure 67: FBG peaks from two orthogonal polarizations under an applied transverse load of 47 N/cm for air-hole under load.

The overall response of the fiber sensor to an applied transverse load is presented in Figure 68 with the solid lines indicating the predicted values of induced birefringence. With the bridge and hole under the applied load the fiber yields a sensitivity of 12.228 pm/(N/cm) and 2.19 pm/(N/cm) when the load is less than 40 N/cm. At higher loads, the experimental results deviate from the simulation. The possible cause for this discrepancy could be that stems experience a buckling at higher loads.

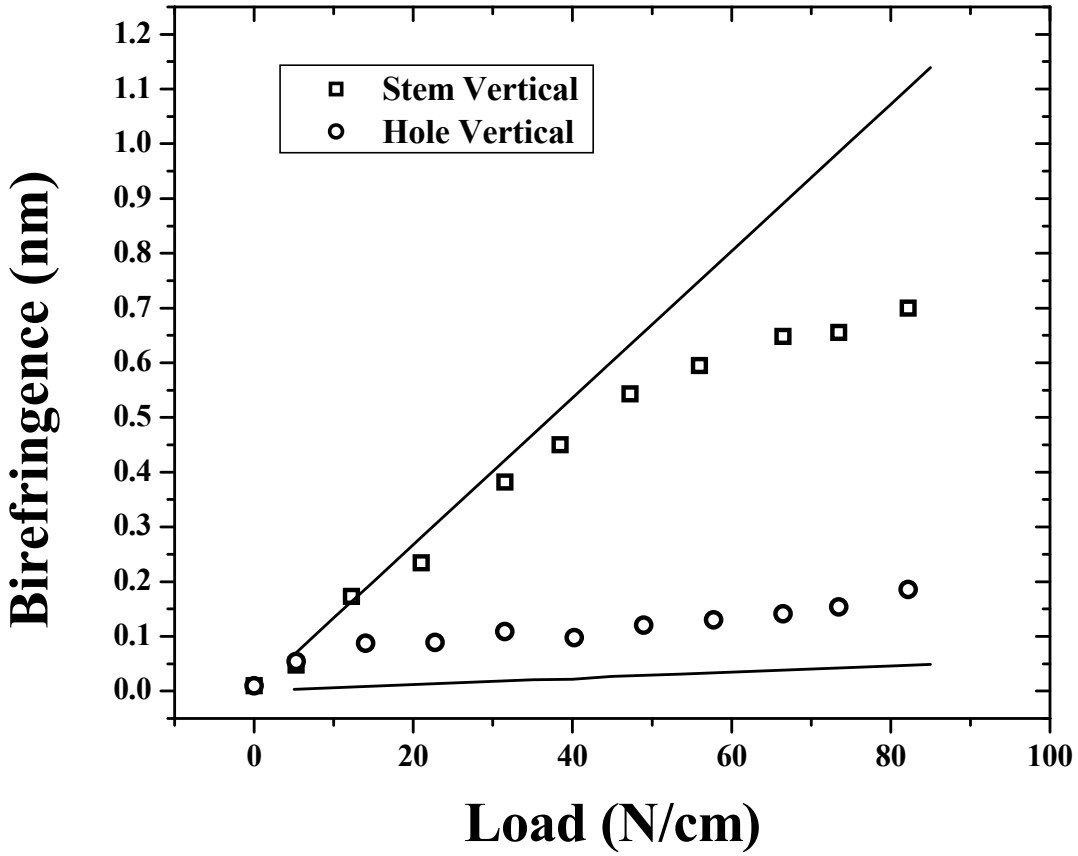

Figure 68: (left) FBG peak splits as functions of applied transverse loads,

The angular dependency on the induced birefringence was also studied and shown in Figure 69. Because of the unique symmetry in the fiber, one orientation (bridge vertical) is 5.58 times more sensitive than the other (hole). Experimental results show that the suspended core fiber has a minimum sensitivity of ~2 pm/(N/cm) when the air-holes are under load and ~12 pm/(N/cm). This is significantly smaller than that of simulation results (22 times). The four-hole fiber was placed under a constant load at different angles to determine the angular dependency on the induced birefringence. The simulation results predict an overall sensitivity of 0.588 pm/(N/cm) and 13.372 pm/(N/cm) at the air-hole (-45^{o} and 45^{o}) and stem (0^{o}) under the applied load. The cause of the discrepancy is currently unknown.

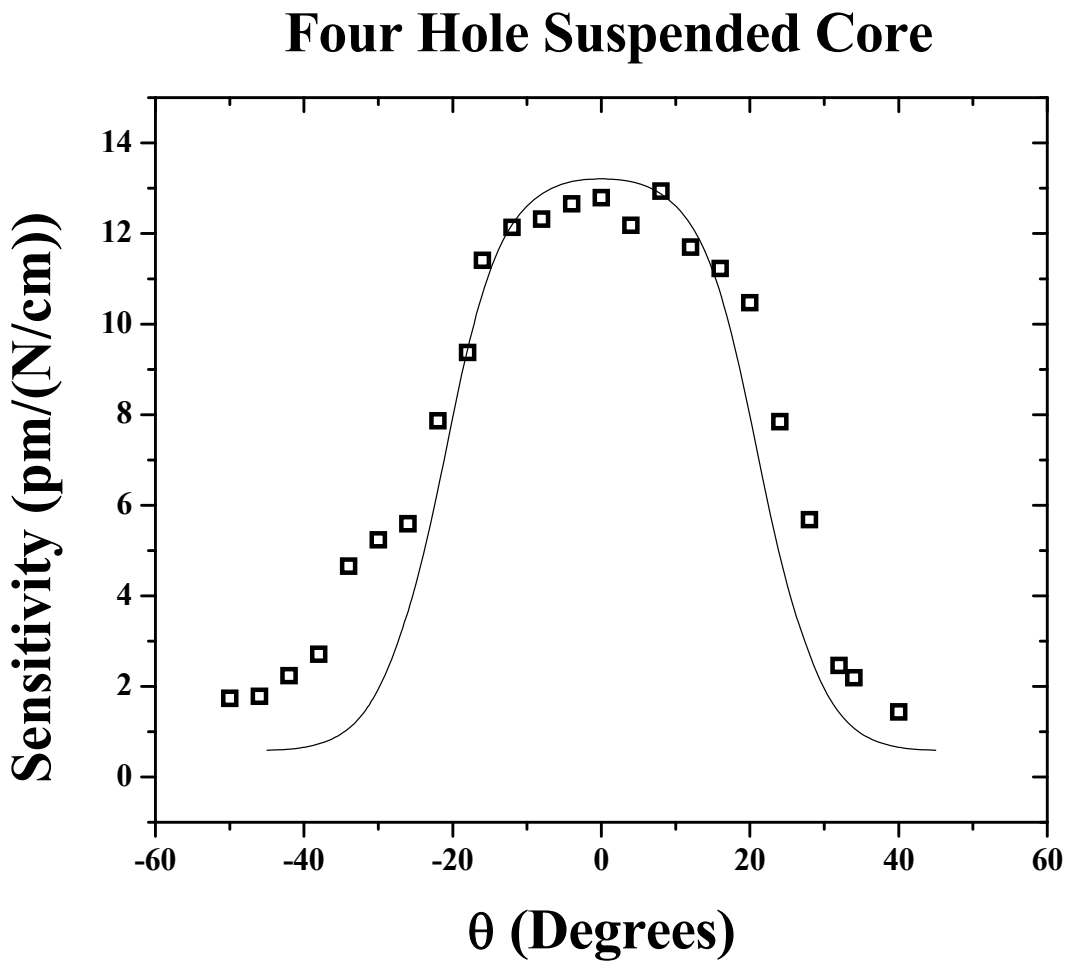

Figure 69: Compression sensitivity as a function of fiber orientations, the fiber is under 47 N/cm load.

5.2.4 Summary

In summary, I have presented work on a directional dependent transverse load sensor by employing the use of a suspended core optical fiber with FBGs. The unique fiber geometry allows for a sensor that one orientation is significantly more sensitive to the applied loads than the other.

5.3 BENDING INSENSITIVE SENSOR

5.3.1 Introduction

With the increasing trend to deploy fiber sensors into structural health monitoring systems there is increased interest in the ability to create fiber sensors that can separate the thermal and mechanical responses or unwanted deflections. One of these types of deflections that needs to be limited is the shift in the FBG from a vertical deflection of the fiber.

For embedded sensor applications, it is highly desirable to use FBG sensors to monitor the longitudinal strain along the fiber and the surrounding structure. However, if during deployment or operation the fiber experiences a bending, significant error can be introduced into the measurements. One such method to alter the response of the FBG is to inscribe the fiber into a suspended core optical fiber. These SCFs possess unique geometries that have been demonstrated to be highly orientation dependent to an applied transverse load in the previous section. With the thin silica bridge and directionality it is possible to create a fiber sensor that possesses lower sensitivity to bending with a directional dependency.

In this section I will present simulation and experimental results showing that 4-hole SCFs not only possess a smaller bending sensitivity than that of solid fiber but that based upon the geometry the bending axis results in a directional dependency upon the bending.

5.3.2 Simulation

The four-hole suspended core fiber used in this work was the same fiber used in the previous section. A finite element analysis (FEA) was performed using ANSYS v. 11.0 to simulate the effect that increased bending would have on the fiber. The model was a created using the PLANE183 element and then extruding the model with SOLID186 elements. Attention was given to ensure that the models were symmetrical about the x and y planes with consistently even meshing to ensure a proper solution was obtained. A solid model is necessary to determine the strain induced in the fiber core as a BEAM model does not permit for the calculation of internal strains or stresses. The model was extruded a length of 1 cm with 16 elements along the length (L) of the model. The fixed end of the model was constrained to allow no displacement or rotations with the free end of the fiber having an increasing displacement (U_y) applied which resulted in a decreasing radius (R). The model was solved via a non-linear Newton-Rhapson method because of the deflection shape caused by the displacement [55-60]. Figure 70 presents a view of the fiber model used in this section.

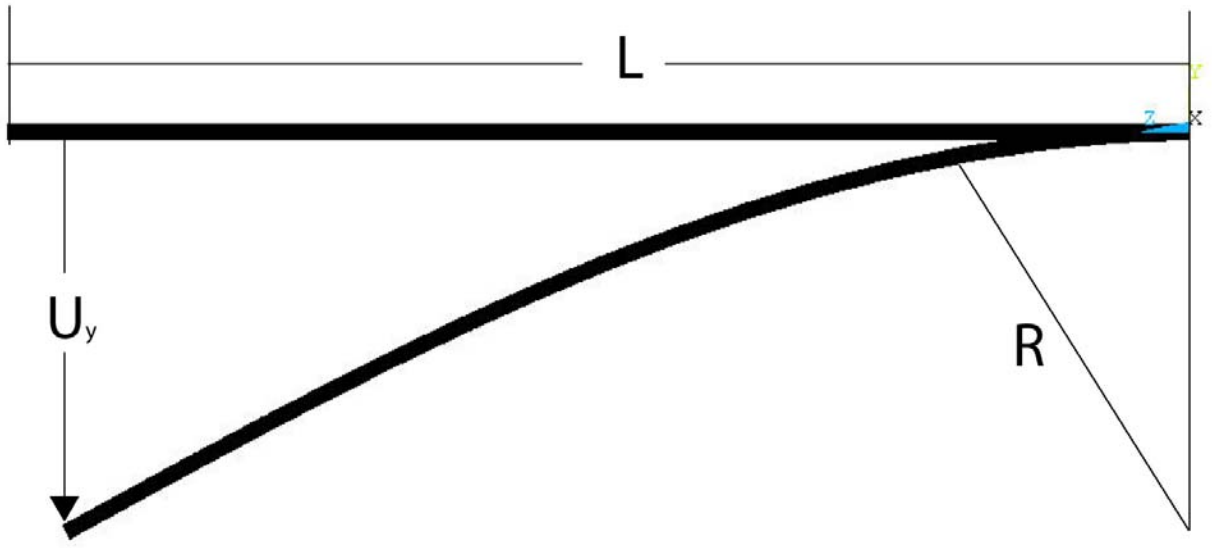

Figure 70: FEA simulation of fiber bending

The results of the FEA simulation are presented in Figure 71. What is immediately apparent is that SMF-28 has a significantly higher sensitivity to the applied bending than that of the SCF with the SMF-28 having 8.59 times more induced strain. The two orientations of the SCF also have different responses to the bending with the silica bridge parallel to the bending axis experiences a 1.4 times increase in strain than when the air holes are parallel to the bending axis with increasing curvature ($K=R^{-1}$).

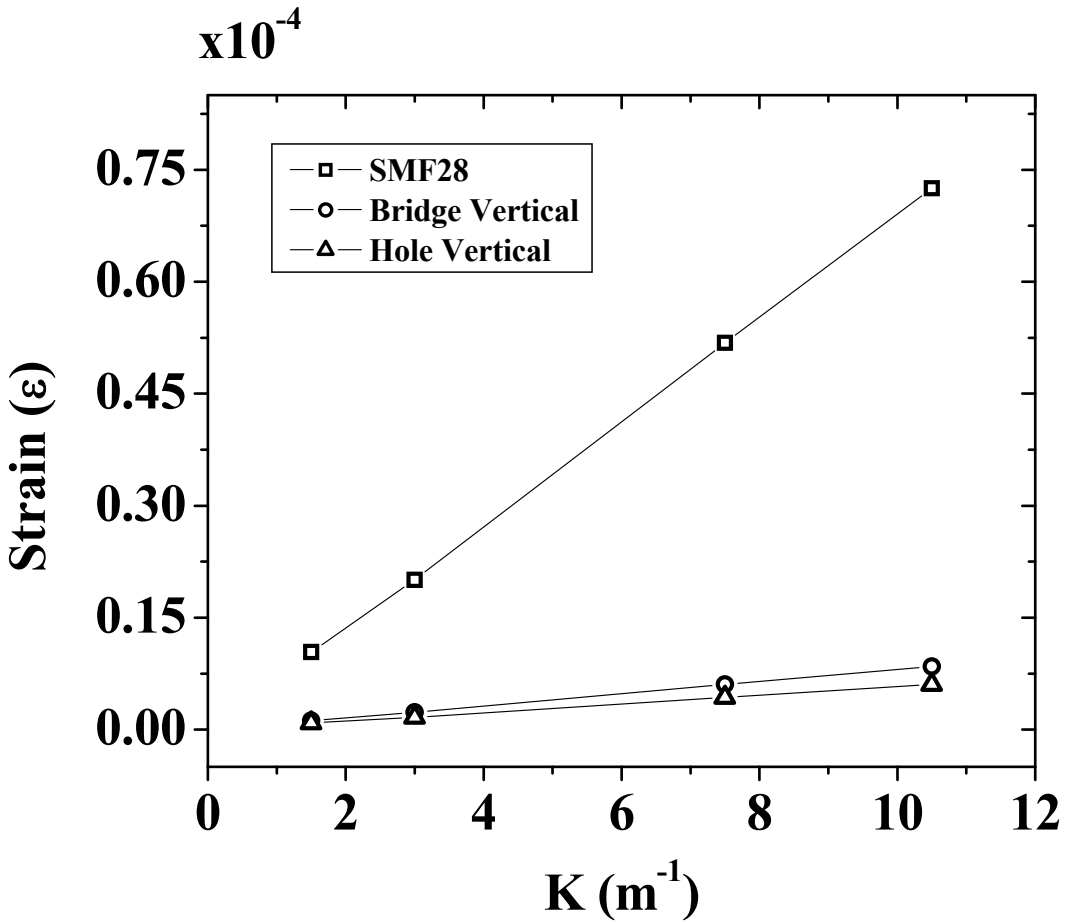

Figure 71: FEA simulation results of induced strain vs. curvature of bending for fiber length = 1 cm

5.3.3 Experiment

To verify the simulated results a bending experiment was performed on the suspended core fiber and SMF-28 with FBGs. The FBGs in the suspended core fiber were written using an ultrafast laser as mentioned previously [54]. The FBGs in SMF-28 were written using a standard phase mask inscription technique with a 248-nm KrF laser. To enhance the photosensitivity, fibers were hydrogen loaded at 1900 psi for one week at room temperature. The gratings were then annealed at 120^{o}C for 24 hours after the FBG writing.

The bending of the fibers was performed by first, mounting the suspended-core fiber on a rotational stage to adjust the orientation of the fiber to bending axis. The orientation of the air holes was via a CCD microscope mounted at the end of the fiber. The fiber was then clamped to a cantilever 12.88 cm in length with the length of fiber containing the FBG placed 3.08 cm from the fixed end of the cantilever. This setup allowed for only the deflection at the far end of the cantilever while ensuring that the grating would be in the nonlinear bending region of the cantilever. The fiber was then bent with an increasing curvature. The FBG spectral changes were monitored by using a broadband amplified stimulated emission source, an optical spectrum analyzer, and circulator. This procedure was repeated for both orientations of the suspended core fiber and the SMF-28 and the resulting spectra are presented in Figs. 72-74.

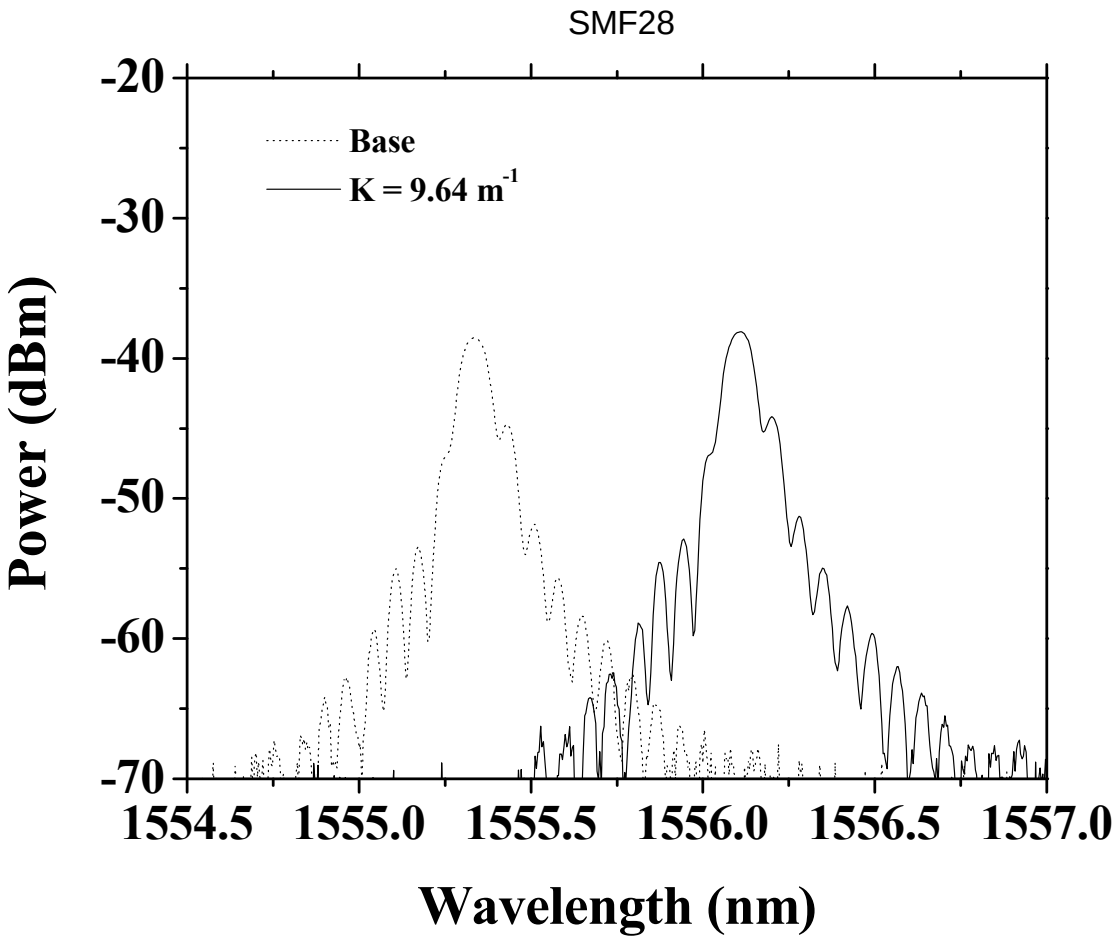

Figure 72: Unloaded and bending FBG spectrums of SMF-28

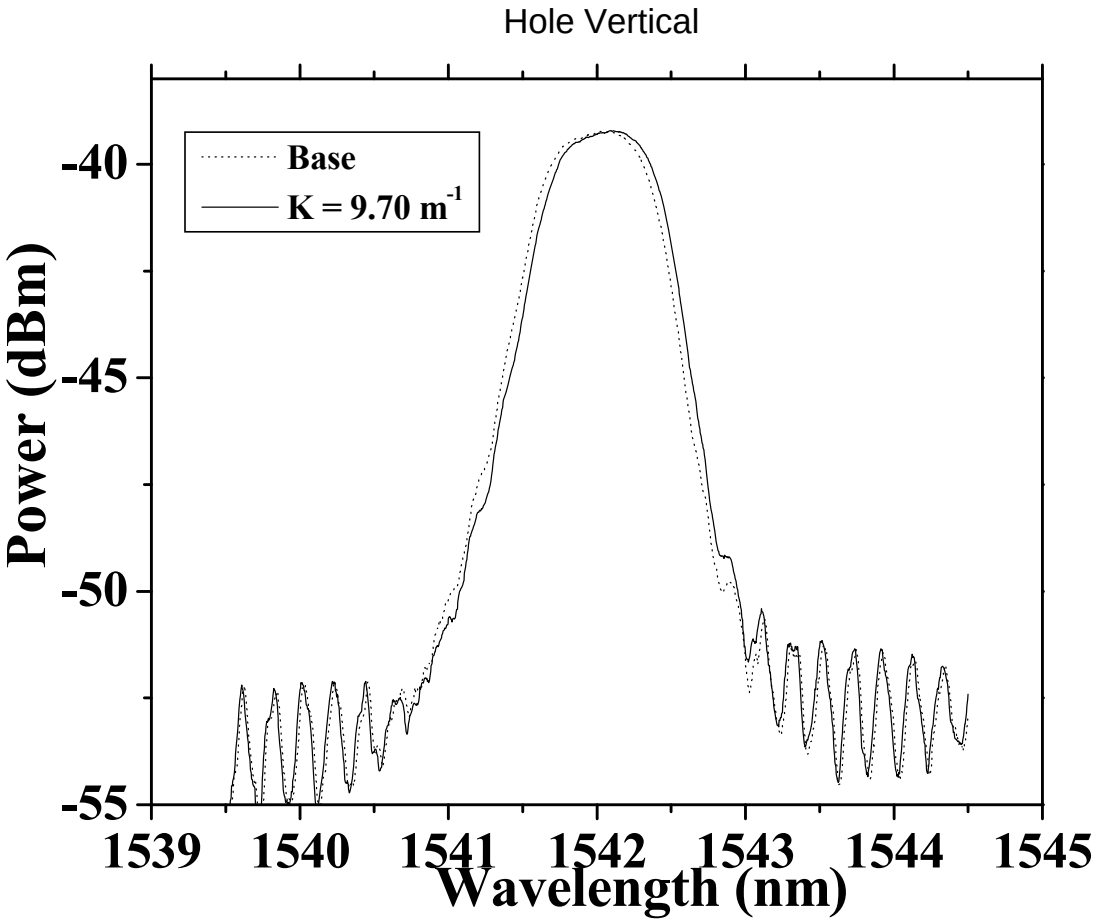

Figure 73: Unloaded and bending FBG spectrums of SCF with air hole vertical

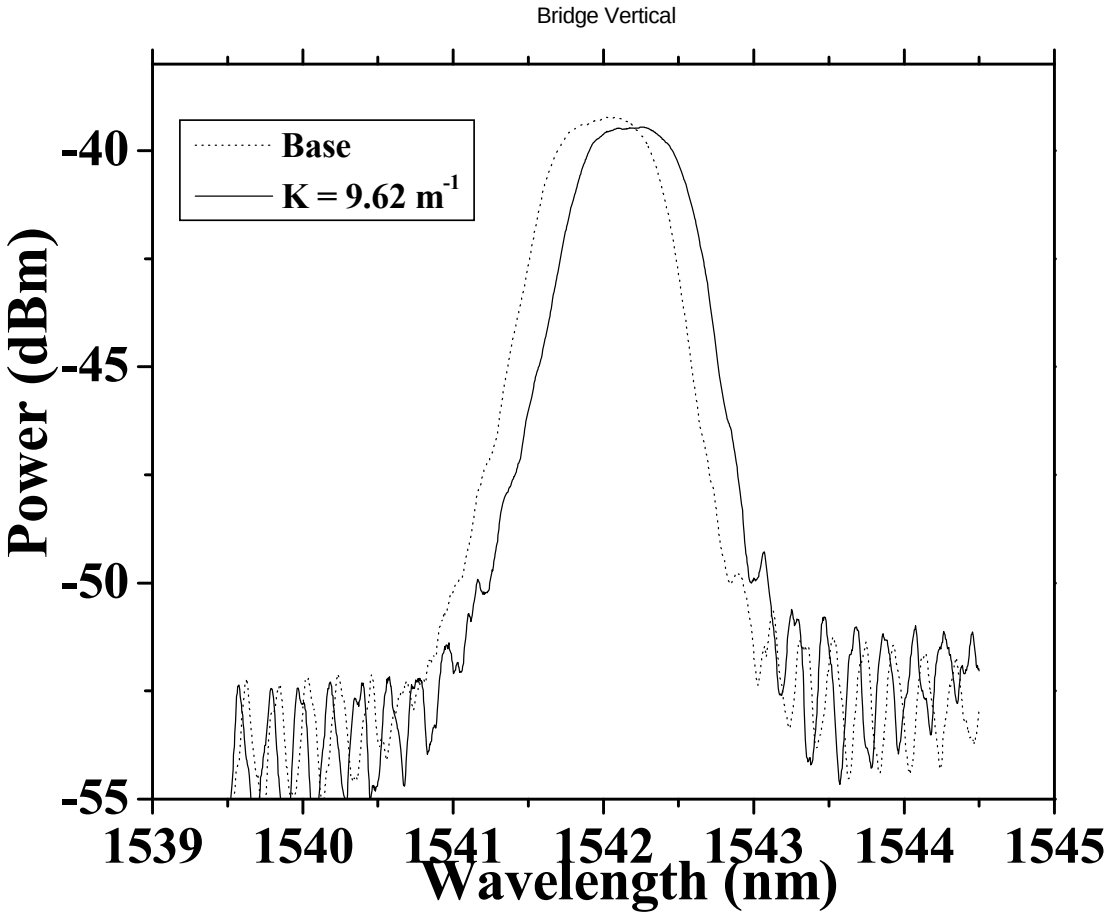

Figure 74: Unloaded and bending FBG spectrums of SCF with silica bridge vertical.

It is immediately apparent that the spectral shift in the SMF-28 grating is much larger than is induced in the suspended core fiber. The FBG response with increasing curvature is presented in Figure 89. The SMF-28 grating experiences a shift of 0.771 nm for a curvature of 9.64 m^{-1}. The suspended core fiber experiences shifts of 0.0877 nm and 0.0481 nm for the silica bridge and air hole parallel to the bending axis, respectively. There is an 8.79 and 16.02 times decrease in the wavelength shift for the suspended core fiber having the silica bridge and air hole parallel to the bending axis, respectively. However, at curvatures above 6 m^{-1} a decrease in the spectral shift is observed. The cause of this discrepancy is unclear to us at this time, but slipping of the fiber and fiber jacket is a strong possibility.

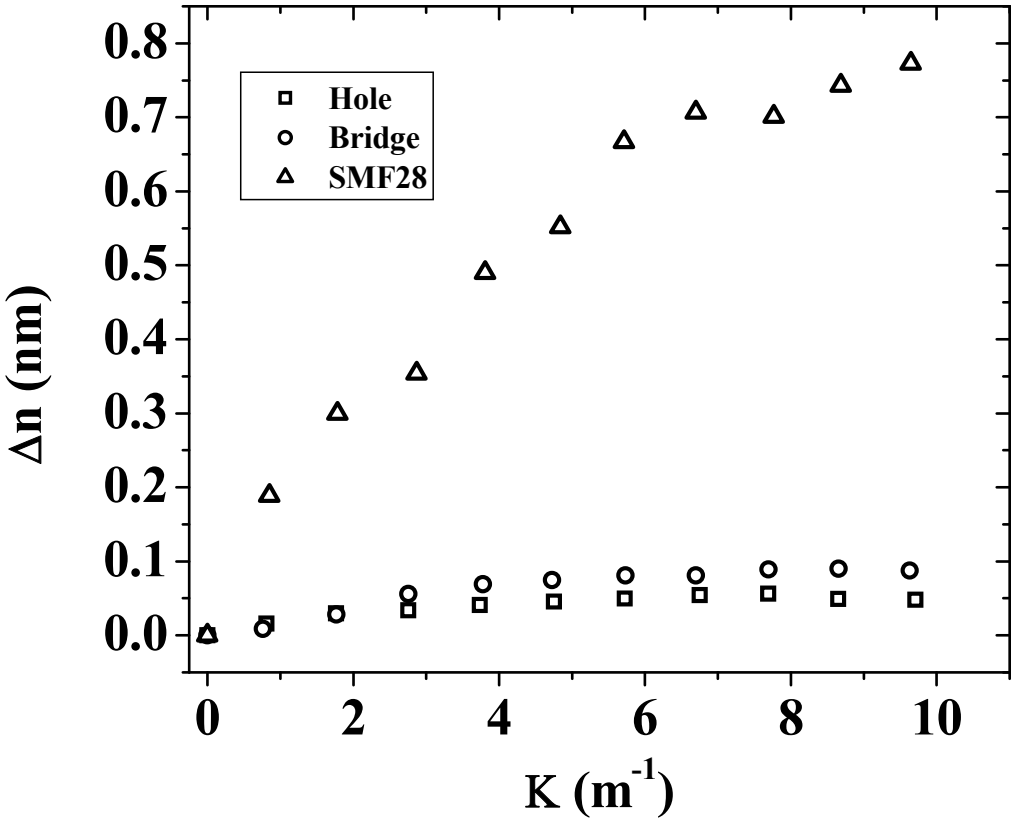

Figure 75: Experimental results for wavelength of FBG shift vs. curvature of bending.

5.3.4 Summary

In summary, I have presented simulations and experimental validation of a suspended core bending insensitive fiber with FBGs. Comparisons with FBGs in SMF-28 were also presented. The suspended core fiber possesses two directions of low sensitivity to an increased bending, allowing for the future creation of embedded sensors that remove the bending strain from the sensor's response.

5.4 BUCKLING OF SILICA BRIDGES AND THEIR EFFECTS ON THE OPTO-MECHANICAL PROPERTIES

5.4.1 Introduction

The incorporation of thin silica bridges in the fiber cladding can significantly alter the opto-mechanical properties of the fibers. It was shown earlier in this chapter that suspension-core fibers' response to lateral impact is highly directional, this is in contrast to that of standard fiber with solid core and cladding. Also, in the previous section studies showed that microstructured fibers with thin air bridges are insensitive to fiber bending. These interesting properties might be precursors to the design of fiber devices useful for sensing.

While specialty fiber architectures are pushing the envelope of fiber design, some unexpected opto-mechanical properties might arise from some extreme air-hole structures. Currently, silica bridges as thin as 0.1 μm are routinely fabricated in microstructured fibers [23, 25, 61]. This enables the fabrication of silica bridges with an extremely high aspect ratio. For these extreme structures, the opto-mechanical properties of the fiber and fiber devices can be affected by the elastic instability of silica.

In a situation that microstructured fibers with thin air bridge are under a compressive stress, while the stress imposed on the fiber is within the elastic limit of the silica materials, the air-bridge can still fail to support the load due to elastic instability. This phenomenon is referred to as buckling. First described by Leonhard Euler back in the 18^{th} century [62], buckling is an important issue in civil engineering. The buckling of reinforced columns in civil and mechanical structures often leads to structure failure. It also has significant impacts on the air-hole microstructure in optical fibers. For example, the buckling of air bridges fails to transfer the

external load to the fiber core, thus reducing the sensitivity fiber Bragg grating sensors. On the other hand, the buckling can be used to reduce or eliminate external impacts to the fiber core. This improves the environmental ruggedness of fiber devices without fiber packaging, an ideal avenue to develop environment-insensitive fiber through fiber design.

In this section, I present the finite element analysis (FEA) of suspended-core fibers with thin silica bridges. The buckling effects of suspended core fibers were studied as functions of fiber structures, external load, and thickness of silica bridges. The impact of buckling to fiber sensors were studied in four-core suspended cores fibers and wheel fiber structures. This section reveals that silica bridge buckling will have a significant impact on the opto-mechanical properties of optical fiber and fiber sensors.

5.4.2 Fiber Models

Three different fiber geometries were studied in this section as shown in Figure 90. The first of these designs was an all-silica 4-core suspended core fiber (SCF-1) that possessed an air-hole diameter and bridge thickness of 25 μm and 0.9 μm, respectively. This is the same fiber geometry that was used in the previous two sections and the opto-mechanical properties have been studied earlier in this chapter.

The second suspended core fiber geometry (SCF-2) was derived from the SCF-1. The core region was increased to 10 μm in diameter while the bridge thickness and air-hole diameters were 0.15 μm and 16 μm, respectively. The core diameter of 10 μm was chosen as from the V-number calculation [7] it is the largest the core can be in order to maintain single-mode operation at 1550 nm. The bridge design was chosen to be more susceptible to buckling than the first design, which reduces the transfer of stress from the external load to the fiber core.

The third fiber geometry (wheel-fiber) was modeled to have 16 supporting silica bridges shown in Figure 90. The core diameter, bridge thickness, and air-hole diameter are 10 μm, 0.15 μm, and 15.5 μm, respectively. The presence of more silica bridges allows for a more uniform dispersion of the external load. Moreover, supporting bridges that are not aligned with the external load are more susceptible to buckling. It also allows the observation of high order buckling modes. All of the fiber geometries were modeled to have an overall fiber diameter of 125 μm and are presented in Figure 76.

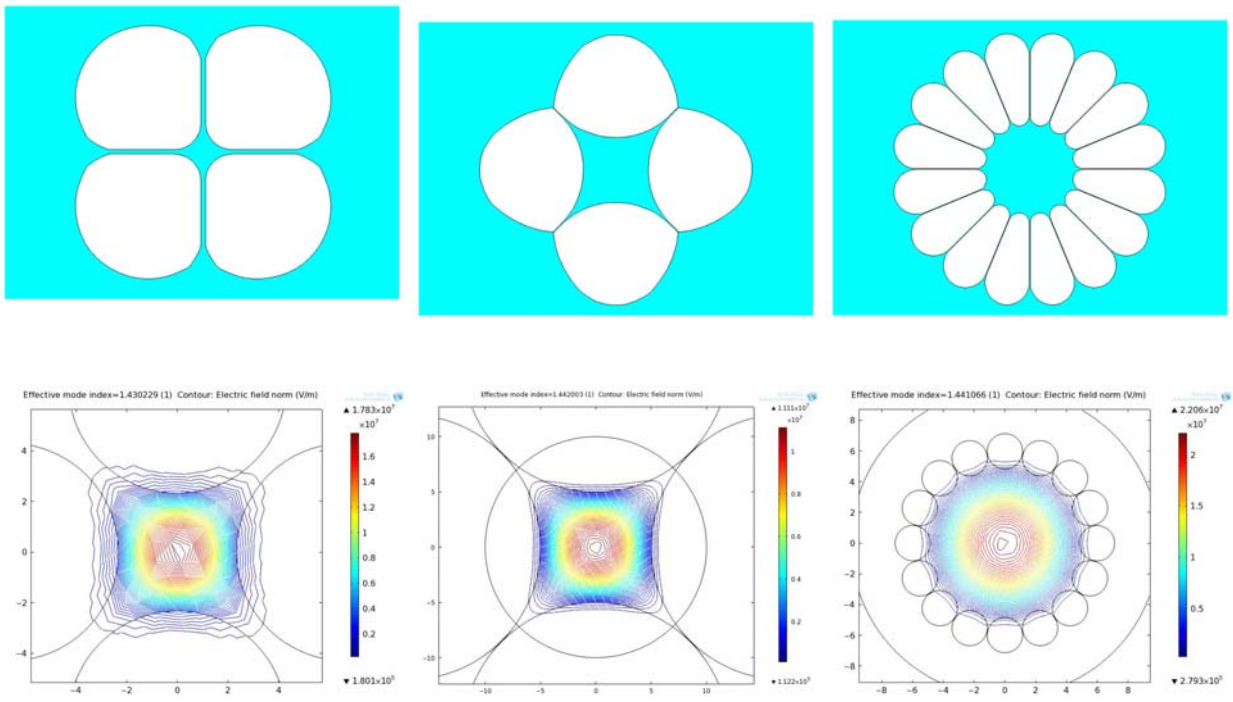

Figure 76: Hole-core regions for SCF1 (Left), SCF2 (Middle), and Wheel-fiber (Right) geometries and their guided mode profiles at 1550 nm.

Electric field distributions in the fiber core region were calculated for all three fiber geometries (Figure 76). As all the models were assumed to be all-silica, proper optical confinement and single-mode operation at 1550 nm required verification as well as the determination of the effective index of the fiber core. The index of refraction of silica was calculated by using the three-term Sellmeier polynomial [46] where at 1550nm the refractive index is n=1.44504 and the air-holes possessed a refractive index of n=1. The resulting effective indices (n_o) for the fiber geometries are 1.430229, 1.442003 and 1.441066 for SCF-1, SCF-2, and the Wheel-fiber, respectively.

5.4.3 Transverse Load Induced Birefringence

The simulations and theory for determining the fiber models' response to an applied transverse load are the same as mentioned previously. Figure 77 presents the birefringence contour plots for the all three fiber geometries at an applied compressive load of 50 N/cm for each fiber with the bridge and air-hole directly under the load. The induced birefringences for the silica bridge under load are 5.948×10^{-4}, 6.869×10^{-5} and 1.364×10^{-5} for SCF-1, SCF-2, and the Wheel-fiber. When the air-hole is under load the corresponding birefringences are 2.623×10^{-5}, 7.856×10^{-7} and 11.57×10^{-6} for SCF-1, SCF-2, and the Wheel-fiber. These results are consistent with what has been reported as the bridges act to focus the stress into the core region while the air-holes act to deflect the stress [51, 63]. As expected, the reduction of bridge thickness between SCF-1 and SCF-2 resulted in a significant reduction in the induced birefringence. However, by increasing the size of the core-region the induced birefringence is reduced by an order of magnitude. The Wheel-fiber experiences the lowest overall induced birefringence as adding more air-holes into the cladding helps to damp the transferred stress.

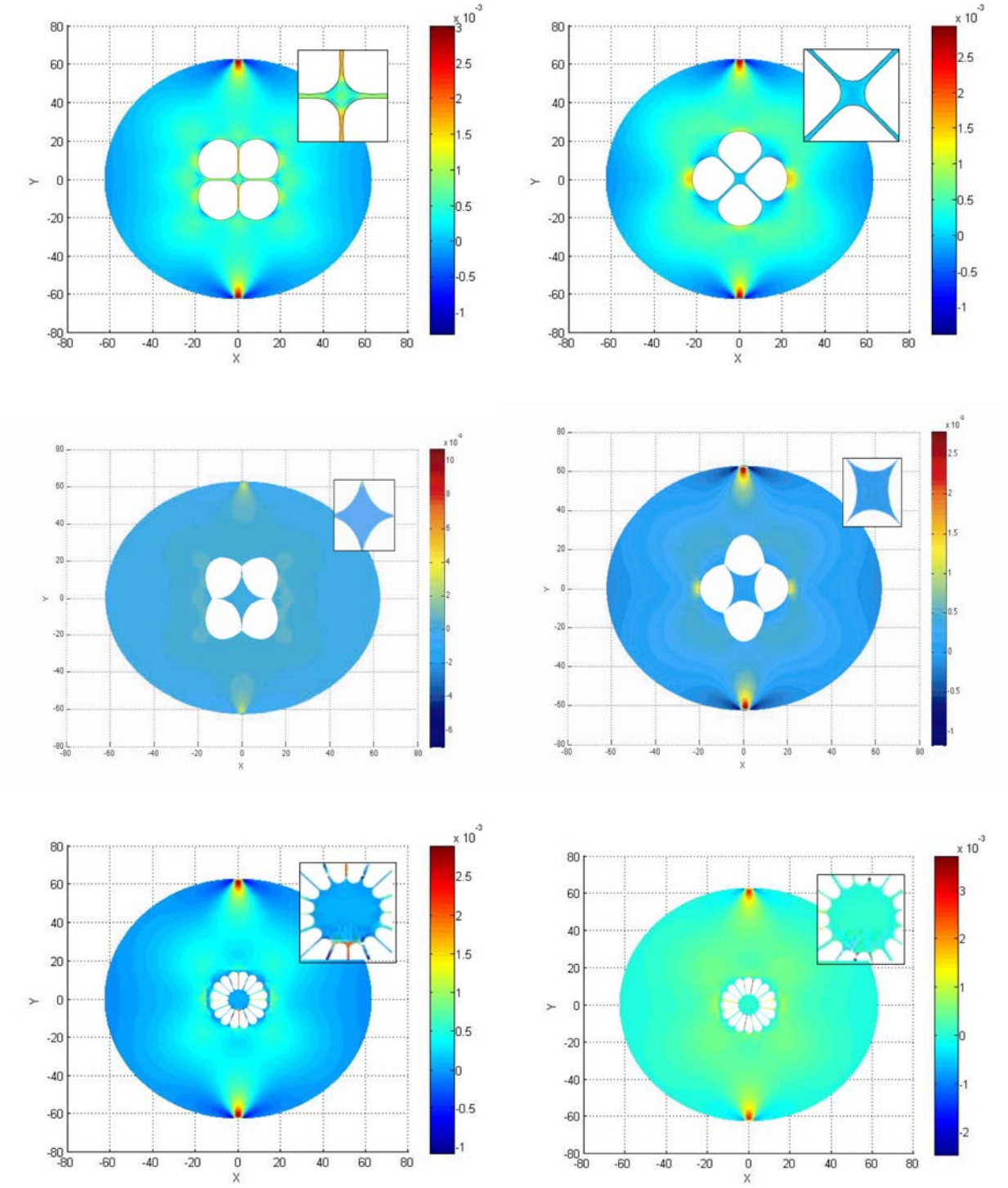

Figure 77: Induced birefringence when silica bridges (left) and air holes (right) are under 50 N/cm directional compression for three fiber designs.

5.4.4 Directional Dependency

Figure 78 shows that the opto-mechanical properties of air-hole fibers with silica bridges are sensitive to the orientation of the fiber with respect to the transverse load. In order to determine the directionality properties of all three fiber designs, FEA simulations were also performed to calculate fiber birefringence as functional of fiber orientation under 10 N/cm transverse loads.

Figure 78 depicts the sensitivities for all three fiber models with a solid line for SMF-28 (4.03×10^{-6} ΔB/N/cm). SCF-1 possesses sensitivities of 12.915×10^{-6} and 0.549×10^{-6} ΔB/N/cm for the bridge and air-hole under load, respectively with an angular span of 45^{o} (bridge and hole under load). SCF-2, with the thinner bridge and larger core diameter shows much lower sensitivities of 2.075×10^{-6} and 0.014×10^{-6} ΔB/N/cm for the bridge and air-hole under load, respectively. The wheel fiber design shows the smallest response to the external load with an almost ten-fold reduction in comparison to that of SMF-28. The orientation-dependent response for SCF-2 and the wheel fiber design is further detailed in Figure 79. Unlike the sine-like variation of SCF-1 between hole and stem under loads, SCF-2 and the wheel fiber designs show additional variations. The FEA simulation shows that the Wheel-fiber possesses sensitivities of 0.3517×10^{-6} and 0.4308×10^{-6} ΔB/N/cm for the bridge and air-hole under load, respectively with an angular span of 11.25^{o} between hole and stem under the load. What is apparent from Figures 78 and 79 is that with a thinner bridge and larger core diameter it is possible to create a fiber structure that is much less sensitive to an applied transverse load than that of SMF-28. The SCF-2 and Wheel-fiber geometries possess sensitivities 1.94 and 9.35 times lower than that of SMF-28. However, the decrease and increase in overall sensitivity to the applied load is primarily caused due to a buckling effect occurring within the bridges.

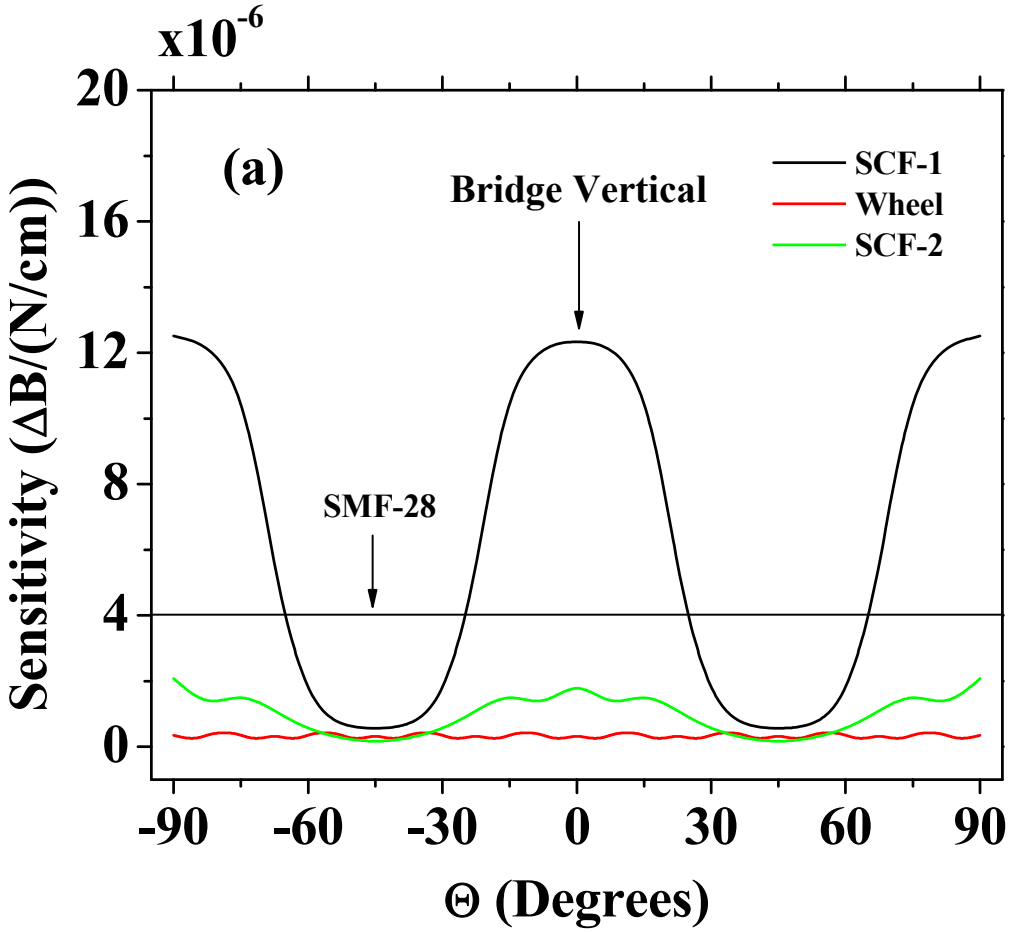

Figure 78: Sensitivity to directional compression as a function of rotation angles for three fiber designs

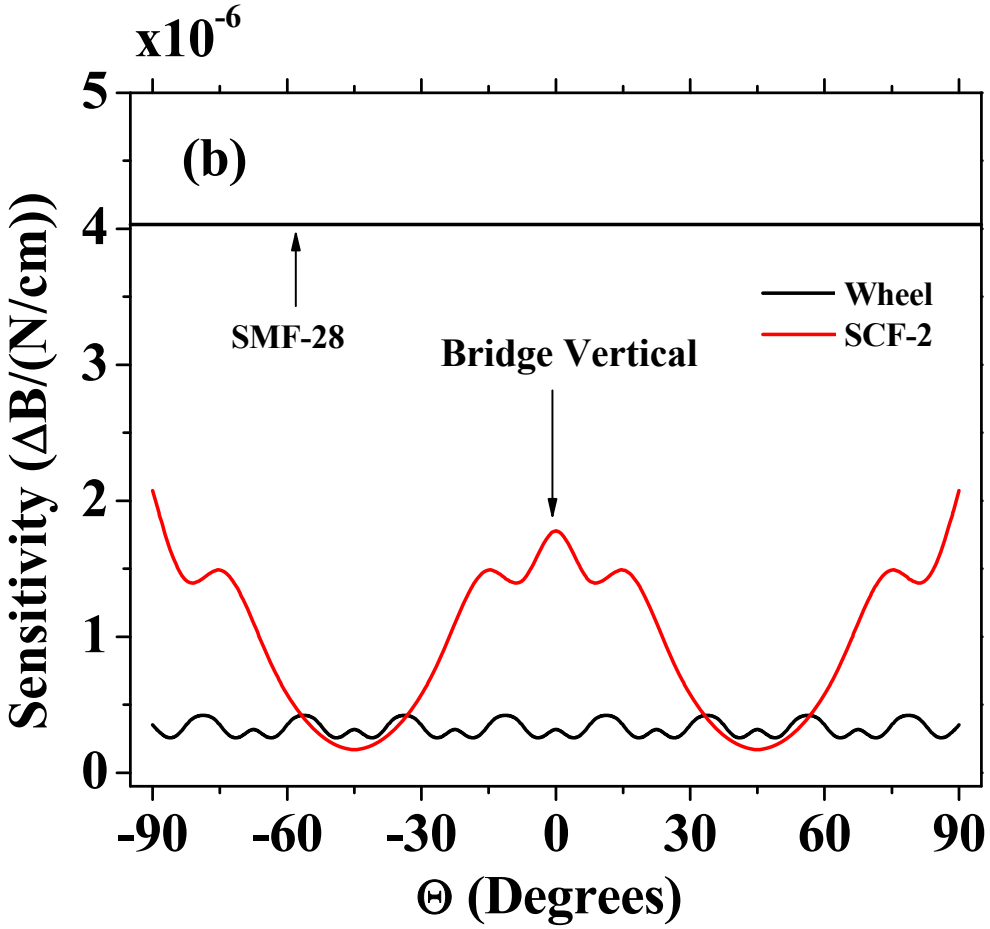

Figure 79: Sensitivity to directional compression as a function of rotation angles for the SCF-2 and Wheel designs.

5.4.5 Buckling Effects on Induced Birefringence

It has just been demonstrated that two of our fiber designs show drastic reduction of stress transfer into the fiber core than that of the standard fibers. This is partially due to a larger fiber core used in SCF-2 and the Wheel fiber in comparison to the SCF-1. More importantly, it is interesting to investigate the stress transfer mechanisms through thin silica bridges. Our FEA simulation has also confirmed that under 50 N/cm loads, strain imposed to silica bridges is within its elastic deformation limits. The fail of stress transfer through the bridge could be due to the mechanic instability of silica bridges, or bifurcation "buckling".

The bifurcation buckling refers to when a mechanical member such as a column fails and therefore is no longer supporting any of the compressive force with the compressive load being under the material's fracture limit. A large deformation occurs resulting in the column deforming into a different mode shape, which reduces the amount of deflection with increasing load. The mode shapes and buckling limits of the column under load are the Eigen value solutions to the homogenous Beam-Column equation [60, 62]:

$$w_n = \sin\left(n\pi \frac{x}{kl}\right), \quad n = 1,2,3,\ldots \tag{5.1}$$

$$F_n = \left(\frac{n\pi}{kl}\right)^2 EI, \; n = 1,2,3,\ldots \tag{5.2}$$

Where E is the Young's Modulus of the material, I is the second moment of area, l is the length of the column and k is the column's effective length factor (the length of an equivalent pin-ended member whose Euler load equals the buckling load of the frame member). The appearance of higher-order buckling modes requires the inclusion of several equally spaced supports within the structure. In the case of the silica bridges in the fiber cladding, the cross section of the column under load is a rectangle, which results in a second moment of area of

$$I = \frac{bh^3}{12} \tag{5.3}$$

where b is the length of the fiber under load and h is the thickness of the bridge. Inserting the equation for the second moment of area (Eqn. 5.3) and taking into account, $\sigma = F/A$, one is able to estimate the stress-limit for buckling:

$$\sigma = \left(\frac{n\pi h}{kl}\right)^2 \frac{E}{12}, \; n = 1,2,3,\ldots \tag{5.4}$$

Due to the nature of the fiber's fabrication, both ends of the silica bridges are fixed and unable to rotate, resulting in an effective length factor (k) of 0.5 [60]. Using Eqn. 5.2-5.4 and the effective length of the fiber with the fiber parameters mentioned earlier, the resulting buckling stresses for the first buckling mode are given in Table 3, which reveals that the buckling limits for the Wheel fiber and SCF-2 are significantly lower than that in SCF-1.

Table 3: Dimensions of three suspended core fibers and their bifurcation buckling limits

	h	***l***	***I***	σ
SCF-1	0.9 μm	20.33 μm	607.5 μm^4	480.46 MPa
SCF-2	0.15 μm	5.2 μm	2.812 μm^4	203.99 MPa
Wheel	0.15 μm	6.62 μm	2.812 μm^4	125.84 MPa

Figure 80 presents the induced birefringence for SCF-1 with increases load for the bridge and air-hole under loading. Both orientations yield linear dependence of birefringence on the external load, which have been experimentally confirmed earlier in this chapter. No buckling effects were found from the simulations. As suggested in Table 3, SCF-1 requires a much stronger compressive stress to induce buckling than those in other two fibers. To produce the required compressive stress at the ends of the silica bridge, the FEA computation indicates that a load > 80 N/cm is needed to apply to the outer edge of the fiber.

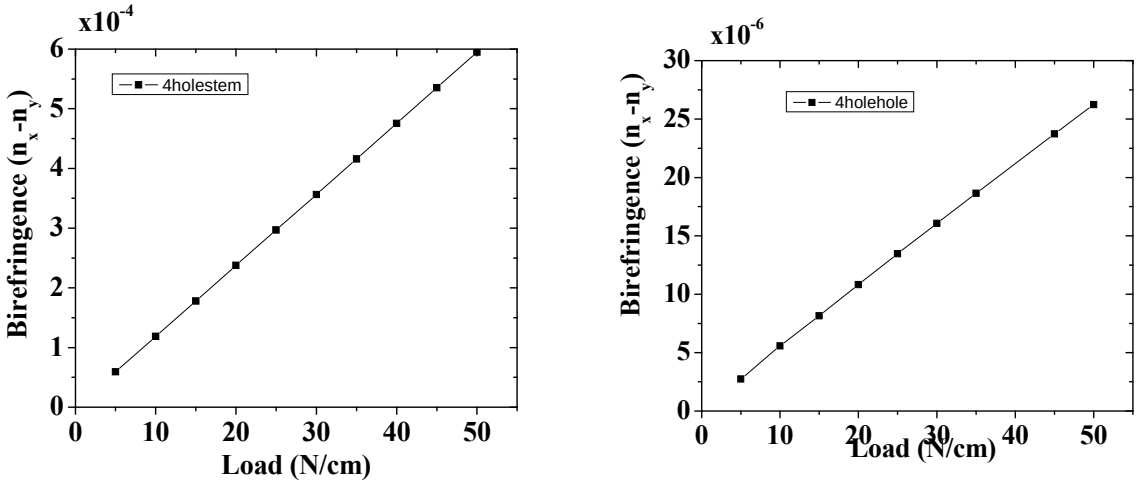

Figure 80: Induced birefringence for 4-hole suspended core fiber for bridge (left) and air-hole (right) under directional compression

Figure 81 presents the induced birefringence for SCF-2 as functions of external loads. What is immediately apparent is that when the bridge is under compression at loads above 20 N/cm, the fiber susceptibility to the external load reduces significantly when the bridge is under the load. The FEA simulation shows the first buckling mode when the bridge is directly under load of 25 N/cm. When the fiber is rotated 45^{o} so the air hole is directly under the load, induced birefringence increases with the external load without buckling. This is due to the effect to large air-holes has on deflecting the stress on the end of the silica bridges. This brings the stress below the buckling limits listed in Table 3.

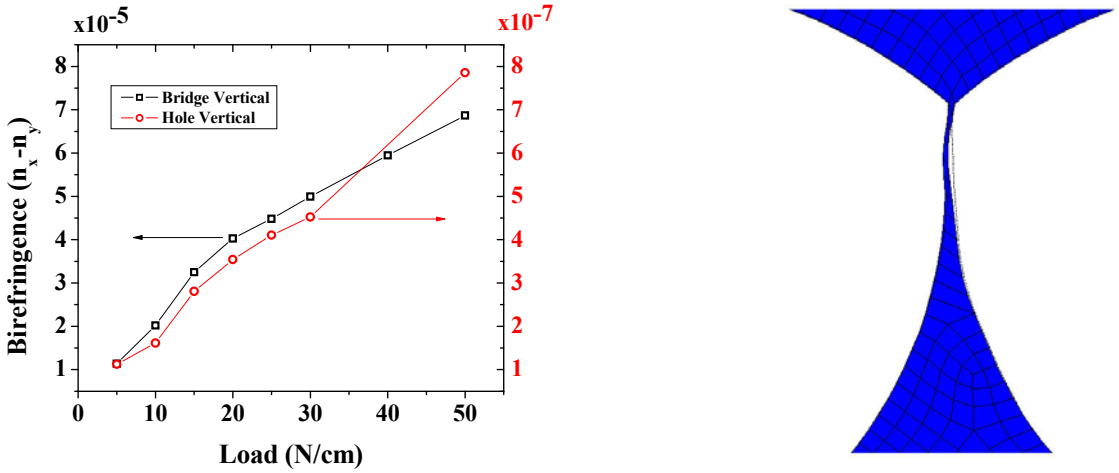

Figure 81: Induced birefringence for SCF-2 under external loads and FEA simulation revealing the buckling of silica bridge under at a load of 25 N/cm.

Figure 82 shows the induced birefringence for the Wheel-fiber with external loads as buckling becomes more prominent. The Wheel-fiber shows a decrease in the induced birefringence at loads over 20 N/cm when the bridge is under the compressive load. Figure 82 shows that one of the bridges has buckled into the first-mode shape while the bridge directly under the compressive load and the other bridges are still supporting their respective loads. When the air-hole is under the compressive load, fiber birefringence shows sudden drop when

the external load reach 20 and 37 N/cm, respectively. Figure 82 shows the first buckling mode occurs at loads of 20 N/cm in a single bridge. At an applied load of 37 N/cm the bridge that buckled at the lower load shifts into the second-order buckling mode. Additionally, a second bridge experiences a first-order buckling mode as illustrated in Figure 82. As was mentioned previously, the ability to experience higher-ordered buckling modes requires additional columns equally spaced within the structure.

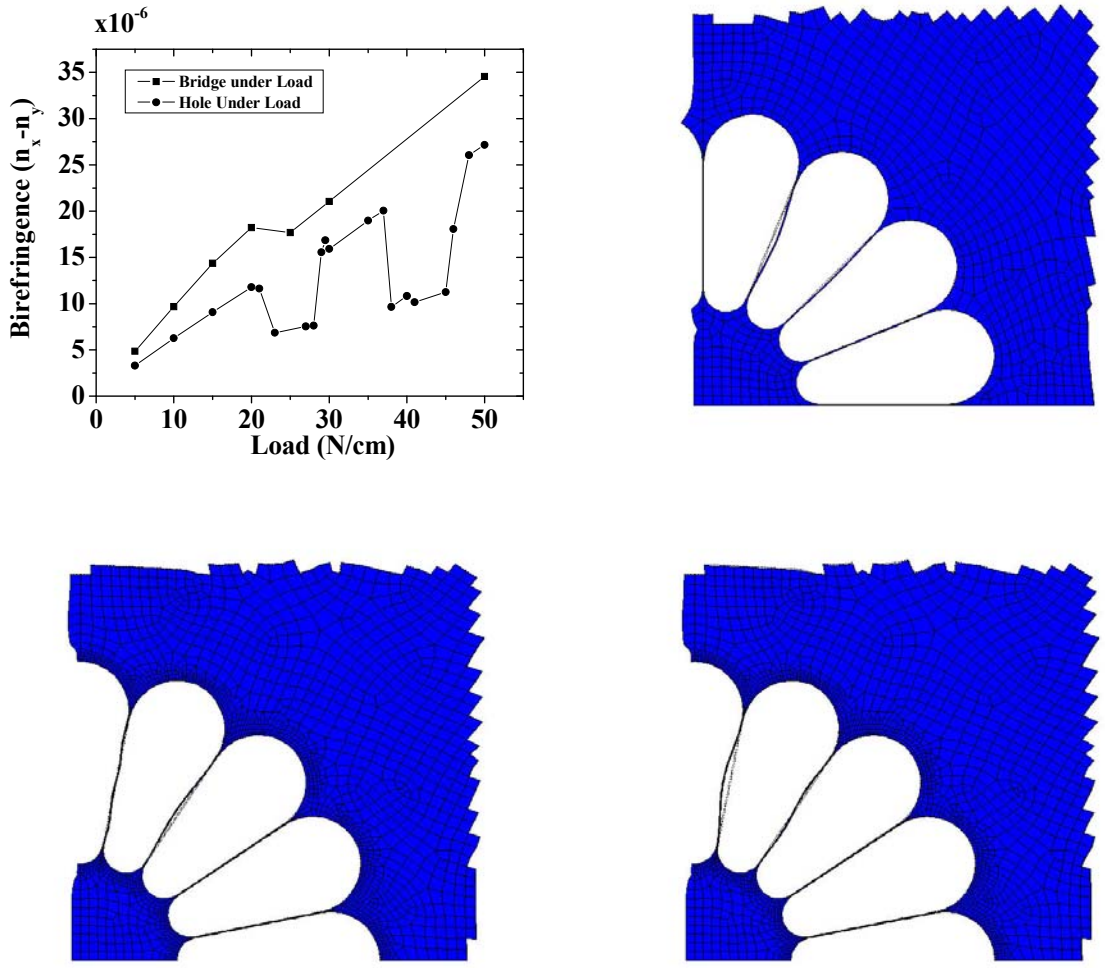

Figure 82: (Top left) Induced birefringence of the wheel fiber for bridge and air-hole under directional compression, (Top right) Buckling of the wheel fiber with bridge under loading (F = 25 N/cm). Buckling of the wheel fiber with air-hole under loading with (Bottom left) the first buckling mode (F = 25 N/cm) and (Bottom Right) the second buckling mode (F = 40 N/cm).

5.4.6 Summary,

In summary, I have presented the design of new suspended core optical fibers that are immune to an applied transverse load. Additionally, mechanical studies on the response of the silica bridge's response to increasing loads and their buckling was presented and thus presents a fiber sensor that can allow for the removal of transverse stress from impacting the fiber which can find great use in embedded sensing applications.

5.5 CHAPTER SUMMARY

In summary, I have demonstrated in this chapter several applications of suspended core optical fibers for sensing applications. A 4 hole suspended core fiber was shown to possess significant directional sensitivity to an applied transverse load while also possessing a low-bending sensitivity with directionality. New fiber geometries were designed and studied to create fiber sensors that were immune to transverse loads. The mechanisms behind this sensitivity was studied and found to be mechanical buckling.

6.0 CONCLUSION

In conclusion, this dissertation presents work on microstructured optical fibers for use as application specific sensors. As traditional solid optical fibers are well understood and are severely limited due to their cylindrical geometry it is necessary to create new fiber structures that can allow for engineering of specific sensor responses without the need of complex packaging. Through this process it is possible to create fiber sensors that are highly sensitive to external fields or immune to specific unwanted perturbations.

I have presented a compact overview of microstructured fibers from there inception in the 1970s up through current state of the art geometries and fabrication techniques. A detailed overview of pressure sensing at high temperatures was given including traditional IC circuits to current fiber sensor devices as a path into my work done on microstructured fibers at elevated temperatures for pressure sensing applications.

Work on induced birefringence in side-hole optical fiber was given. Starting with simulation data involving FEA I showed how the placement of the fiber core can affect the overall sensitivity to pressure. Experimental validations were performed using two fiber cross sections with different core placement. It was confirmed that the placement of the fiber core on the edge of the air hole will allow for the most sensitive fiber sensor. Solid fibers with FBGs were demonstrated to be able to work at temperatures above 400^{o}C vie the use of ultrafast laser inscription. The merging of the side-hole fiber and ultrafast laser writing technique allowed for

the demonstration of a microstructured FBG sensor that could monitor hydrostatic pressure at high temperatures.

Improvement of the hydrostatic pressure sensor was presented with a new tear-drop fiber structure. This fiber was studied via simulation to increase the overall sensitivity. Due to the difficulty in the geometry of the air hole a novel fabrication technique concerning the drilling of small air holes and an etching process was presented and confirmed to increase sensitivity. This fiber structure lead to the development of a highly-birefringent photonic crystal fiber that could monitor hydrostatic pressure. The fiber was designed so that single-mode operation would be maintained while significantly increasing the pressure sensitivity. By the inclusion of smaller air holes extending to the fiber's edge incorporated with the etching process demonstrated prior a highly sensitive pressure sensor was developed.

Suspended core optical fibers were studied for further development of optical sensors due to their unique geometry. The 4 hole suspended core fiber was chosen because of it's ability to act as a directionally dependent sensor. FBGs were inscribed in the fiber to allow for better ease of interrogation of the induced birefringence from the transverse load. Simulations and experiments confirmed that the suspended core fiber possessed one orientation that was much more sensitive to the applied load that the other. Further work was done on a suspended core bending sensor that was directionally dependent and much less sensitive to bending that that of SMF-28. Again, simulations and experimental validations were performed to show that when used as an embedded sensor the suspended core fiber would not be susceptible to bending. Finally, new suspended core fibers were developed so that a transverse load immune fiber could be implemented. The development of these fiber geometries lead to the studying of the

mechanical properties of the silica support bridges and the buckling that occurs at particular loads and the impact on the induced birefringence.

Overall, I have presented studies on multiple microstructured fiber geometries for the creation of application specific sensors. My unique approach of a merging of the optical and mechanical responses of these fibers has allowed me to create sensors with sensitivities and responses that have before been unobtainable. Future work on the fabrication and testing of these new designs as well as sensor deployment and other new geometries make this field exciting for additional research.

BIBLIOGRAPHY

[1] P. Kaiser and H. W. Astle "Low-Loss Single-Material Fibers Made From Pure Fused Silica" *The Bell Systems Technical Journal* **Vol. 53**, No. 6, pp. 1021-1039 July-August 1974.

Figure 1 from The Bell System technical journal by AMERICAN TELEPHONE AND TELEGRAPH COMPANY. Copyright 1974 Reproduced with permission of ALCATEL-LUCENT in the format Dissertation via Copyright Clearance Center.

[2] Xie, H. M., *et al.*, "Side-hole fiber for fiber-optic pressure sensing," *Optics Letters*, **Vol. 11**, No. 5, pp. 333-335 (1986).

[3] R. Clowes, S. Syngellakis and M. N. Zervas, "Pressure Sensitivity of Side-Hole Optical Fibers", IEEE Photon. Technol. Lett. **10**, pp. 857-859 (1998).

[4] J. C. Knight, T. A. Birks, P. St. Russel and D. M. Atkin, "All-silica single-mode optical fiber with photonic crystal cladding" *Optics Letters*, **Vol. 21**, No. 19 pp. 1547-1549 (1996).

[5] W. J. Bock, W. Urbancyzk and J. Wojcik, "Measurement of sensitivity of the single-mode photonic crystal holey fibre to temperature, elongation and hydrostatic pressure" *Meas. Sci. Technol.* **Vol. 15** pp. 1496-1500 (2004).

[6] C. Martelli, J. Canning, N. Groothoff and K. Lyytikainen, "Strain and temperature characterization of fiber Bragg gratings" *Optics Letters*, **Vol. 30**, No. 14, pp. 1786-1787 (2005).

[7] R . Ghosh, A. Kumar, J .P. Meunier and E . Marin, "Modal characteristics of few-mode silica-based photonic crystal fibres," Optical and Quantum Electronics **32**, pp. 963-970 (2000).

[8] S. Barkou Libori, J. Broeng, E. Knudsen, A. Bjarklev and H. R. Simonsen, "High-birefringent photonic crystal fiber," OFC 2001. Optical Fiber Communication Conference and Exhibit. Technical Digest Postconference Edition. (IEEE, 2001) pp. TuM2-1-3

[9] NKT Photonics - Photonic Crystal Fibers, SuperK Continuum Laser, Koheras Fiber Lasers, http://www.blazephotonics.com

[10] H. K. Gahir and Dhiraj Khanna, "Design and development of a temperature-compensated fiber optic polarimetric pressure sensor based on photonic crystal fiber at 1550 nm," Applied Optics 46, pp. 1184-1189 (2007).

[11] H Y Tam, S. K. Khijwania, and X.Y. Dong, "Temperature-Insensitive Pressure Sensor Using a Polarization-Maintaining Photonic Crystal Fiber based Sagnac Interferometer," 2007 Asia Optical Fiber Communication and Optoelectronics Conference, (IEEE, 2007) pp. 345-347.

[12] F. C. Fávero, S. M. M. Quintero, V. V. Silva, C. Martelli, A. M. B. Braga, I. C. S. Carvalho, and R. W. A. Llerena, "Photonic crystal fiber pressure sensor," Proc. SPIE 7503, 750364 (2009).

[13] M. Szpulak, T. martynkien, and W. Urbanczyk, "Highly birefringent photonic crystal fibre with enhanced sensitivity to hydrostatic pressure," 2006 International Conference on Transparent Optical Networks, (ICTON, 2006) pp. 174-177.

[14] T. Martynkien, G. Statkiewicz-Barabach, J. Olszewski, J. Wojcik, P. Mergo, T. Geernaert, C. Sonnenfeld, A. Anuszkiewicz, M. K. Szczurowski, K. Tarnowski, M. Makara, K. Skorupski, J. Klimek, K. Poturaj, W. Urbanczyk, T. Nasilowski, F. Berghmans, and H. Thienpont, "Highly birefringent microstructured fibers with enhanced sensitivity to hydrostatic pressure," Opt. Express 18, pp. 15113-15121 (2010).

[15] M. Szpulak, T. Martynkien, and W. Urbanczyk, "Effects of hydrostatic pressure on phase and group modal birefringence in microstructured holey fibers," Applied Optics 43, pp. 4739-4744 (2004).

[16] W. Bock, J. Chen, T. Eftimov and W. Urbanczyk, "A Photonic Crystal Fiber Sensor for pressure Measurments," IEEE Transaction on Instrumentation and Measurement, **Vol. 55**, No. 4, pp. 1119-1123 (2006).

[17] T. Nasilowski, T. Martynkien, G. Statkiewicz, M. Szpulak, J. Olszewski, G. Golojuch, W. Urbanczyk, J. Wojcik, P. Mergo, M. Makara, F. Berghmans, H. Thienpont, "Temperature and pressure sensitivities of the highly birefringent photonic crystal fiber with core asymmetry," Appl. Phys. B 81, pp. 325–331 (2005).

[18] M. Chen, R. Yu and A. Zhao, "Polarization Properties of rectangular lattice photonic crystal fibers" *Optics Communications*, **241**, pp. 365-370 (2004).

[19] S. Kim, S. Kee and C. G. Lee, "Modified rectangular lattice photonic crystal fibers with high birefringence and negative dispersion," Optics Express **17**, pp. 7952-7957 (2009).

[20] Kiang, K.M.; Frampton, K.; Monro, T.M.; Moore, R.; Tucknott, J.; Hewak, D.W.; Richardson, D.J.; Rutt, H.N.; , "Extruded singlemode non-silica glass holey optical fibres," Electronics Letters , vol.38, no.12, pp.546-547, 6 Jun 2002.

[21] M. Liao, C. Chaudhari, X. Yan, G. Qin, C. Kito, T. Suzuki and Y. Ohishi, "A suspended core nanofiber with unprecedented large diameter ratio of holey region to core" *Optics Express* **Vol. 18**, No. 9, pp. 9088-9097 (2010).

[22] H. Ebendorff-Heidepriem, S. C. Warren-Smith and T. M. Monro, "Suspended nanowires: Fabrication, design and characterization of fibers with nanoscale cores," *Optics Express*, **Vol. 17**, No. 4, pp. 2646-2657 (2009).

[23] Mukasa, K.; Petrovich, M.N.; Poletti, F.; Webb, A.; Hayes, J.; van Brakel, A.; Correa, R.A.; Provost, L.; Sahu, J.; Petropoulos, P.; Richardson, D.J.; , "Novel fabrication method of highly-nonlinear silica holey fibres," Lasers and Electro-Optics, 2006 and 2006 Quantum Electronics and Laser Science Conference. CLEO/QELS 2006. Conference on , vol., no., pp.1-2, 21-26 May 2006.

[24] A. S. Webb, F. Poletti, D. J. Richardson, and J. K. Sahu, "Suspended-core holey fiber for evanescent-field sensing", Opt. Eng. 46, 010503 (2007).

[25] L. Dong, B. K. Thomas and L. Fu, "Highly nonlinear silica suspended core fibers" *Optics Express*, **Vol. 16**, No. 21, pp. 16423-16430 (2008).

[26] M. L. V. Tse, K. M. Chung, L. Dong, B. K. Thomas, L. B. Fu, K. C. D. Cheng, C. Lu and H. Y. Tam "Obersercation of symmetrical reflection sidebands in a silica suspended-core fiber Bragg grating" *Optics Express*, **Vol. 18**, No. 16, pp. 17373-17381 (2010).

[27] Young, D. J. *et al.* "High-Temperature Single-Crystal 3C-SiC Capacitive Pressure Sensor," *IEEE Sensors Journal*, **Vol. 4**, No. 4, pp.464-470 (2004).

[28] Sippola, C. B. and C. H. Ahn, "A thick film screen-printed ceramic capacitive pressure microsensor for high temperature applications", *J. of Micromechanics and Microengineering*, **16**, pp. 1086-1091 (2006).

[29] Fonseca, M. A. *et al.*, "Wireless Micromachined Ceramic Pressure Sensor for High-Temperature Applications," *J. of Microelectromechanical Systems*, **Vol. 11**, No. 4, pp. 337-343 (2002).

[30] Chen, L and M. Mehregany, "A silicon carbide capacitive pressure sensor for in-cylinder pressure measurement," *Sensors and Actuators A*, **145-146**, pp. 2-8 (2008).

[31] Dorf, R. and J. Svaboda, *Introduction to Electric Circuits 5th Edition*. 2001, New York, New York: John Wiley & Sons, Inc.

[32] Zhao, Y. L. *et al.*, "High temperature and frequency pressure sensor based on silicon-on-insulator layers," *Meas. Sci. Technol.*, **17**, pp. 519-523 (2006).

[33] Guo, S. *et al.*, "High temperature smart-cut SOI pressure sensor," *Sensors and Actuators A*, **154**, pp. 255-260 (2009).

Figure 13 Reprinted from Sensors and Actuators A, Vol. 17, Guo, S. *et al,* High temperature smart-cut SOI pressure sensor, pp. 255-260 (2009) with permission from Elsevier.

[34] J. W. Borinksi, S. A. Meller, W. J. Pulliam, K. A. Murphy "Aircraft health monitoring using optical fiber sensors" 19th Digital Avionics System Conference. Proceedings, 7-13 Oct. 2000 (IEEE)

[35] Wang, Q. *et al.*, "Multiplexed Fiber-Optic Pressure and Temperature Sensor System for Down-Hole Measurement," *IEEE Sensors Journal*, **Vol. 8**, No. 11, pp. 1879-1883 (2008).

[36] Fielder, R. S. *et al.*, "State of the art in high-temperature fiber optic sensors," *Proceedings of the SPIE - The International Society for Optical Engineering*, **Vol. 5589**, pp. 60-68 (2004).

[37] Schroeder, R. J. *et al.*, "High pressure and temperature sensing for the oil industry using fiber Bragg gratings written onto side hole single mode fiber," *Proceedings of the SPIE - The International Society for Optical Engineering*, **Vol. 3746**, pp. 42-45 (1999).

[38] Yamate, T. *et al.*, "Thermally Insensitive Pressure Measurements up to 300 degree C Using Fiber Bragg Gratings Written onto Side Hole Single Mode Fiber," *Proceedings of the SPIE - The International Society for Optical Engineering*, **Vol. 4185**, pp. 628-632 (2000).

[39] Grobnic, D. *et al.*, "Long-term thermal stability tests at 1000^{o}C of silica fibre Bragg gratings made with ultrafast laser radiation," *Meas. Sci. Technol.*, **17**, pp. 1009-1013 (2006).

[40] R. Gafsi and M. A. El-Sherif, "Analysis of Induced-Birefringence Effects on Fiber Bragg Gratings", *Opt. Fiber Technology*. **Vol. 6**, pp. 299-323 (2000).

[41] Nye, J. F., *Physical properties of crystals*. 1985, Oxford, United Kingdom: Oxford University Press.

[42] M. Szpulak, G. Statkiewicz, J. Olszewski, T. Martynkien, W. Urbanczyk, J. Wójcik, M. Makara, J. Klimek, T. Nasilowski, F. Berghmans, and H. Thienpont, "Experimental and theoretical investigations of birefringent holey fibers with a triple defect," Applied Optics 44, pp. 2652-2658 (2005).

[43] M. Antkowiak, R. Kotynski, T. Nasilowski, P. Lesiak, J. Wojcik, W. Urbanczyk, F. Berghmans and H. Thienpont, "Phase and group modal birefringence of triple-defect photonic crystal fibres," J. Opt. A: Pure Appl. Opt. 7, pp. 763–766 (2005).

[44] C. Jewart, D. Xu. J. Canning and K. P. Chen, "Structure optimization of air-hole fibers for high-sensitivity fiber Bragg grating pressure sensors," Proc. of SPIE 7004 70041Z (2008).

[45] S. Kreger, S. Calvert and E. Udd, "High Pressure Sensing Using Fiber Bragg Gratings Written into Birefringent Side Hole Fiber," 2002 15th Optical Fiber Sensors Conference Technical Digest. (IEEE, 2002), pp. 355-358.

[46] I. H. Malitson, "Interspecimen Comparison of the Refractive Index of Fused Silica", J. Optical Society of America, **55**, pp. 1205-1209 (1965).

[47] W. Urbanczyk, T. Martynkien, and W. J. Bock, "Dispersion effects in elliptical core highly birefringent fibers," Appl. Opt. **40**, pp. 1911–1920 (2001).

[48] J. Noda, K. Okamoto, and Y. Sasaki, "Polarization maintaining fibers and their applications," J. Lightwave Technol. LT-4, pp. 1071–1089 (1986).

[49] Geernaert, T.; Luyckx, G.; Voet, E.; Nasilowski, T.; Chah, K.; Becker, M.; Bartelt, H.; Urbanczyk, W.; Wojcik, J.; De Waele, W.; Degrieck, J.; Terryn, H.; Berghmans, F.; Thienpont, H.; , "Transversal Load Sensing With Fiber Bragg Gratings in Microstructured Optical Fibers," Photonics Technology Letters, IEEE , vol.21, no.1, pp.6-8, Jan.1, 2009

[50] Yiping Wang; Bartelt, H.; Ecke, W.; Schroeder, K.; Willsch, R.; Kobelke, J.; Rothhardt, M.; Latka, I.; Brueckner, S.; , "Investigating Transverse Loading Characteristics of Microstructured Fiber Bragg Gratings With an Active Fiber Depolarizer," Photonics Technology Letters, IEEE , vol.21, no.19, pp.1450-1452, Oct.1, 2009

[51] C. Jewart, K. P. Chen, B. Mcmillen, M. M. Bails, S. P. Levitan, J. Canning, and I. V. Avdeev, "Sensitivity enhancement of fiber Bragg gratings to transverse stress by using microstructural fibers" Opt. Lett. 31, 2260-2262 (2006).

[52] V.V. Ravi Kumar, A. George, W. Reeves, J. Knight, P. Russell, F. Omenetto, and A. Taylor, "Extruded soft glass photonic crystal fiber for ultrabroad supercontinuum generation," Opt. Express 10, 1520-1525 (2002)

[53] Frazao, O.; Aref, S.H.; Baptista, J.M.; Santos, J.L.; Latifi, H.; Farahi, F.; Kobelke, J.; Schuster, K.; , "Fabry–PÉrot Cavity Based on a Suspended-Core Fiber for Strain and Temperature Measurement," Photonics Technology Letters, IEEE , vol.21, no.17, pp.1229-1231, Sept.1, 2009

[55] Becker, M., Bergmann, J., Brückner, S., Franke, M., Lindner, E., Rotthardt, M., and Bartelt, H., „Fiber Bragg grating inscription combining DUV sub-picosecond laser pulses and two-beam interferometry" Optics Express, Vol. 16, Issue 23, pp. 19169-19178 (2008)

[56] T. Belendez, C. Neipp and A. Belendez "Large and small deflections of a cantilever beam" *Eur. J. Phys.*, **23**, pp. 371-379 (2002).

[57] Z. Ning and J. R. Melrose "A numerical model for simulating mechanical behavior of flexible fibers" *Journal of Chemical Physics*, **Vol. 111**, No. 23, pp. 10717-10726 (1999).

[58] T. Belendez, M. Perez-Polo, C. Neipp and A. Belendez "Numerical and experimental analysis of large deflections of a cantilever beam under a combined load" *Physica Scrpita*, **Vol. T118**, pp. 61-65 (2005).

[59] J. D. Aristizabal-Ochoa "Large deflection and postbuckling behavior of Timoshenko beam-columns with semi-rigid connections including shear and axial effects" *Engineering Structures*, **29**, pp. 991-1003 (2007).

[60] V. J. Parks and A. J. Durelli "Various forms of the strain-displacement relations applied to experimental strain analysis" *Experimental Mechanics*, pp. 37-47, February 1964.

[61] S. Krenk, *Mechanics and Analysis of Beams, Columns and Cables 2nd Edition* (Springer 2001).

[62] L. Euler, Sur la forces des colonnes, Acad. R. Sci. Belles Letr. Berlin, Mem. 13, 252 (1759). English translation by J. A. Van den Broek, Am. J. Phys. **15,** 309, (1947).

[63] C. M. Jewart, T. Chen, K. P. Chen, E. Lindner, J. Fiebrandt, M. Rothhardt, K. Schuster, J. Kobelke and H.Bartelt, "Fiber Bragg grating transverse load sensor using suspended core fibers for directional dependent strain measurement," Accepted for publications to Optics Letters.